UNIVERSITY OF CALIFORNIA,
IRVINE

Understanding the Role of Convection on Global Land-Atmosphere Coupling and Remote Control of Amazonian Hydroclimate by the Andes

DISSERTATION

submitted in partial satisfaction of the requirements
for the degree of

DOCTOR OF PHILOSOPHY

in Earth System Science

by

Hongchen Qin

Dissertation Committee:
Associate Professor Michael S. Pritchard, Chair
Professor Jin-Yi Yu
UCI Chancellor's Professor James T. Randerson

2019

DEDICATION

To

the giants

whose shoulders

we could stand upon

&

everyone

whose collective efforts

laid

the foundation

for

those giants

to

stand upon

In

the pursuit of

the prosperity of humanity

TABLE OF CONTENTS

LIST OF FIGURES

Chapter 1

Chapter 2

Chapter 3

Chapter 4

LIST OF TABLES

Chapter 2

Chapter 3

Chapter 4

ACKNOWLEDGMENTS

First and foremost, I would like to express the deepest appreciation to my advisor Professor Mike Pritchard. His pursuit of excellence in research and persistence in probing the why question is inspiring; his enthusiasm and passion for science is infectious. His mentorship constitutes a nourishing environment which gives me freedom to try new things and provides advice when I lose directions. This dissertation would not have been possible without his continuous guidance and generous support in the past five plus years.

I would like to thank my committee members, Professor Jin-Yi Yu and Professor James Randerson, who provided valuable and constructive comments and suggestions on my dissertation research throughout my Ph.D. career. I also thank Prof. Francois Primeau, Prof. Gudrun Magnusdottir, and Prof. Amir AghaKouchak for being on my advancement committee.

The research in Chapter 2-3 is based on a published article in which I should thank my co-authors Gabe Kooperman and Hossein Parishani. I thank Martin Jung at Department Biogeochemical Integration at the Max Planck Institute for Biogeochemistry for providing the FLUXNET-MTE dataset. The subject matter of Chapter 4 is based on a manuscript in preparation in which I should thank Chris Terai, Julio Bacmeister, and Peter Bogenschutz.

Furthermore, I acknowledge all the professors who taught courses for our cohort in the 2014-2015 academic year. They are: Prof. Charles Zender, Prof. Francois Primeau, Prof. Michael Prather, Prof. Adam Martiny, Prof. Gudrun Magnusdottir, Prof. James Randerson, Prof. Claudia Czimczik, Prof. Isabella Velicogna. I also thank Dr. Elizabeth Crook, whom I worked with for four quarters as a teaching assistant. I am also grateful to Morgan Sibley, Jaycee Chu, Elliot McCollum, Melanie Nakanishi and other administrative staff in the department for being resourceful and their professional service.

In addition, I acknowledge the supporting and collaborative environment in the Pritchard Lab. I give my thanks to Sungduk Yu, Gabe Kooperman, Hossein Parishani, Jian Sun, Megan Flower, Chris Terai, Baird Langenbrunner, Stefan Rasp, Galen Yacalis, Tom Beucler, Griffin Mooers, Jacob Hendrickson and Soukayna Mouatadid.

Finally, I am eternally grateful to my parents and sister for supporting me tremendously in too many ways to list.

I acknowledge the funding from Department of Energy grant DE-SC0012152, the computational support from the Extreme Science and Engineering Discovery Environment under allocation TG-ATM120034 and from Yellowstone (ark:/85065/d7wd3xhc) provided by NCAR's Computational and Information Systems Laboratory under allocation UCIR0018.

CURRICULUM VITAE

Hongchen Qin

EDUCATION

University of California, Irvine Sep 2014–Dec 2019
Ph.D. Earth System Science Dec 2019
M.S. Earth System Science Dec 2017

Nanjing University of Information Science & Technology Sep 2010–June 2014
(Nanjing Institute of Meteorology)
B.S. Atmospheric Science

RESEARCH EXPERIENCE

Graduate Student Researcher Sep 2014–Dec 2019
Department of Earth System Science, UC Irvine
Advisor: Michael S. Pritchard
Dissertation Committee: Michael S. Pritchard, Jin-Yi Yu, James T. Randerson

Senior Thesis Research Sep 2013–Jun 2014
School of Atmospheric Science, NUIST
Advisor: Jianying Jia
Thesis: The Interdecadal Variation of the Summer Rainfall Pattern in East China and Its Relationship with the Tibetan Plateau Snow Cover

Undergraduate Student Researcher Summer 2012
School of Mathematics and Statistics, NUIST
Advisor: Wenjun Liu, Meifen Fu
Project: New bounds for Ostrowski type inequality involving integral means over end intervals.

PUBLICATIONS

Qin, H., Pritchard, M. S., Terai, C., Bacmeister, J., & Bogenschutz, P., Understanding the Remote Influence of Andean Convection on Amazonian Rainfall. *(In preparation*)

Qin, H., Pritchard, M. S., Kooperman, G. J., & Parishani, H. (2018). Global Effects of Superparameterization on Hydrothermal Land-Atmosphere Coupling on Multiple Timescales. *Journal of Advances in Modeling Earth Systems*, 10, 530–549. https://doi.org/10.1002/2017MS001185

Fu, M. and **Qin, H**. (2013). New bounds for Ostrowski type inequality involving integral means over end intervals and applications. *International Journal of Applied Mathematics and Statistics* 49, 490-498.

PRESENTATIONS

Qin, H., Pritchard, M. S., Terai, C., Bacmeister, J., & Bogenschutz, P., Stationary Wave Mediated Remote Control of Amazonian Rainfall by Andean Latent Heating: Implications for

Chronic Zonal Dipole Rainfall Biases in CMIP5 Simulations over South America, 2018 American Geophysical Union Fall Meeting. (Poster)
Qin, H., Pritchard, M. S., Terai, C., Bacmeister, J. & Bogenschutz, P., Amazonian Rainfall Biases of Andean Origin: Equatorial Wave Mediated Teleconnection over Tropical South America, 2018 Department of Energy (DOE) Earth & Environmental System Modeling (EESM) PI Meeting. (Poster)
Qin, H., Pritchard, M. S., Kooperman, G. J., & Parishani, H. Global Effects of SuperParameterization on Hydro-Thermal Land–Atmosphere Coupling on Multiple Timescales and an Amplification of the Bowen Ratio, 2017 American Geophysical Union Fall Meeting. (Poster)
Qin, H., Pritchard, M. S., & Parishani, H. Effects of Explicit Convection on Land-Atmosphere Coupling in GLACE-Type Experiments Using the SuperParameterized CAM, 2016 American Geophysical Union Fall Meeting. (Poster)

TEACHING

Teaching Assistant
Department of Earth System Science, UC Irvine
EarthSS 5: The Atmosphere — Spring 2016, 2017, 2018
Instructor: Elizabeth Crook
EarthSS 15: Climate Change — Winter, Fall 2016
Instructor: Michael Pritchard
EarthSS 17: Catastrophes — Fall 2015
Instructor: Elizabeth Crook

- Teaching weekly discussion sessions; grading assignments and exams; composing exam questions; holding office hours; leading review sessions.

CERTIFICATES

Deep Learning Specialization — Jun 2019
Credential ID 59YPGKMBERES
By *Andrew Ng, Deeplearning.ai* on *Coursera*
Machine Learning — Jan 2019
Credential ID LVP5KXW9UNAQ
By Andrew Ng, Stanford University on Coursera
Public Speaking: Activate to Captivate – Communication Certificate Series — Jun 2017
By Bri McWhorter, Graduate Division, UC Irvine

HONORS & AWARDS

Associated Graduate Student (AGS) Travel Grant, UC Irvine — Fall 2016, 2017
Editing Assistant Invitation for the Loh Down on Science, NPR — Mar 2017
Community Earth System Model (CESM) Tutorial, partial funding, NCAR — Aug 2016
Departmental Fellowship, ESS, UC Irvine — Sep 2014–Jun 2015
National Scholarship, NUIST — Nov 2012
Pacemaker of Excellent Students, NUIST — Nov 2012
The Second Prize in the 6th Mathematical Modeling Contest, NUIST — Jun 2012
Excellent Student Award, NUIST — Oct 2011
The First Prize in the Summer Vacation Social Practice, NUIST — Sep 2011

The Third Prize in the 5th Mathematical Modeling Contest, NUIST Jun 2011

PROFESSIONAL AFFILIATIONS

American Geophysical Union (AGU)
American Meteorological Society (AMS)
Chinese-American Oceanic and Atmospheric Association (COAA)

SERVICE & OUTREACH

Chinese-American Oceanic and Atmospheric Association Jul 2018–Aug 2019
Southern California Chapter
Executive Committee Member, Newsletter Editor & Webmaster

- Communications between our local chapter and the headquarters; documenting activities on the COAA-SCC website; MC for the Spring Festival Luncheon Assembly; assisting logistical managements for gatherings.

UCI Summer Data Science Workshop for CSULA DIRECT-STEM Student Aug 2015–2018

- Point of Contact, program "buddy"; assisting material preparation for instructors; sharing graduate experiences; presenting research; assisting field trips.

TECHNICAL TRAINING & SKILLS

Community Earth System Model (CESM) Tutorial, NCAR, Boulder, CO Aug 8-12, 2016

Proficient in NCAR Command Language (NCL), Python, MATLAB, Panoply, workflow management via Git/GitHub, Vim editing, UNIX/Linux and HPC environments.
Familiar with Fortran, C, NCO, GrADS, UV-CDAT, IDV.

ABSTRACT OF THE DISSERTATION

Understanding the Role of Convection on Global Land-Atmosphere Coupling and Remote Control of Amazonian Hydroclimate by the Andes

By

Hongchen Qin

Doctor of Philosophy in Earth System Science

University of California, Irvine, 2019

Associate Professor Michael S. Pritchard, Chair

This dissertation aims to better understand the role of moist convection (clouds and turbulence) in the complex dynamic coupling that occurs between components (land and atmosphere) as well as between subregions (Andes and Amazon) of the Earth system, using modern numerical modeling approaches. First, climate model representation of land-atmosphere coupling is compared between standard techniques that use conventionally parameterized convection versus prototype next-generation simulations that can include explicit convection. That is, numerical experiments are designed to isolate the global hydrologic land-atmosphere coupling on weekly-to-subseasonal and seasonal timescales using both approaches to representing convection in climate simulation. Initial analysis focuses on hydrologic coupling dynamics, and then the effects of explicit convection on thermal land-atmosphere coupling are highlighted over the southwestern U.S. and the Arabian Peninsula. Implications on global land surface Bowen ratio and its climate sensitivity are also discovered and discussed. Finally, a separate topic is analyzed, related to clarifying ongoing issues in capturing realistic regional hydroclimate over the Amazon. In this case the coupling dynamics are not between atmosphere and land, but between convective heating over a mountain chain (the Andes) and associated modulations of the atmospheric

thermodynamic environment over an upstream rainforest (the Amazon). These dynamics are elucidated using mechanism denial techniques within an ensemble hindcast experiment, which sheds light on a previously underappreciated Andean control on Amazonian rainfall. Key results from these analyses are summarized below.

The first theme (Chapter 2) is to investigate the effects of explicit convection on global hydrologic land-atmosphere coupling across multiple timescales. Over weekly-to-subseasonal timescales, based on experiments following the Global Land-Atmosphere Coupling Experiment (GLACE) protocol, explicit convection is found to systematically mute the soil moisture–precipitation coupling strength on a global scale which is primarily linked to the atmospheric segment (evapotranspiration–precipitation) of the land-atmosphere feedback. Whereas this sensitivity is pronounced on short timescales relevant to synoptically driven drought and hydrologic weather extremes, over longer (seasonal) timescales, based on simulations following the Atmospheric Model Intercomparison Project (AMIP) protocol, the effects of explicit convection on seasonal hydrologic land-atmosphere coupling are undetectable.

The second topic (Chapter 3) is to uncover the effects of explicit convection on global thermal land-atmosphere coupling. In both the GLACE- and AMIP-type simulations, a range of complementary metrics all suggest that explicit convection robustly changes the thermal coupling within specific subregions of the globe. Over the Arabian Peninsula, explicit convection produces less but more realistic time-mean rainfall, pushing local soil moisture regime away from the optimal transitional regime, which is required for strong coupling. As a result, local thermal coupling strength is significantly reduced. Over the southwestern U.S. and northern

Mexico, explicit convection substantially enhances the thermal coupling strength independent of soil moisture or precipitation. Instead, such enhancement is related to increases in the local surface Bowen ratio. Based on a variety of simulations across multiple model version pairs of using parameterized vs. explicit convection, I conclude that the use of explicit convection has a systematic and robust effect of increasing the land surface Bowen ratio. Furthermore, under climate change scenarios, comparing to parameterized convection, explicit convection exhibits a remarkably stronger amplification of the land surface Bowen ratio. This opens up new questions in the era of explicitly simulated convection in climate models pertaining to surface climate simulation.

The third subject matter (Chapter 4) of the thesis is motivated by the ubiquitous "Wet Andes – Dry Amazon" (WADA) dipole pattern of rainfall biases seen in the Coupled Model Intercomparison Project Phase 5 (CMIP5) archive. Using the Community Earth System Model version 1 (CESM v1) and focusing on the wet season, mechanism denial experiments are conducted to investigate the remote influence of Andean convection on Amazonian rainfall. It is shown that Andean convective heating reduces rainfall over the Amazon with a maximum of -1 mm/day, and that this response sets up rapidly, within 15 hours. Column moisture budget analysis shows that the total advection of moisture over the Amazon due to Andean convective forcing is controlled by the vertical advective term in ways that can be traced back to a mountain-forced component of the vertical velocity field. Meanwhile, other causative pathways that could control Amazon precipitation through the surface moist static energy, gross moist stability, or column energetics are found to be either irrelevant or secondary.

Chapter 1. Introduction

1.1 Overview

Atmospheric convection is crucial in transporting heat, momentum, and moisture within the troposphere, and it occurs across a broad range of spatial and temporal scales. This dissertation aims to better understand the role of convection within the Earth system through numerical investigations into the impacts of explicit convection on global hydrologic and thermal land-atmosphere coupling, and remote influence of Andean convective heating on Amazonian rainfall over South America.

1.2 Effects of explicit convection on global hydrologic land-atmosphere coupling across multiple timescales

Land-atmosphere feedbacks refer to interactions between state variables belonging to the land and atmosphere, among which soil moisture is of essential functionality in modulating the energy balance and the hydrological cycle. Soil moisture directly modulates local evapotranspiration (ET), surface Bowen ratio, and impacts atmospheric boundary layer stability, near-surface temperature, convection, clouds, and precipitation. As a major component of land-atmosphere interaction, the soil moisture-precipitation feedback has received considerable attention. In transitional zones, i.e., geographic regions where soil moisture is neither too small nor too large for interactions with the atmosphere to be inconsequential, elevated soil moisture can enhance ET, which may decrease or increase subsequent precipitation, and with few exceptions increasing (decreasing) precipitation will cause changes in soil moisture in the same direction,

completing the whole feedback loop (Seneviratne et al. 2010a). The soil moisture-precipitation feedback intrinsically involves ET. As a result, this complex overall feedback is often decomposed into two links: first, the soil moisture-ET (the terrestrial segment) and next the ET-precipitation (the atmospheric segment).

The feedback link between ET and precipitation is very uncertain, rendering the sign of the total soil moisture-precipitation feedback difficult to characterize. Depending on the impacts of the synoptic-scale background circulation, soil moisture-precipitation feedback can be either positive or negative (Cook et al. 2006; Entekhabi et al. 1992; Froidevaux et al. 2014). Even in the absence of impacts from background circulation, the sign of the soil moisture-precipitation feedback is still affected by the relative dominance of descending in the Level of Free Convection (LFC) and growing of boundary layer depth in triggering convection (Schlemmer et al. 2012), and by whether the complex effects of explicit convection are included (Hohenegger et al. 2009). Furthermore, mesoscale soil moisture spatial distribution patterns can also alter the soil moisture-precipitation feedback (Taylor et al. 2012a; Taylor et al. 2011). As a result, different studies have disagreed on the sign of the feedback. Over the eastern United States, using North American Regional Reanalysis dataset (NARR), after mitigating the impact of large-scale synoptic systems, Findell et al. (2011) argue that the probability of afternoon precipitation is enhanced by high evaporation over the eastern United States and Mexico. However, based on remote sensing, in-situ, and reanalysis datasets, Guillod et al. (2014) find no confirmation from observational-derived data for the positive relationship of the ET-precipitation link over the eastern United States revealed by NARR.

Much of our historical intuition for land-atmosphere feedback in global climate models comes from the Global Land-Atmosphere Coupling Experiment (GLACE) (Koster et al. 2006a), in which a metric for the land-atmosphere coupling strength, namely the degree to which land surface anomalies can impact the atmosphere, is intercompared across twelve modeling groups. This GLACE study concluded that land-atmosphere coupling hot spots occur in transition regions and a follow-up study suggests that the inter-model variation of land-atmosphere coupling strength in GLACE mostly comes from differences in the soil moisture-evaporation link (Guo et al. 2006). In results of the GLACE, during boreal summer, regions of strong soil moisture–precipitation coupling include the central Great Plains of North America, the Sahel, equatorial Africa, and India (Koster et al. 2004).

Multiple studies have since cast doubt on the soil moisture-precipitation coupling strength obtained by Global Climate Models (GCMs) via the GLACE protocol. Wei et al. (2010) argue that considering the tendency of GCMs to underestimate of the low-frequency band of precipitation variability, the soil moisture–precipitation coupling strength obtained in GLACE should be re-calibrated to be smaller. Utilizing observational data from the Atmospheric Radiation Measurement Program's Southern Great Plains (SGP) Central Facility site, Phillips and Klein (2014) suggest that the impacts of soil moisture on precipitation, unlike in GCMs, are minimal and the soil moisture-precipitation coupling strength over the central United States may be overestimated in modern ESMs. Consistent with this view, remote sensing observations also suggest weaker soil moisture–precipitation coupling compared to modeled coupling strength (Ferguson et al. 2012; Levine et al. 2016b).

Soil moisture–precipitation interactions are too important to be misrepresented, yet too complex to be realistically simulated by traditional GCMs. One huge uncertainty in traditional GCMs comes from parameterizations of sub-grid scale cloud processes. Such deficiencies have plagued the atmospheric modeling community for decades. The best approach to solve this problem would be using a Global Cloud-Resolving Model (GCRM). Despite the progress on this front, long-duration simulations using this type of model are not yet practical due to computational limitations (Fukutomi et al. 2016; Randall 2013; Sasaki et al. 2016; Satoh et al. 2019; Stevens et al. 2019). Another more practical approach, called cloud SuperParameterization (SP), is to embed a Cloud-Resolving-Model (CRM) within every grid column of a GCM, to explicitly simulate deep convection, shallow convection and cloud overlapping, making it possible to couple large-scale circulation, cloud processes, gravity wave dynamics, turbulence, and radiative transfer, hence enabling generally more realistic and explicit simulations of weather and climate (Randall et al. 2003; Randall 2013). This approach is computationally much cheaper than a GCRM model while still maintaining many of the physical merits of explicit convection. SP models have been shown to give fruitful results in some aspects of atmospheric simulations that have been challenging in conventional GCMs, such as the Madden-Julian Oscillation (MJO), the diurnal cycle of precipitation, and the frequency and intensity statistics of rainfall (Benedict and Randall 2009; Demott et al. 2007; Kooperman et al. 2016; Pritchard and Somerville 2009; Randall 2013).

The research objective of Chapter 2 is to reveal the effects of explicit convection by using the SP framework on global soil moisture–precipitation coupling across multiple timescales. In particular, chapter two aims to answer the following research questions:

(1) How does explicit convection change the soil moisture–precipitation coupling in GLACE-type experiments that measure it with soil moisture synchronization? Are these effects global or regional?

(2) How to understand the effects of explicit convection on hydrologic land-atmosphere coupling? Is the atmospheric segment or the terrestrial segment the dominant driver of the overall effects of explicit convection?

(3) Does explicit convection change the hydrologic land-atmosphere coupling on seasonal timescales? Why or why not?

1.3 Effects of explicit convection on global thermal land-atmosphere coupling and implications on land surface Bowen ratio

The soil moisture–temperature feedback can be described as follows: negative soil moisture anomalies will reduce surface ET and latent heat flux, which leads to more surface sensible heat flux and higher temperature; elevated temperature may in turn enlarge the water vapor deficit, potentially producing more ET despite dryer soils and hence exacerbating soil moisture dryness (Seneviratne et al. 2010a). The soil moisture-temperature feedback may interplay with the soil moisture-precipitation feedback. For instance, less rainfall results in soil moisture deficit, leading to strengthened surface sensible heat flux and increased surface temperature (Berg et al. 2015). Over strong land-atmosphere coupling regions, soil moisture-atmosphere interactions are also able to alter the mean, variance, and higher-order distribution moments in the probability density functions of surface temperature (Berg et al. 2014).

Soil moisture-temperature feedbacks can impact society and ecosystems by modulating the intensity and persistence of heatwaves (Fischer et al. 2007b; Lorenz et al. 2010), which subsequently contribute to increased mortality, forest fires and crop yield shortfall (Fischer et al. 2007a). Regional simulations of the 1976, 1994, 2003, and 2005 heat extremes over Europe demonstrate (Fischer et al. 2007a) that these heatwave events can be partially attributed to preceding soil moisture depletion, and 50-80% of sweltering summer days can be attributed to soil moisture-temperature interactions. As a consequence of global warming, there is a higher probability of hot extremes induced by surface soil moisture deficits (Mueller and Seneviratne 2012). In future climate, new transitional climate zones of strong land-atmosphere coupling have been predicted to form in central and eastern Europe, which could likewise contribute to increased summer temperature variability and hot extremes by end of century (Seneviratne et al. 2006).

The research objective of Chapter 3 is to shed light on the effects of explicit convection on soil moisture-temperature coupling and understand why explicit convection changes the thermal coupling in a certain way. Specifically, this chapter will address the following research questions:

(1) What are the effects of explicit convection on soil moisture–temperature coupling based on ensemble hindcast experiments following the GLACE protocol?

(2) Are these effects of explicit convection robust insofar as they are similarly detectable when using different types of experiment designs and different diagnostics to measure soil moisture–temperature coupling?

(3) Why does explicit convection impact the thermal coupling in the manner observed?

(4) Does explicit convection have an impact on the surface Bowen ratio? Does explicit convection have a robust effect on the future amplification of the surface Bowen ratio in a warmer climate?

1.4 Understanding the remote influence of Andean convection on Amazonian rainfall

Amazonia is the most diverse terrestrial ecosystem on the planet with crucial impacts on regional and global weather and climate. It is a massive carbon sink capable of buffering to some degree the current carbon stress impacting the atmosphere. As the climate warms, this paradise of biodiversity and its carbon buffering functionality may be endangered by water stress and deforestation in the coming decades (Levine et al. 2016a; Malhi et al. 2008; Malhi et al. 2009; Medvigy et al. 2013).

GCMs remain an important tool for projecting future climate and informing mitigation and adaptation strategies. Nevertheless, biases in GCMs in the present climate increase uncertainties of future climate projections, reducing the reliability of this policy-making process. Models participating in the Coupled Model Intercomparison Project Phase 5 (CMIP5) do not perform well on the hydroclimate over the Andes-Amazon region, as can be seen by the biases of annual-mean rainfall in the multi-model-mean of CMIP5 (Figure 1.1). I will refer to the zonal dipole structure of rainfall biases as the “Wet Andes – Dry Amazon” (WADA) in this thesis. This WADA bias pattern is also evident in the multi-model-median from CMIP5 (Mueller and Seneviratne 2014).

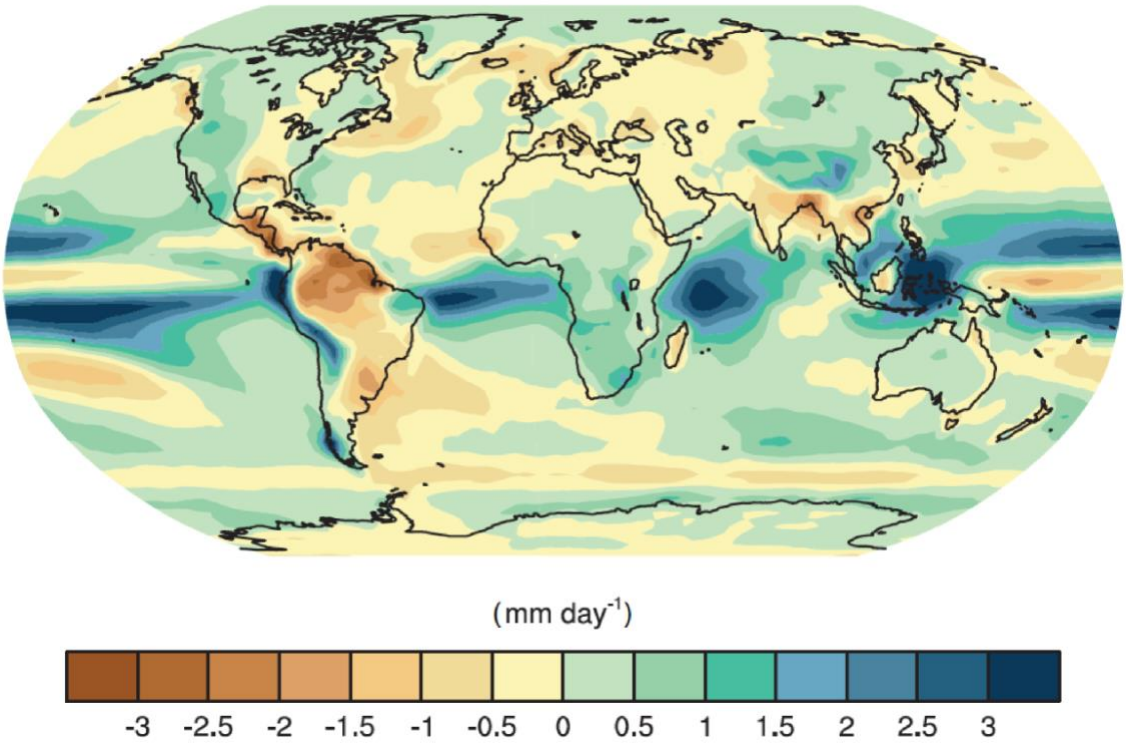

Figure 1.1 Biases of annual-mean precipitation rate in the multi-model-mean of all atmosphere-ocean coupled GCMs in CMIP5 historical simulations (1850-2005). Benchmark dataset for precipitation is from Global Precipitation Climatology Project (GPCP). Adapted from Fig. 9.4b in the Working Group One report of IPCC (2014).

Imperfections in GCM-simulated Amazonian rainfall have been historically viewed through the lenses of surface net radiation, terrestrial water availability, nearby Intertropical Convergence Zones (ITCZs), sea surface temperatures (SSTs) in adjacent oceans (Fernandes et al. 2015; Yin et al. 2012); treatments of cloud processes, land parameterizations (Sakaguchi et al. 2018; Zhang et al. 2017); strength of the South American Low-Level Jet (SALLJ) and its east-to-west moisture transport (Barros and Doyle 2018; Boers et al. 2017; Kooperman et al. 2018; Langenbrunner et al. 2019; Vizy and Cook 2007).

This chapter takes a different perspective by hypothesizing that Andean convection can remotely influence Amazonian rainfall in a west-to-east manner. If proven right, this hypothesis suggests that the Andes-Amazon ought to also be assessed in model evaluations, and implies that Amazonian rainfall biases in a model can be partially attributed to biases of convection and rainfall over the Andes.

The research objective of Chapter 4 is to better understand the role of Andean convection on Amazonian rainfall. In particular, this chapter answers the following research questions:
(1) How does Andean convection influence Amazonian rainfall? What are the spatial and temporal features characterizing its role?
(2) What is the dominant mechanism for Andean convection to exert a notable influence on precipitation over the Amazon? Can other mechanisms be ruled out?

1.5 Organization

Chapter 2 will first briefly review the GLACE protocol for historical context on background on a GCM experiment design that has become a standard for defining the soil moisture–precipitation coupling strength unambiguously, then introduce the seasonal hydrologic coupling metric using terrestrial water storage. Next, this chapter will reveal the effects of explicit convection by comparing new superparametreized vs. conventionally parameterized climate simulations, focusing on hydrologic land-atmosphere coupling on weekly-to-subseasonal timescales and examining implications on the atmospheric and terrestrial segments. Lastly, the effects of explicit convection on hydrologic land-atmosphere coupling on seasonal timescales will be shown.

The first part of Chapter 3 builds upon the GLACE-type simulations introduced in the second chapter and further uncovers the effects of explicit convection on *thermal* land-atmosphere coupling. In the second part of this chapter, after corroborating evidence using multiple experiment designs and various diagnostics, it will be shown that the effects of explicit convection on soil moisture–temperature coupling is robustly detectable over the Arabian Peninsula and the southwestern United States. Explicit convection reduces thermal coupling over the Arabian Peninsula due to reductions of the time-mean rainfall, while it enlarges the thermal coupling over the southwestern United States, which is related to enhancements of surface Bowen ratio. The final part of this chapter will present additional evidence showing that explicit convection systematically enhances land surface Bowen ratio in the present climate, and it also leads to predictions of a stronger amplification of future land Bowen ratio in a warmer climate compared to standard GCMs with conventionally parameterized convection.

The research in Chapters 2 and 3 was published in the *Journal of Advances in Modeling Earth Systems* as:

Qin, H., Pritchard, M. S., Kooperman, G. J., & Parishani, H. (2018). Global Effects of Superparameterization on Hydrothermal Land-Atmosphere Coupling on Multiple Timescales. *Journal of Advances in Modeling Earth Systems*, 10, 530–549.

Chapter 4 will focus on the remote control by Andean convective heating of Amazonian rainfall, regionally over South America. After descriptions of the experimental design, this chapter will present the characteristics of Andean convective forcing, followed by spatial and temporal features in the Amazonian rainfall responses. By testing multiple hypotheses from competing

frameworks for interpreting the causality underpinning tropical rainfall dynamics, it will be argued that changes in the moisture budget over the Amazon serve as a first-order control on Amazonian rainfall oscillations due to the vertical velocity anomalies galvanized by Andean convective forcing. As a consequence, features of the eastward expansion of the vertical velocity and moisture field in the middle troposphere will be described. The research in Chapter 4 is being prepared as a manuscript for publication in the *Journal of Advances in Modeling Earth Systems* as:

Qin, H., Pritchard, M. S., Terai, C., Bacmeister, J., & Bogenschutz, P., Understanding the Remote Influence of Andean Convection on Amazonian Rainfall. (*In preparation*)

Chapter 5 will summarize the major results and provide suggestions on future directions of follow up research.

Chapter 2. Effects of Explicit Convection on Global Hydrologic Land-Atmosphere Coupling Across Multiple Timescales

Adapted from:

Qin, H., Pritchard, M. S., Kooperman, G. J., & Parishani, H. (2018). Global Effects of Superparameterization on Hydrothermal Land-Atmosphere Coupling on Multiple Timescales. *Journal of Advances in Modeling Earth Systems*, 10, 530–549.

Abstract

Many conventional General Circulation Models (GCMs) in the Global Land–Atmosphere Coupling Experiment (GLACE) tend to produce what is now recognized as overly strong Land–Atmosphere (L–A) coupling. I investigate the effects of cloud Superparameterization (SP) on L–A coupling on timescales beyond diurnal where it has been recently shown to have a favorable muting effect hydrologically. Using the Community Atmosphere Model v3.5 (CAM3.5) and its Superparameterized counterpart SPCAM3.5, I conduct soil moisture interference experiments following the GLACE and Atmospheric Model Intercomparison Project (AMIP) protocols. The results show that, on weekly-to-subseasonal timescales, SP also mutes hydrologic L–A coupling. This is detectable globally, and happens through the evapotranspiration–precipitation segment. But on seasonal timescales, SP does not exhibit detectable effects on hydrologic L–A coupling.

2.1 Introduction

Land–atmosphere (L–A) interactions play a critical role in the energy balance and hydrological cycles [*Entekhabi et al.*, 1992; *Krakauer et al.*, 2010; *Seneviratne et al.*, 2010] and thus significantly influence weather and climate on local [*Chen and Avissar*, 1994; *Froidevaux et al.*, 2013], regional [*Kochendorfer and Ramírez*, 2005], to global [*Seneviratne et al.*, 2010] spatial scales and on diurnal [*Findell et al.*, 2011; *Schlemmer et al.*, 2011, 2012], seasonal [*Cook et al.*, 2006; *Khodayar and Schädler*, 2013], decadal and even centennial [*Seneviratne et al.*, 2010] temporal scales. Soil moisture is an especially important land variable in a variety of L–A feedbacks. Soil moisture affects evapotranspiration (ET), water vapor content in the overlying atmosphere, and affects Planetary Boundary Layer (PBL) stability by changing the surface Bowen ratio, thus influencing local temperature, convection, clouds and precipitation [*Hohenegger et al.*, 2009; *Krakauer et al.*, 2010; *Seneviratne et al.*, 2010]. Soil moisture can also have non-local and large-scale impacts [*Seneviratne et al.*, 2010; *Koster et al.*, 2014].

As reviewed by *Seneviratne et al.* [2010], L–A feedbacks can occur because soil moisture enhancement can lead to amplified ET (this link from soil moisture to ET is referred to as the terrestrial segment), which may or may not result in increased precipitation (this link from ET to precipitation is referred to as the atmospheric segment); in turn, increased precipitation contributes to more abundant soil moisture. The atmospheric segment, linking ET to precipitation, is the most uncertain within this process chain. For example, many studies disagree on the relationship between evaporation and precipitation over the eastern US [*Findell and Eltahir*, 2003; *Findell et al.*, 2011; *Guillod et al.*, 2014]. In one study, convection and precipitation are favored in conditions with either dryer or wetter soils, depending on the

inclusion of explicitly resolved convection or not [*Hohenegger et al.*, 2009]. Surface soil moisture heterogeneity on scales of tens of kilometers is reported to be important for rainfall initiation [*Taylor et al.*, 2011] and afternoon rainfall can be favored over regions dryer than surrounding areas [*Guillod et al.*, 2015]. Cloud cover, not always associated with precipitation, can be higher over either wetter or dryer soils depending on the moisture content and stability of the overlying free atmosphere [*Huang and Margulis*, 2011; *Chlond et al.*, 2014].

Despite the importance of L–A coupling, some fundamental puzzles remain unsolved. In the Global Land Atmosphere Coupling Experiment (GLACE) [*Koster et al.*, 2000, 2006], inter-model differences in the degree of soil moisture–precipitation are significant. For ease of description here and below, I will refer to coupling between land variables and precipitation as hydrologic L–A coupling (e.g., soil moisture–precipitation, land water storage–precipitation). Although a companion investigation to *Koster et al.* [2006] concluded that the multi-model mean of GLACE agrees with observations reasonably well [*Guo et al.*, 2006], criticisms of overly strong L–A coupling in General Circulation Models (GCMs) have been proposed by many more recent studies [*Wei et al.*, 2010; *Ferguson et al.*, 2012; *Phillips and Klein*, 2014; *Levine et al.*, 2016], albeit with at least one exception [*Mei and Wang*, 2012].

Model representations of land processes have been shown to play an important role [*Wei et al.*, 2010; *Medlyn et al.*, 2011; *Swenson and Lawrence*, 2014], and can be instrumental in determining the overall L–A coupling in terms of spatial and temporal variations [*Wei and Dirmeyer*, 2012]. For example, varying the representation of vegetation on the terrestrial segment of L–A coupling was shown [*Williams and Torn*, 2015] to improve summer climate in

central US in the single column Community Earth System Model v1.2.2 through prescribing Leaf Area Index (LAI), increasing leaf reflectivity, soil resistance to evaporation, and minimal stomatal conductance [*Williams et al.*, 2016].

Representations of atmospheric processes are also important to L–A coupling, as has been noted by sensitivities to the choices of PBL and cumulus schemes in a regional model (Hirsch et al. 2014) and changes of convection schemes in a GCM (Mei and Wang 2012); interactions between land surface and PBL (Santanello et al. 2009a; Santanello Jr et al. 2011; Santanello Jr et al. 2013); and simulations of the low frequency component of precipitation (Wei et al. 2010). Interestingly, Wei and Dirmeyer (2010) investigated the GLACE-type soil moisture–precipitation coupling strength in six combinations using two atmospheric models and three land surface schemes, and concluded that the main difference of coupling strength was due to the choice of atmospheric model rather than land surface scheme. In this chapter, I focus on a major update to the representation of atmospheric convection using an approach known as Superparameterization (SP, also known as Multiscale Modeling Framework, or "embedded explicit convection"), which replaces conventional parameterizations of deep convection, shallow convection and PBL turbulence with embedded Cloud-Resolving-Models (CRMs) [*Grabowski and Smolarkiewicz,* 1999; *Grabowski,* 2001; *Khairoutdinov and Randall,* 2001; *Randall et al.*, 2003]. It has been shown to have important consequences. Over the Central U.S. during summer, SP can alter canopy–rainfall interactions due to a more intense precipitation distribution, without the overly frequent drizzle and associated excessive canopy interception recycling found in conventional GCMs [*DeMott et al.*, 2007]. An improved rainfall intensity distribution is also evident at global scales relative to remotely sensed precipitation data TRMM

3B42 [*Kooperman et al.*, 2016], as is improved surface latent heat fluxes relative to in-situ derived data FLUXNET [*Mohr et al.*, 2013].

Recently, the first detailed analysis of SP from the perspective of modern coupling metrics showed that it favorably reduces hydrologic L–A coupling on subdaily timescales [*Sun and Pritchard*, 2016, SP16 hereafter]. But two limitations of SP16 are (1) the use of diagnostic correlative metrics of coupling and (2) the focus on short (subdaily) timescales of L–A coupling. It is still an open question whether or not similar effects of SP on L–A coupling can be confirmed using more causatively unambiguous metrics of GLACE, or on longer timescales in ways that might matter to weather and climate prediction. The main focus of this article is thus to reveal and understand the effects of SP on hydrologic on timescales beyond daily with an emphasis of results following the GLACE protocol.

2.2 Methods

2.2.1 Quantifying the hydrologic L-A coupling strength

2.2.1.1 GLACE experiment revisited

Previous attempts to isolate and quantify the effects of explicit convection on global hydrologic L–A coupling have relied on correlative metrics that are purely diagnostic (e.g. in SP16). To address this limitation, I first focus on a metric of coupling strength defined in GLACE [*Koster et al.*, 2006], which can be derived from mechanism denial interference experiments. This procedure is used for a climate model with and without explicit convection. Briefly, the method consists of two sets of experiments, each a 16-member ensemble hindcast spanning 1 Jun–31 Aug 1994, with perturbed initial conditions to sample atmospheric internal variability. In the first

set of experiments (called ensemble W, or ENS(W)), one ensemble member is randomly selected and its soil moisture is written to external files at every time step. Then in the second experiment (called ensemble S, or ENS(S)), subsurface (deeper than 5cm) soil moisture is prescribed from previous saved files at time step level for each ensemble member, thus surgically removing the soil moisture–atmosphere interactions. The idea is that the internal variability that produces differences between ensemble members will be stronger in ensemble W, due to full interactions between soil moisture and the atmosphere, than in ensemble S, in which soil moisture time series are artificially synchronized to be identical for all members. Thus a quantitative metric of the impacts of L–A interactions on simulated internal variability, with direct relevance to intrinsic predictability, can be obtained as the difference in a metric of ensemble "similarity," a converse to spread.

Following *Koster et al.* [2006], this similarity metric is calculated as follows. I neglect the first 8 days as spinup, and then reduce the following 84 daily mean precipitation values to six-day totals representing 14 samples. Within each set of hindcast experiments, I calculate the pan-ensemble standard deviation based on the full set of 224 six-day totals (i.e., 14 samples ×16 ensemble members) denoted by σ_p; I then calculate the standard deviation based on 14 six-day totals representing the ensemble mean time series calculated by averaging across the 16 ensemble members, denoted by $\sigma_{\hat{p}}$. Finally, I compute the similarity quantity from GLACE,

$$\Omega_p = \frac{16\sigma_{\hat{p}}^2 - \sigma_p^2}{15\sigma_p^2} \tag{2.1}$$

for both ensemble W and ensemble S, denoted by $\Omega_p(W)$ and $\Omega_p(S)$ respectively.
In ensemble S, soil moisture is synchronously prescribed to be identical in each ensemble member. In ensemble W, soil moisture is allowed to vary internally through atmospheric

feedbacks. The higher the enhancement of similarity in ensemble S relative to ensemble W, the larger the control of soil moisture on precipitation. Therefore, the soil moisture–precipitation coupling strength can be defined as $\Omega_p(S) - \Omega_p(W), or\ \Delta\Omega_p$, where P stands for precipitation. To assess statistical significance, Monte Carlo analysis was done to calculate the 95% confidence level of $\Delta\Omega_p$, finding it to be 0.057. This is consistent with the original GLACE study [*Koster et al.*, 2006] arguing 0.06 is significant at 95% confidence level for Ω difference.

It is worth noting that both soil liquid water and soil ice are prescribed in the original GLACE (Hauser et al. 2017; Koster et al. 2006b), while only soil liquid water are prescribed in our simulation set-up. Coincidentally, Hauser et al. (2017) recently pointed out that prescription of soil ice is not recommended for soil moisture prescription practices because it may cause large anomalies of surface temperature and ground heat flux.

2.2.1.2 Land–atmosphere coupling on seasonal timescales

The L–A coupling strength measured by the above GLACE protocol intrinsically focuses on weekly-to-subseasonal timescales. I expand our analysis by looking at coupling diagnostics on seasonal timescales using a strategy recently proposed in *Levine et al.*, [2016] (L16 hereafter). Terrestrial water storage anomaly (TWSA) typically has a marked seasonal cycle with a maximum ($TWSA_{max}$) and a minimum ($TWSA_{min}$), the interval between which is referred to as the drawdown interval, corresponding to the growing season of vegetation. L16 argued that empirically, if land water storage had a strong control on precipitation during the following months, there should be detectable correlations across independent years between $TWSA_{max}$ and the rainfall amount averaged over the drawdown interval ($Precip_{di}$). Similarly, if preceding precipitation had a strong control on terrestrial water storage, the interannual correlation of

averaged precipitation over the seasonal drawdown interval and the terrestrial water storage at the end of the interval should be strong. Therefore, the impact of TWSA on subsequent precipitation can be indirectly measured by what is called the "forcing metric", which is the correlation (Pearson's r) between $TWSA_{max}$ and $Precip_{di}$. The impact of preceding precipitation on subsequent TWSA can be indirectly measured by the correlation between $Precip_{di}$ and $TWSA_{min}$, called the "response metric". This correlation is computed over inter-annually varying pairs, separately at every land grid point location. Only inter-annual variability of the terrestrial water storage is retained by removing both the least square linear trend and the climatology of the seasonal cycle at every grid point.

2.2.2 Models and simulations

To assess the effects of explicit convection on L–A coupling on weekly-to-subseasonal timescales via the GLACE metric, 16-member ensemble hindcast simulations of June-July-August (JJA) 1994 with and without soil moisture synchronization were conducted. Each ensemble member has an initial temperature perturbation on a magnitude of round-off error ($1.0 \times 10^{-5} K$) to sample the atmospheric internal variability. I use the Community Atmosphere Model version 3.5 (CAM3.5) at T42 horizontal resolution (~2.8 degrees) and with 30 vertical levels, developed by National Center for Atmospheric Research (NCAR) [*Collins et al.*, 2004], and its Superparameterized counterpart SPCAM3.5, which was developed by Marat Khairoutdinov [*Khairoutdinov et al.*, 2005] and supported by the NSF Center for Multiscale Modeling of Atmospheric Processes (CMMAP).

In SPCAM3.5, within each grid column of the host GCM, a 32-column CRM with 4-km horizontal grid spacing replaces the conventional parameterizations of deep convection, shallow convection, and boundary layer turbulence. Both models are run with the Community Land Model version 3.5 (CLM3.5) [*Oleson et al.*, 2008]. Initial atmospheric conditions are interpolated from ERA-Interim Reanalysis [*Dee et al.*, 2011]. CLM3.5 was initialized in the same way as in SP16 using land variables from long-term climate simulations. Modifications to the CLM3.5 code (also relevant to modern versions of CESM) needed for soil moisture writing and reading capabilities were engineered as illustrated in Figure A1, where I make them available to the CESM user community.

In a complementary set of long, free-running experiments, I followed the Atmospheric Model Intercomparison Project (AMIP) protocol to assess the effects of explicit convection on L–A coupling on seasonal timescales and for additional analysis. Both CAM3.5 and SPCAM3.5 were run for 1996-2015 with prescribed sea surface temperature (SST) and sea ice [*Hurrell et al.*, 2008] and the time period of this AMIP-type simulation was chosen to allow consistent validation against constraints from the Gravity Recovery And Climate Experiment (GRACE) satellite records.

2.3 Results

2.3.1 Hydrologic L-A coupling on weekly-to-subseasonal timescales

In CAM3.5, most continental interiors including North America, tropical South America, tropical Africa, central Eurasia and East Asia are hotspots of strong hydrologic coupling (Figure 2.1a). In contrast, in SPCAM3.5, a systematic reduction of the coupling strength can be seen

nearly everywhere. The only exception is a regional enhancement over Northern Mexico (Figure 2.1b), which I will show later is linked to a local enhancement of the terrestrial segment of L–A coupling. I note that the presence of small negative values in the $\Delta\Omega_p$ metric is not physically interpretable; such negative values attest to a degree of stochasticity in this type of analysis as discussed by *Koster et al.* [2006]. Thus, it is important to consider these results in broad geographical context, and in relation to a full suite of complementary metrics as evaluated below. Since CAM3.5 and SPCAM3.5 share an identical land model, it is logical to expect that the reductions in overall coupling occur through the atmospheric, rather than the terrestrial segment. I quantify their relative contribution by decomposing the soil moisture–precipitation (SM–P) coupling into soil moisture–ET (SM–ET) coupling (the terrestrial segment) and ET–precipitation (ET–P) coupling (the atmospheric segment). Following *Guo et al.*, [2006], measurement of the terrestrial segment, C_T, can be expressed as a GLACE-type metric for ET multiplied by the standard deviation of ET in ensemble W, i.e.,

$$C_T = (\Omega_{ET}(S) - \Omega_{ET}(W)) \times \sigma_{ET}(W), \tag{2.2}$$

and is calculated for every land point. The latitude-weighted global mean (latitude from 30°S to 60°N) of the terrestrial coupling is then calculated. For overall consistency, quantification of the atmospheric segment is calculated by dividing the global mean of SM–P coupling by that of the terrestrial segment. The results shown in Table 2.1 confirm that, for the global mean, the reduction of overall coupling strength in SPCAM3.5 comes from the reduction in ET–P coupling, highlighting the importance of the atmospheric segment. Therefore, globally speaking, on weekly-to-subseasonal timescales, explicit convection reduces the SM–P coupling via reducing the atmospheric segment.

This is consistent with recent findings on the effects of explicit convection on shorter timescales. In SP16, on subdaily timescales, CAM3.5 was found to produce systematically higher sensitivity of afternoon rainfall occurrence to morning evaporative fraction changes than SPCAM3.5. The reduced subdiurnal coupling under SP was in turn in better agreement with precipitation-assimilating regional reanalysis over the US. One implication of our discovery of a consistent effect of SP in the GLACE metric is that the same mechanism that realistically mutes coupling on subdaily timescales may also impact coupling on weekly-to-subseasonal timescales. From the perspective of criticisms on overly strong coupling strength in conventionally parameterized climate models [*Wei et al.*, 2010; *Ferguson et al.*, 2012; *Phillips and Klein*, 2014; *Levine et al.*, 2016], such a reduction could be viewed as an improvement, though it is difficult to consistently validate the model-based GLACE metric using observations due to its dependence on an artificial mechanism denial.

The GLACE result has an interesting implication for subseasonal-to-seasonal predictability in superparameterized frameworks. The systematic reduction of SM–P coupling in SPCAM3.5 indicates that when explicit convection is used, there is less intrinsic synoptic predictability of precipitation from knowledge of soil moisture. This message is relevant to ongoing attempts to exploit the benefits of SP to enhance subseasonal-to-seasonal predictions [*Goswami et al.*, 2015; *Subramanian and Palmer*, 2016, 2017; *Düben et al.*, 2017] — while more midlatitude predictability might be expected from teleconnections linked to enhanced simulations of slow tropical modes like the Madden-Julian Oscillation (MJO) using SP [*Benedict and Randall*, 2009], our results suggest a reason to expect less predictability from assimilation of local soil moisture.

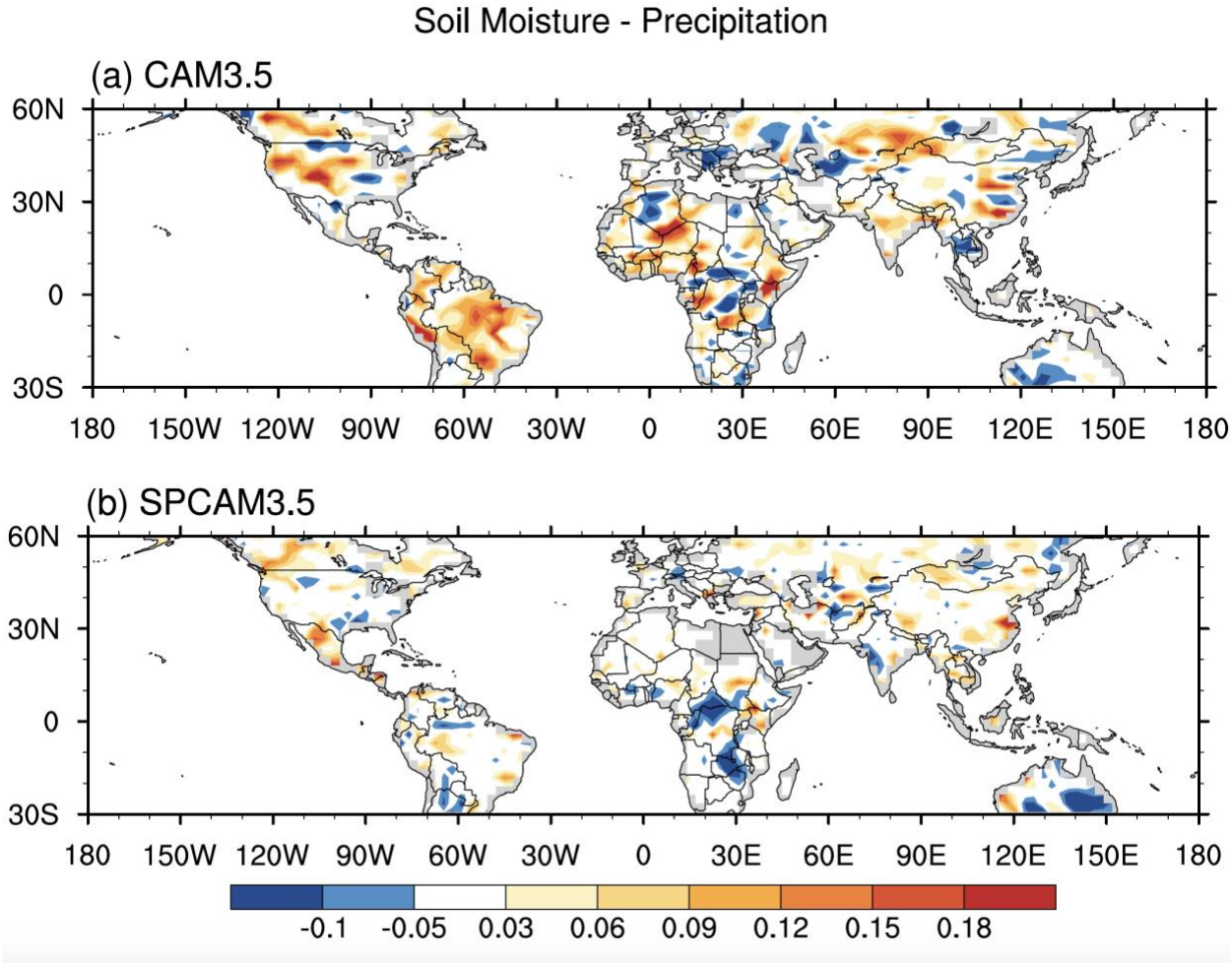

Figure 2.1 Soil moisture–precipitation coupling strength revealed by $\Delta\Omega_p$ from (a) CAM3.5 and (b) SPCAM3.5. $\Delta\Omega_p$ is significant at 95% confidence level where it's larger than 0.06. The color bar is irregular and set to be the same as in Koster et al. (2006b).

Table 2.1 Global mean strength of soil moisture–precipitation coupling (SM–P), terrestrial segment coupling (SM–ET), and atmospheric segment coupling (ET–P) in CAM3.5 and SPCAM3.5, latitude-weighted (latitude from 30°S to 60°N).

	SM-P	SM-ET	ET-P
CAM3.5	0.0175	0.0249	0.7028
SPCAM3.5	0.0046	0.0368	0.1250

2.3.2 Hydrologic L-A coupling on seasonal timescales

As pointed out in L16, previous studies do not agree on the sign and magnitude of L–A coupling and many focus on short (daily-to-synoptic) timescales. To test whether the striking sensitivity of

SP on hydrologic L–A coupling on these short timescales has implications for longer term hydrologic variability, I extend our analysis to seasonal timescales using the forcing metric and response metric defined in L16. In order to validate the model performance, I use monthly precipitation data from the Global Precipitatoin Climatology Project (GPCP) version 2.3 [*Adler et al.*, 2003, 2011; *Huffman et al.*, 2009] and monthly TWSA from the GRACE mission's Level-3 gridded land data [*Landerer and Swenson*, 2012]. Missing values in the latter are replaced using linear interpolation.

As shown in Figure 2.2, in observations and models, the forcing metric — as a measure of the impact of preceding terrestrial water storage on atmospheric precipitation during subsequent months — is consistantly weak. The response metric, as a measure of the impact of preceding atmospheric precipitation on subsequent terrestrial water storage, is much stronger. This is understandable because the impact of precipitation on land water state is more direct and should be more detectable than the reverse. In contrast to the striking differences in coupling between SPCAM and CAM seen on weekly-to-subseasonal timescales (Figure 2.1), coupling strength is remarkably similar on seasonal timescales for both the forcing and the response metric.

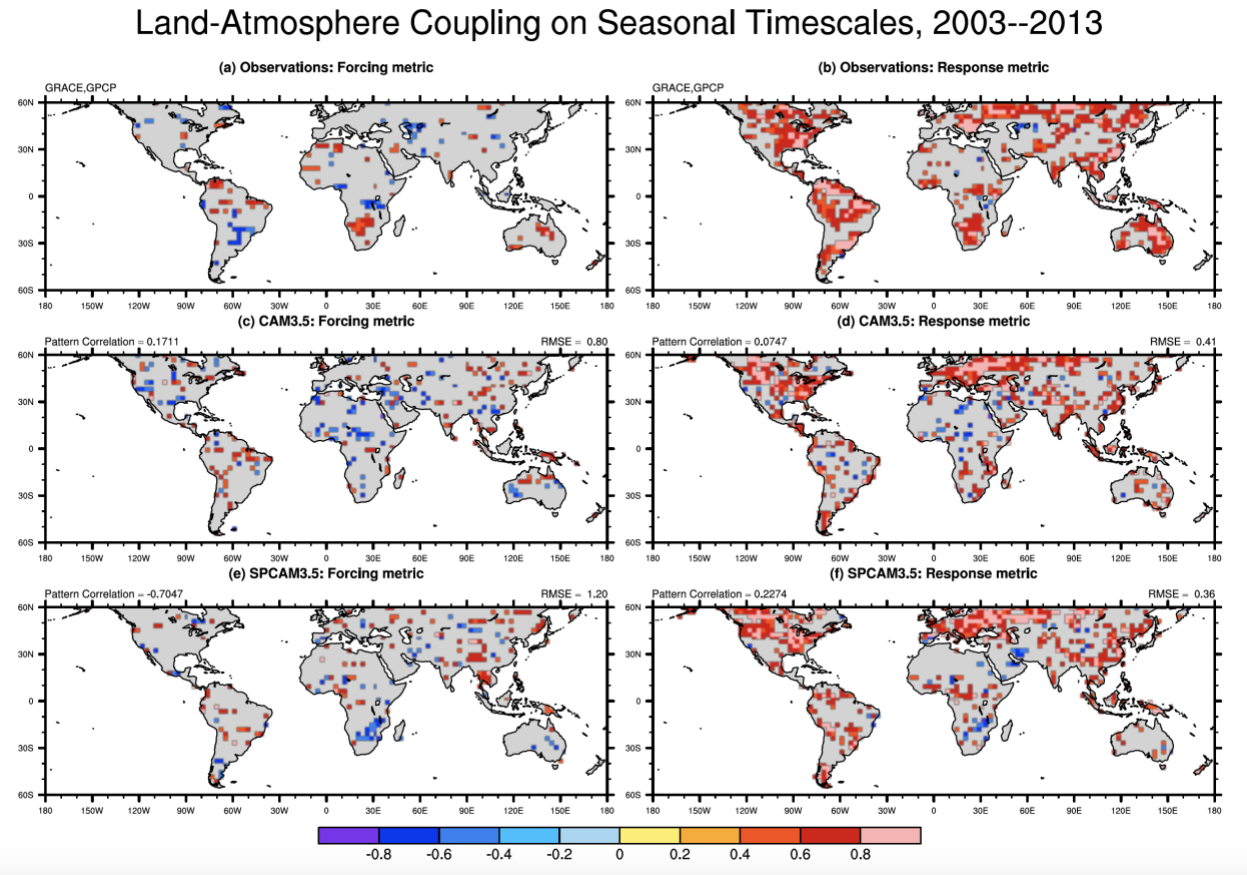

Figure 2.2 Land–atmophere coupling measured by the forcing metric (left column) and the response metric (right column) for 2003-2013 based on (a,b) GPCP and GRACE; and based on AMIP simulations from (c,d) CAM3.5 and (e,f) SPCAM3.5. Areas where correlation is not significant (significance level set to be 0.1) are shown in grey. In (c-f), numbers are latitude-weighted pattern correlation between models and observations at the upper left, and latitude-weighted Root-Mean-Square Error (RMSE) at the upper right. Latitudes are limited between 60°S and 60°N.

In summary, based on a set of metrics that attempt to quantify similar aspects of local L–A coupling, I have found evidence of time-scale dependence in the effects of SP on hydrologic coupling. On subdaily timescales, SP fundamentally changes hydrologic L–A coupling measured by triggering feedback strength, which was proposed by Findell et al. (2011) to delineate how afternoon rainfall occurrence changes with evaporative fraction, as seen in SP16. On weekly-to-subseasonal timescales, our results show that SP also has a systematic impact on the hydrologic L–A coupling as measured by the GLACE-type metric.

I suspect a strong oceanic control and more non-local influences on precipitation for longer timescales. This might help explain why SP's systematic effects on hydrologic L–A coupling manifest on subdaily and weekly-to-subseasonal timescales, but vanish over seasonal timescales, at least as measured by the seasonal coupling metric of L16, and in simulations in which SSTs are prescribed. Another possibility is that differences of the experiment and diagnostic design between GLACE-type soil moisture–precipitation coupling metric and the seasonal coupling metric of L16 play a role in differentiating the response.

2.4 Conclusion

L–A coupling is important to regional climate and weather prediction. Focusing on hydrologic coupling on timescales beyond daily, I have analyzed the effects of including explicit representations of cloud processes on global L–A coupling (by using SP). On weekly-to-subseasonal timescales, based on the GLACE-type metric, the results show that explicit convection systematically mutes soil moisture–precipitation coupling by reducing the atmospheric segment. This tends to confirm the recent findings of reduced coupling under SP on subdaily timescales, i.e., smaller sensitivity of afternoon rainfall occurrence to morning evaporative fraction changes in SP16, and shows this muting extends to weekly-to-subseasonal timescales. This implies that realistic treatment of convection will reduce the contribution of initial state of soil moisture to intrinsic rainfall predictability. On seasonal timescales, hydrologic L–A coupling mainly manifests on the response segment (the impact of precipitation on land water storage), and the forcing segment (the impact of land water storage on precipitation) is weak, perhaps due to greater oceanic controls on seasonal precipitation. Unlike on shorter

timescales, the effects of explicit convection on hydrologic L–A coupling are undetectable on seasonal timescales.

I acknowledge physical limitations of the standard implementation of SP used in the models I have analyzed, which limits the degree to which these sensitivities should be presumed to inform understanding of nature. While several of the sensitivities appear promising relative to observational constraints, there is the philosophical concern that real L–A coupling operates through the system of real boundary layer turbulence and shallow cumulus convection, which requires 3D grid spacing approaching 50-m to satisfyingly resolve vertical mixing. In contrast, the 2D CRMs with 200-m vertical (4-km horizontal) grid spacing used in SPCAM heavily under-resolve, and over-parameterize, the relevant atmospheric physics, even if they are a step towards more "explicit" than conventional parameterization approaches. *Xu et al.* [2017] recently showed that addressing this shortcoming by augmenting SP with a higher-order subgrid turbulence parameterization significantly modifies simulated surface flux partitioning and the Bowen ratio's climate sensitivity. It would likewise be interesting to know if "ultra-parameterized" configurations of SPCAM [*Parishani et al.*, 2017] with radically refined resolution in the PBL exhibit modified L–A coupling.

Chapter 3. Effects of Explicit Convection on Global Thermal Land-Atmosphere Coupling and Impacts on Land Surface Bowen Ratio

Adapted from:

Qin, H., Pritchard, M. S., Kooperman, G. J., & Parishani, H. (2018). Global Effects of Superparameterization on Hydrothermal Land-Atmosphere Coupling on Multiple Timescales. *Journal of Advances in Modeling Earth Systems*, 10, 530–549.

Abstract

I investigate the effects of cloud Superparameterization (SP) on the thermal Land–Atmosphere (L-A) coupling in this chapter. Using the Community Atmosphere Model v3.5 (CAM3.5) and its Superparameterized counterpart SPCAM3.5, I conducted soil moisture interference experiments following the GLACE and Atmospheric Model Intercomparison Project (AMIP) protocols. Two robust regional effects of SP on thermal L–A coupling are found and explored. Over the Arabian Peninsula, SP reduces thermal L–A coupling through a straightforward control by mean rainfall reduction. More counterintuitively, over the southwestern US and northern Mexico, SP enhances the thermal L–A coupling in a way that is independent of rainfall and soil moisture. This signal is associated with a systematic and previously unrecognized effect of SP that produces an amplified Bowen ratio, and in hindsight is detectable in multiple SP model versions and experiment designs. In addition to amplifying the present-day Bowen ratio, SP is found to amplify the climate sensitivity of Bowen ratio as well, which likely plays a role in influencing climate change predictions at the L–A interface.

3.1 Introduction

Soil moisture and associated L–A coupling are of great importance in operational Numerical Weather Prediction (NWP) [*Seneviratne et al.*, 2010; *Barthlott and Kalthoff*, 2011; *Koster et al.*, 2011], and contribute to continental summer warm biases seen in both NWP and climate simulations [*Cheruy et al.*, 2014; *Van Weverberg et al.*, 2015]. Soil moisture conditions can also play a role in sustaining and amplifying temperature extremes and droughts [*Entekhabi et al.*, 1992; *Hong and Kalnay*, 2000; *Fischer et al.*, 2007a, 2007b; *Lorenz et al.*, 2010; *Jaeger and Seneviratne*, 2011]. Downstream effects include higher summer temperature variability and possibly enhanced temperature extremes, which have been demonstrated in eastern and central Europe and the Great Plains over North America [*Seneviratne et al.*, 2006; *Mueller and Seneviratne*, 2012; *Teng et al.*, 2016]. Furthermore, L–A coupling is projected to strengthen in a warmer climate [*Dirmeyer et al.*, 2012, 2014], which may contribute to increases in the frequency or intensity of these extreme events.

A basic soil moisture – surface temperature coupling concept can be described as follows. A decrease in ET (latent heat flux), resulting from a negative soil moisture anomaly, may lead to higher sensible heat flux and promote positive temperature anomalies in the air above the surface, possibly feeding back to soil moisture depletion by creating a larger atmospheric water vapor deficit [*Seneviratne et al.*, 2010]. For convenience, I refer to the coupling between soil moisture and near-surface temperature as thermal L–A coupling. In this chapter, I investigate the effects of SP on the *thermal* pathway of L–A coupling which directly influences temperature extremes.

3.2 Methods

3.2.1 Thermal L-A coupling strength measured by the GLACE metric

Firstly, we compute the similarity quantity from GLACE for near-surface temperature,

$$\Omega_T = \frac{16\sigma_{\hat{T}}^2 - \sigma_T^2}{15\sigma_T^2} \tag{3.2}$$

for both ensemble W and ensemble S, denoted by $\Omega_T(W)$ and $\Omega_T(S)$ respectively. The soil moisture–temperature coupling strength can be defined as $\Omega_T(S) - \Omega_T(W), or\ \Delta\Omega_T$, where T stands for 2-meter air temperature. To assess statistical significance, Monte Carlo analysis was done to calculate the 95% confidence level of $\Delta\Omega_T$, finding it to be 0.0561. This is consistent with the original GLACE study [*Koster et al.*, 2006] arguing 0.06 is significant at 95% confidence level for Ω difference.

3.2.2 Terrestrial coupling index

In *Dirmeyer* [2011], a metric of terrestrial coupling strength is proposed as:

$$I_\phi = S_W \beta_\phi, \tag{3.3}$$

where I_ϕ is the terrestrial coupling index for surface flux ϕ, S_W is the standard deviation of daily soil moisture at a given level, β_ϕ is the linear regression coefficient between soil moisture and surface flux ϕ. Very often ϕ is chosen to be the surface latent heat flux in W/m^2 and the index I_ϕ is therefore in units of W/m^2. Such an index is only retained when the Pearson's r correlation between soil moisture and variable ϕ is significant at the 99% confidence level.

Furthermore, the above index can be easily modified into a soil moisture–sensible heat flux coupling or soil moisture–temperature coupling index in which ϕ is replaced with sensible heat flux or 2-meter air temperature.

3.2.3 Additional simulations

We also analyze a set of pre-existing simulations from multiple model versions in discussing SP's effects on the Bowen ratio and its climate sensitivity. These included conventional and SP simulations of the Representative Concentration Pathway 8.5 (RCP8.5, years 2006 to 2100) emissions scenario using the Community Climate System Model v4 (CCSM4), and pre-industrial (i.e. 285 ppm) and 4xCO_2 (i.e. 1140 ppm) scenarios with the Community Earth System Model v1 (CESM1). CCSM4 was run with conventional and SP versions of the CAM4 as its atmospheric component, and CESM1 was run for two sets of simulations using both CAM4 and CAM5 as its atmospheric component. All of these simulations were run in a fully coupled configuration with interactive atmosphere, land, ocean, and sea-ice components. More details about these simulations are provided in *Stan and Xu* [2014], *Arnold et al.* [2014], and *Kooperman et al.* [2016a, b].

3.3 Results

3.3.1 Soil moisture–temperature coupling

Here I investigate the effects of SP on soil moisture–temperature coupling, or thermal L–A coupling, which has direct relevance to temperature extremes and has not been studied as extensively as hydrologic L–A coupling.

Unlike its effects on hydrologic coupling, which I have shown are systematic and visible on a global scale, effects of SP on thermal L–A coupling are regionally limited. Figure 3.1 shows that thermal coupling in SPCAM3.5 is significantly reduced over the Arabian Peninsula, slightly enhanced over parts of South America, and drastically enhanced over the Southwestern US and northern Mexico (SW US hereafter).

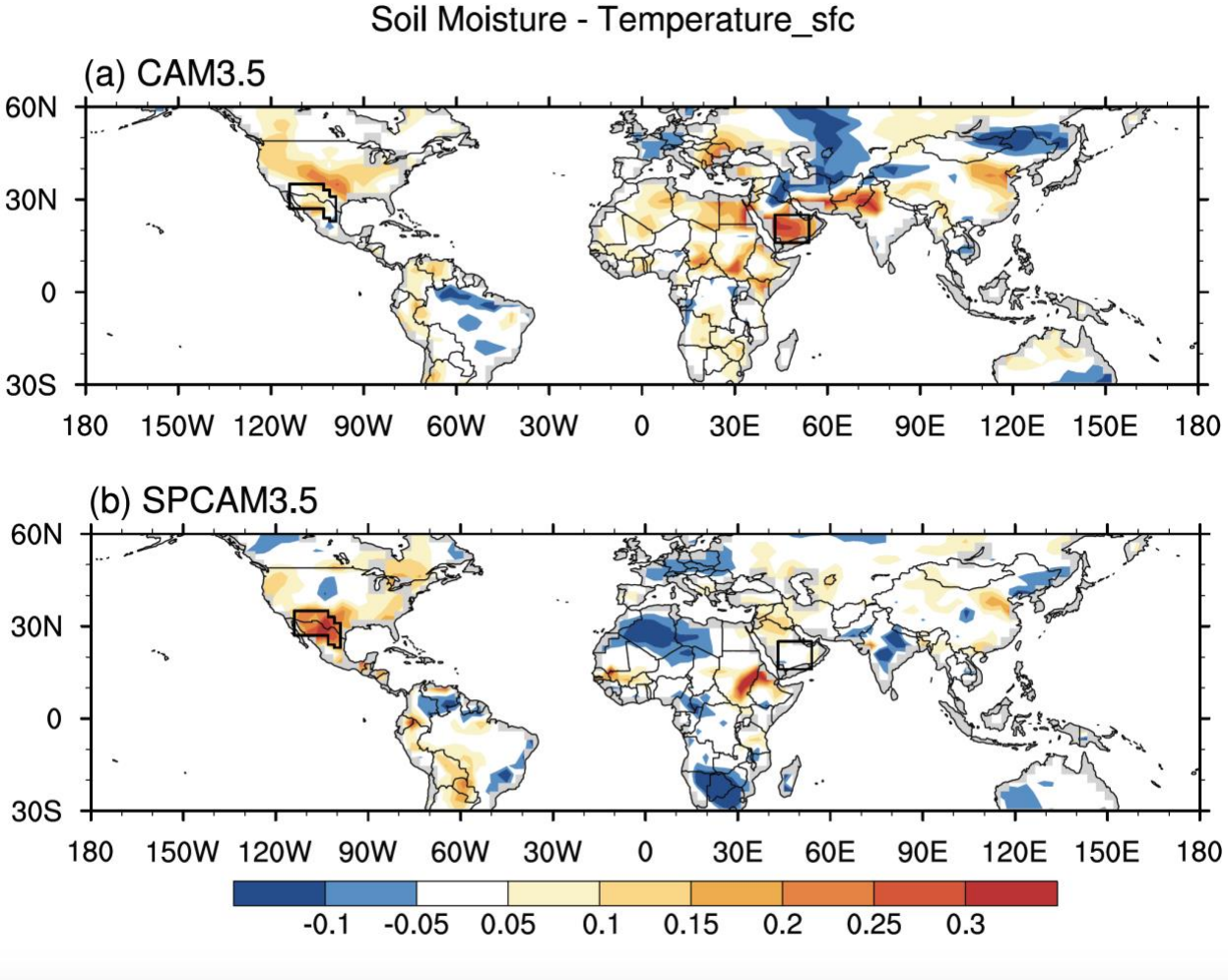

Figure 3.1 Soil moisture–2m air temperature coupling strength revealed by $\Delta\Omega_T$ from (a) CAM3.5 and (b) SPCAM3.5. $\Delta\Omega_T$ is significant at 95% confidence level where it is larger than 0.06. The color bar is irregular and set to be the same as in Koster et al. (2006b).

Since these effects of SP on thermal coupling are not globally systematic and have not been previously reported, I first test the signal's resilience beyond the GLACE experiment before

proceeding to understand it. This is done by applying an independent diagnostic coupling metric — the terrestrial coupling index introduced by Dirmeyer (2011), to a complementary pair of long free-running AMIP-style simulations. Compared to CAM3.5, the terrestrial coupling index for both latent heat flux (Figure 3.2 a,b) and sensible heat flux (Figure 3.2 c,d) confirm that SP produces local enhancements of coupling over the SW US, as well as India; and reductions of coupling over the Arabian Peninsula. I conclude that the main differences of thermal coupling between CAM3.5 and SPCAM3.5 initially suggested by the GLACE-type experiments are robust in the sense that they seem immune to the diagnostics chosen and the type of simulations performed.

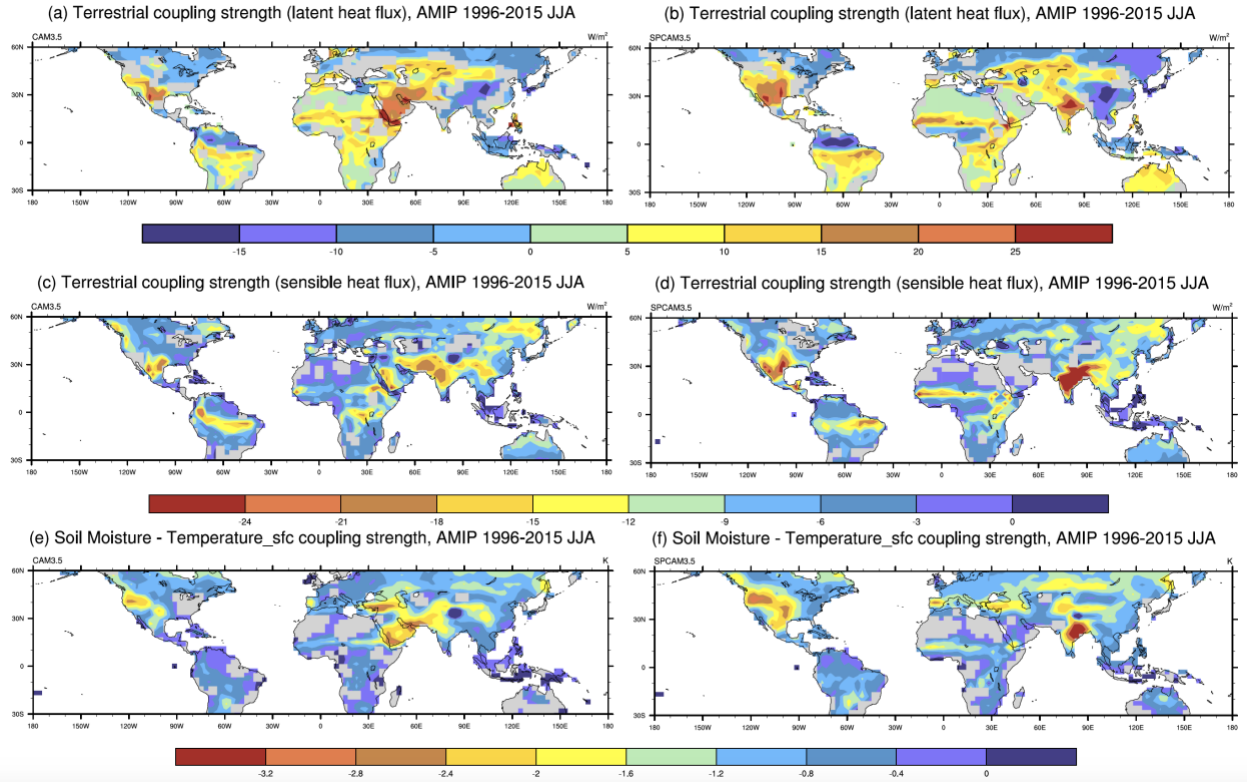

Figure 3.2 Based on 1996-2015 AMIP simulation, June-July-August (JJA) terrestrial coupling index (Dirmeyer 2011) applied to latent heat flux from (a) CAM3.5 (b) SPCAM3.5; and applied to sensible heat flux from (c) CAM3.5 (d) SPCAM3.5; and applied to 2m air temperature coupling from (e) CAM3.5 (f) SPCAM3.5; Soil moisture chosen to be soil liquid water in kg/m^2, at 0.12m depth.

In the following subsections, I hone in on Arabia and SW US (illustrated in Figure 3.1) for further analysis in order to understand why SP changes the thermal L–A coupling regionally.

3.3.1.1 Reduced Arabian coupling as a result of SP's reduction of time mean rainfall

Based on multiple lines of evidence, the Arabian Peninsula is one region where SPCAM is superior in simulating time-mean JJA precipitation relative to regular CAM. Over the Arabian Peninsula, both the mean and standard deviation of boreal summer precipitation are biased high in CAM3.5 while they are less biased in SPCAM3.5 in the AMIP-type simulations relative to GPCP datasets (Figure B1). This appears to be a robust effect of SP also seen in earlier versions of SPCAM/CAM, JJA mean precipiation over the Arabian Peninsula was more realistically simulated in SPCAM3.0 while CAM3.0 overestimated the mean precipitation [*Khairoutdinov et al.*, 2005]. In more recent versions of SPCAM5/CAM5, the mean and standard deviation of JJA precipitation is also better simulated in SP over the Arabian Peninsula (Jian Sun, personal communication).

Given the striking reduction of JJA time mean rainfall over the Arabian peninsula (Figure 3.3), it is reasonable to expect that these changes in rainfall when using SP play an overarching role in reducing the thermal coupling in this region. This follows ideas from previous studies [*Guo et al.*, 2006; *Seneviratne et al.*, 2010; *Dirmeyer*, 2011] suggesting that strong L–A coupling generally occurs in regions with moderate amounts of soil moisture — neither too dry, nor too wet. Such regions are called "transitional zones". From this perspective, mean rainfall through its effect on mean soil moisture may be considered as a first-order control on L–A coupling. I hypothesize that under CAM3.5, soil moisture is being pushed towards such "transitional" values due to relatively high mean precipitation in a region that should be drier, contributing to stronger

thermal coupling. While under SPCAM3.5, soil moisture is lower than "transitional" values due to less and more realistic mean precipitation, generating weaker thermal coupling.

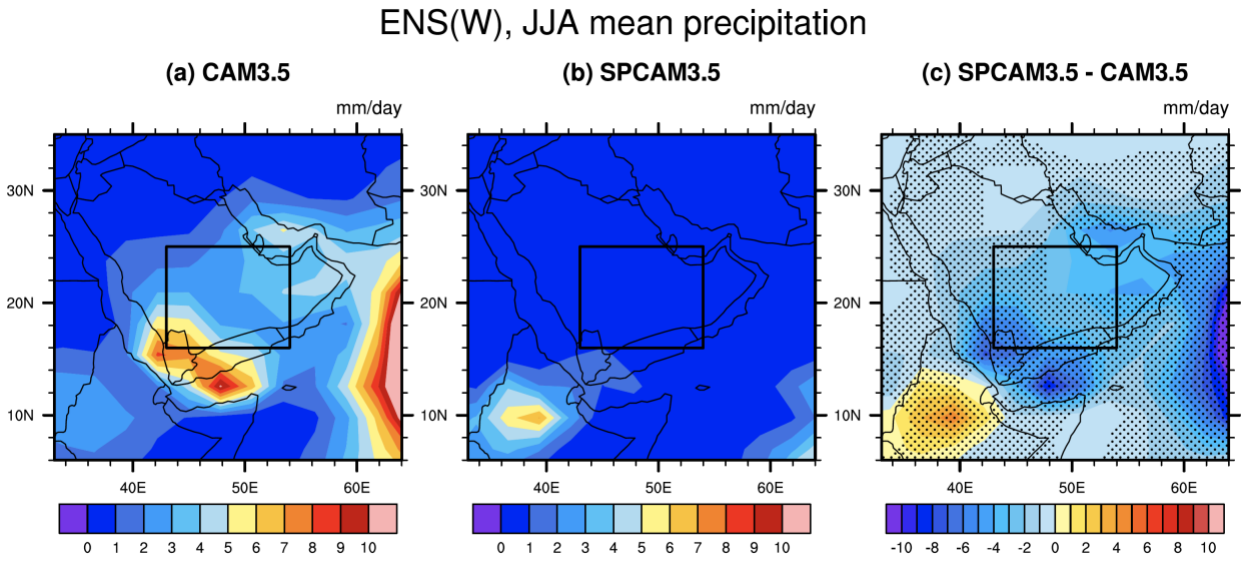

Figure 3.3 Based on ENS(W) over the Arabian Peninsula, JJA mean precipitation in (a) CAM3.5; (b) SPCAM3.5; and (c) differences of JJA mean precipitation between SPCAM3.5 and CAM3.5, stippling is based on controlling False Discovery Rate (FDR) (Wilks 2016) by choosing $\alpha_{FDR} = 0.1$. Assuming synoptic temporal scale (weekly) precipitation is nearly independent, original sample size is reduced by a factor of 7 to account for temporal autocorrelation in the Student's t test.

Detailed regional analysis of the Probability Density Functions (PDFs) of Arabian surface net radiation, latent heat flux, sensible heat flux, and volumetric soil moisture broadly confirms this view (Figure 3.4). SPCAM3.5's climate is fairly arid over the Arabian Peninsula. Compared to CAM3.5, precipitation is mostly confined below 4mm/day when using SP (Figure 3.3b), contributing to smaller soil moisture both at near-surface levels (Figure 3.4e,f) and deeper levels (Figure B2). Despite larger surface net radiation (resulting from less cloud cover, Figure 3.4d) demanding higher evaporative cooling (Figure 3.4a), surface latent (sensible) heat flux is much lower (higher) when using SP (Figure 3.4b,c), presumably due to soil moisture limitations.

In summary, the reason SP reduces thermal L–A coupling over the Arabian region appears to be relatively straightforward — due to regionally reduced time mean precipitation. The same control likely explains similar reductions in coupling noted but not explained for this region in SP16 (seen in their Figure 1a,b).

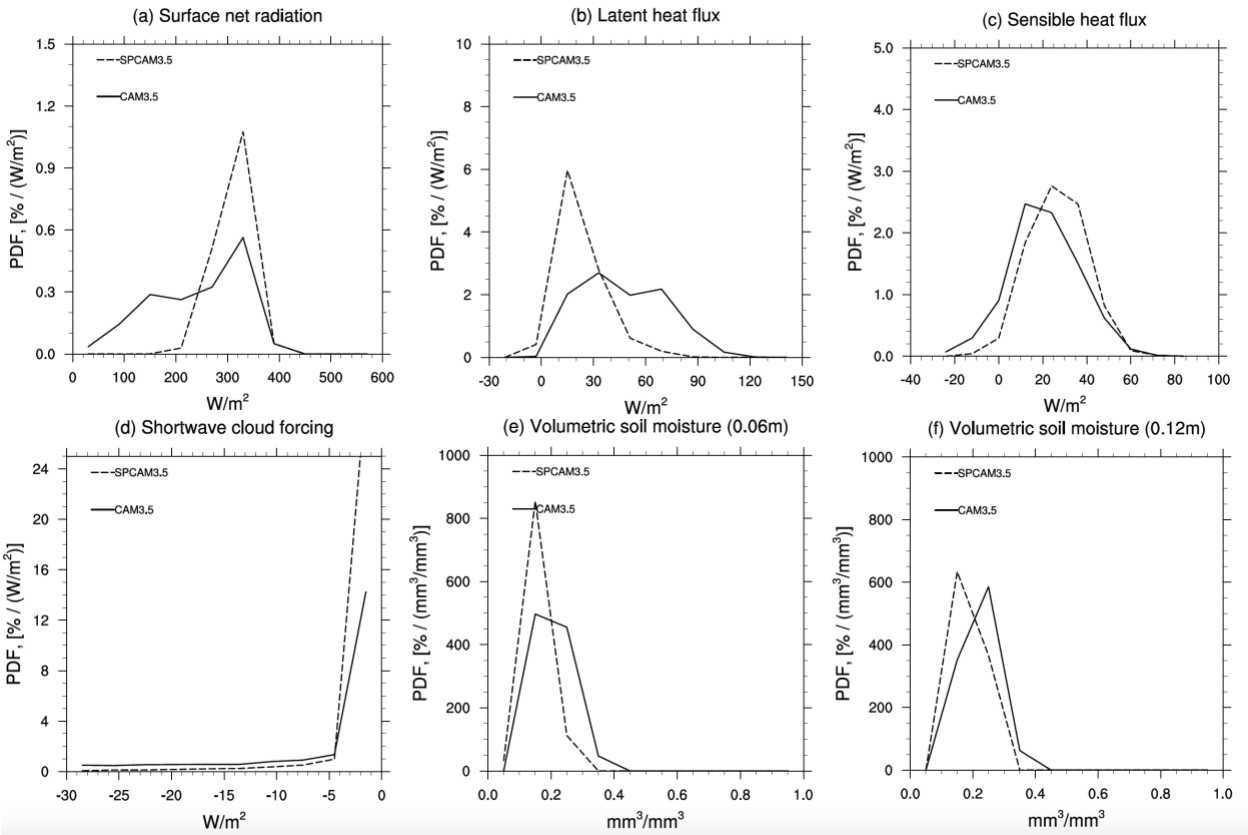

Figure 3.4 Based on ENS(W), probability density functions (PDFs) using daily samples within the Arabian box (as outlined in black in Figure 3) from CAM3.5 (solid lines) and SPCAM3.5 (dashed lines) of (a) surface net radiation, (b) surface latent heat flux, (c) sensible heat flux, (d) shortwave cloud forcing, (e) volumetric soil moisture at 0.06m in depth, and (f) volumetric soil moisture at 0.12m in depth.

3.3.1.2 Enhanced SW US coupling independent of rainfall

Unlike the Arabian region, first order effects of SP on precipitation cannot explain why it strongly enhances thermal coupling over the SW US region, where precipitation differences between the two models are neither universally positive nor negative within the region (Figure B3), and the median, lower and upper quartiles of the soil moisture are very similar at all depths

(Figure B4). The implication, given that SPCAM3.5 exhibits a remarkable enhancement of thermal coupling throughout a large region compared to CAM3.5 (Figure 3.1a,b), is that there must be another factor independent of mean precipitation or its associated soil moisture abundance that can produce enhanced thermal coupling under SP.

One potentially important pathway may be through the effects of SP on the intensity distribution of rainfall, for instance by removing an unrealistic drizzle mode that has been shown to produce artifical canopy reevaporation feedbacks [*DeMott et al.*, 2007]. However, after removal of drizzling samples in which daily rainfall is less than 0.1 mm/day, SP still highlights enhancements of the terrestrial coupling index of thermal coupling over the SW US relative to conventional CAM3.5, and such regional enhancement features are insensitive to the selection of drizzling threshold ranging from 1.0×10^{-5} to 0.1 mm/day (Figure B5). This argues against the idea that SP's modification of the rainfall distribution is responsible for enhanced thermal coupling over SW US. In the subsequent section I investigate other potential pathways that could influence thermal coupling strength by focusing on simulated differences in the Bowen Ratio.

3.3.2 Bowen Ratio control

Soil moisture can influence the near-surface temperature through its impact on surface energy partitioning, which can be characterized by the ratio of sensible to latent heat fluxes, or Bowen ratio. It is also important to note that the Bowen ratio tends to discriminate conditions of stronger or weaker relationship between near-surface temperature and surface soil moisture. This is visible as a dominant relationship in diagnostics of model output, in both SPCAM and CAM.

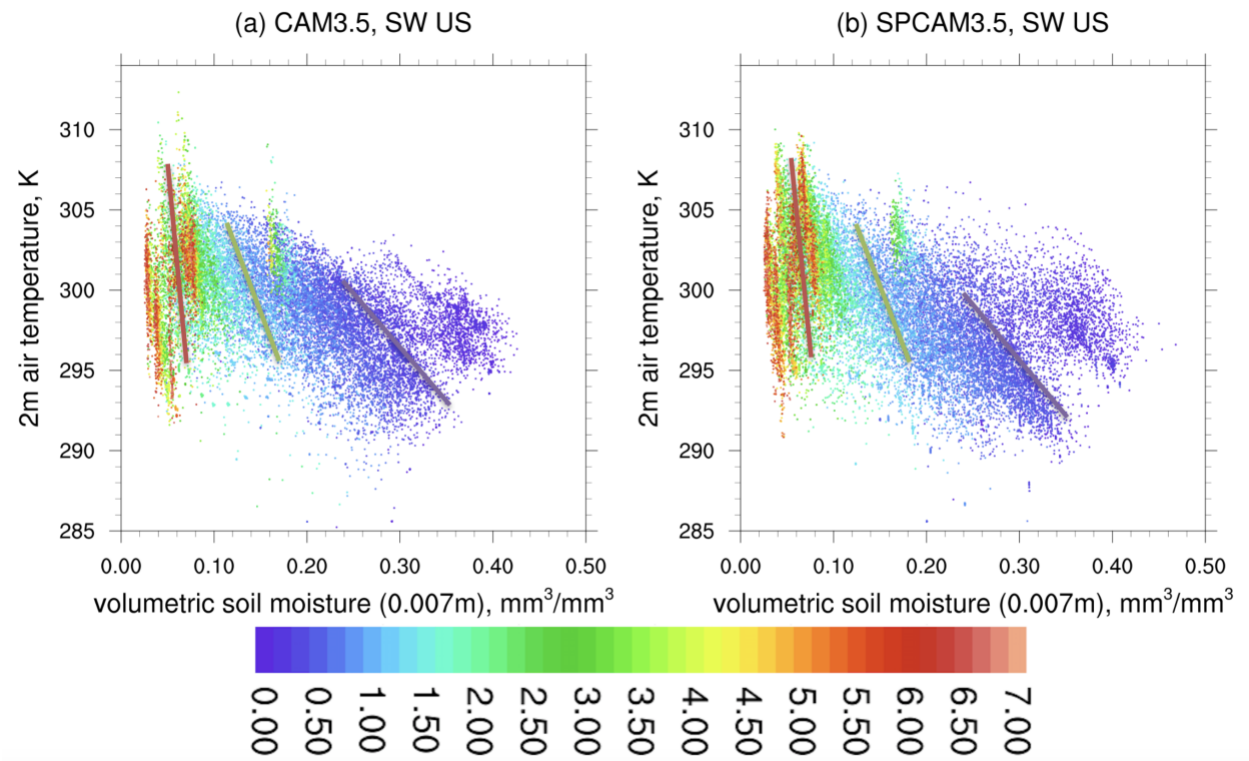

Figure 3.5 Based on daily samples in ENS(W) over the Southwestern US and Northern Mexico (as outlined in black in Figure 3) during boreal summer, scatter plots between surface volumetric soil moisture (0.007m depth) and 2m air temperature in (a) CAM3.5 and (b) SPCAM3.5. Samples are colored based on the magnitude of their Bowen ratio. The lavender, green and red line segments are the same in both subpanels and are added only for the purpose of illustrating that larger Bowen ratio is associated with steeper slope.

Figure 3.5 shows a scatter plot of soil moisture and 2m air temperature, using colors to disciminate samples (with varying days and locations) within the SW US region by their Bowen ratio. At higher Bowen ratio, 2m air temperature is more sensitive to changes in soil moisture, as evidenced by the sub-clusters of the phase space exhibiting increasing dependency (steeper slopes) between soil moisture and the y-axis. Of course Bowen Ratio is not the only factor important to coupling – for instance, despite the fact that the strongest dependency between surface volumetric soil moisture and 2m air temperature occurs at the driest regime of soil moisture (dots in red colors) in both models, the strongest coupling is likely at slightly higher soil moisture bins, since sufficient background soil moisture is also a prerequisite (Dirmeyer 2011; Seneviratne et al. 2010b). But the point is that Bowen Ratio is a relevant factor, such that

model differences in its statistics – especially in soil moisture regimes that are not extremely dry – may be meaningful to understanding coupling differences. While no major model difference is immediately visible in Fig. 3.5, I will uncover one statistically.

SP has little impact on the soil moisture distribution at all depths over SW US (Figure B4). This is corroborated by the similarities of percentiles between two models (Figure 3.6a), which are used as the bin structure to categorize the effects of SP on the distribution and mean of the Bowen ratio in multiple soil moisture groups (Figure 3.6b,c). SPCAM3.5 presents higher mean Bowen ratio in seven out of the ten bins and lower Bowen ratio in three very dry bins (soil moisture < 0.075 mm^3/mm^3). I hypothesize that the reason SP enhances thermal coupling over the SW US is that it produces conditions that barely change soil moisture distributions (Figure B4), but noticeably promote higher Bowen ratios within transitional soil moisture regimes (Figure 3.6d). This higher Bowen ratio at moderate soil moisture regimes in turn assists variations in soil moisture to translate into noticeable fluctuations in near-surface temperature, driving a stronger thermal coupling over the SW US. At least in regions where the first-order control of mean precipitation is absent, such effects could determine the magnitude of thermal coupling. It is natural to wonder about the reverse tendency for CAM to produce larger Bowen ratios in three very dry bins. While at first this might imply stronger dependency between soil moisture and near-surface temperature at these bins, I suspect it is overwhelmed by too little variation in soil moisture at such dry values (Table B1) to have meaningful impact on overall thermal coupling.

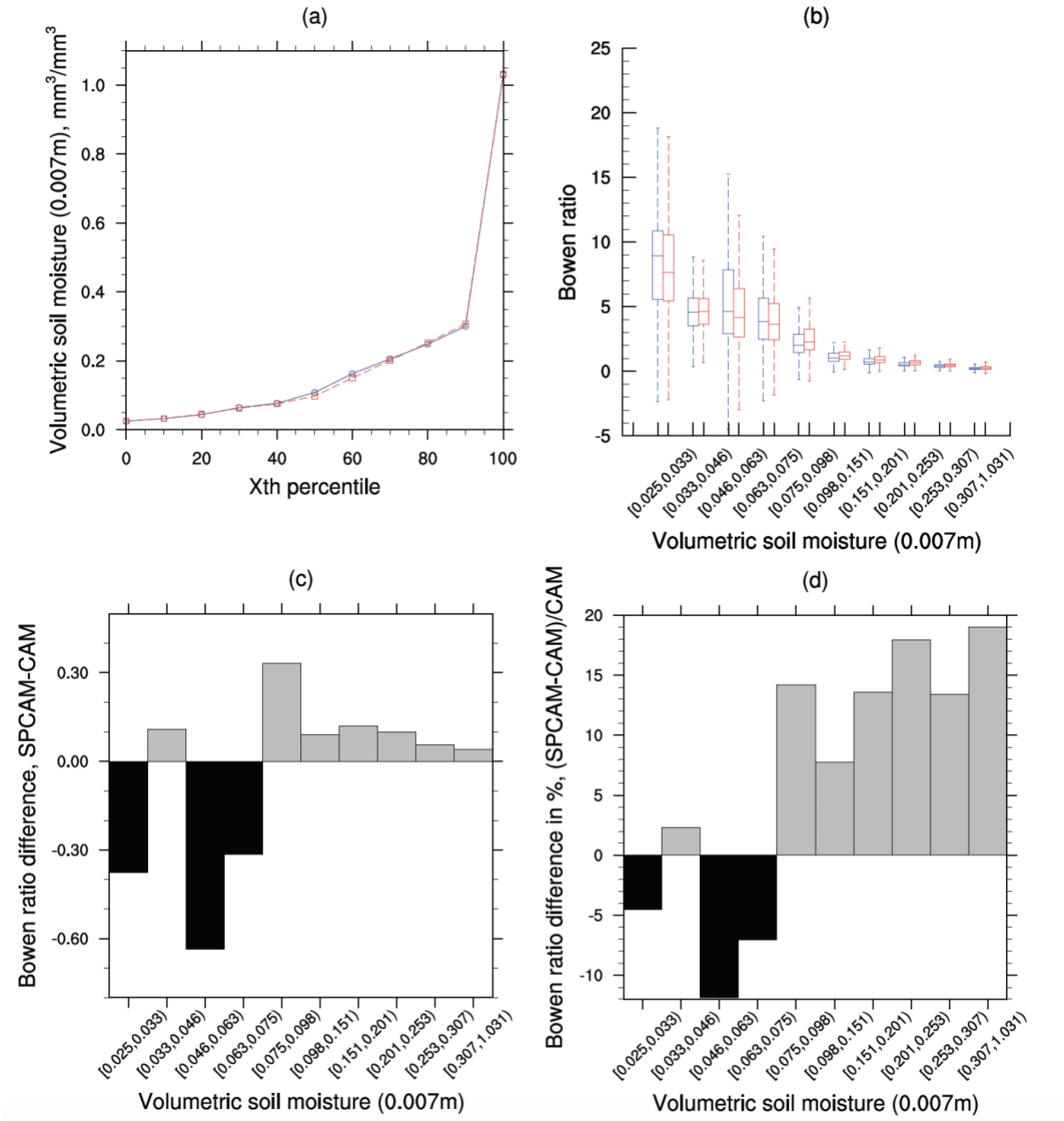

Figure 3.6 Based on daily samples in ENS(W), over the Southwestern US and Northern Mexico (as outlined in Figure 3) during boreal summer, (a) deciles of volumetric soil moisture in CAM3.5 (blue solid) and SPCAM3.5 (red dashed). (b) Box-and-whisker plot of the Bowen ratio binned within percentiles of volumetric soil moisture at 7 mm depth in CAM3.5 (blue) and SPCAM3.5 (red). Bowen ratio is only calculated when absolute value of latent heat flux is larger than 10 watts/m2. The whiskers delinate 1.5 times the interquartile range. (c) Difference of the mean Bowen ratio between SPCAM3.5 and CAM3.5 within each volumetric soil moisture decile bin. (d) Changes of Bowen ratio in SPCAM relative to CAM are expressed in percentage for each volumetric soil moisture decile bin. In the 1st-10th bin, Bowen ratio changes by -4.5%, 2.3%, -11.8%, -7.1%, 14.2%, 7.7%, 13.6%, 17.9%, 13.4%, 19.0%, respectively.

3.3.3 Magnified Bowen ratio and its climate sensitivity as a systematic effect of SP

The above analysis has suggested that a locally enhanced Bowen ratio might play a role in promoting an otherwise puzzling enhancement of thermal L–A coupling over the SW US. Effects of SP on the simulated Bowen ratio have not been reported previously, so the question naturally arises as to whether SP has any robust or systematic effect on surface energy flux partitioning beyond this region. If so, this would be worth knowing, since the Bowen ratio is fundamental to near-surface climate.

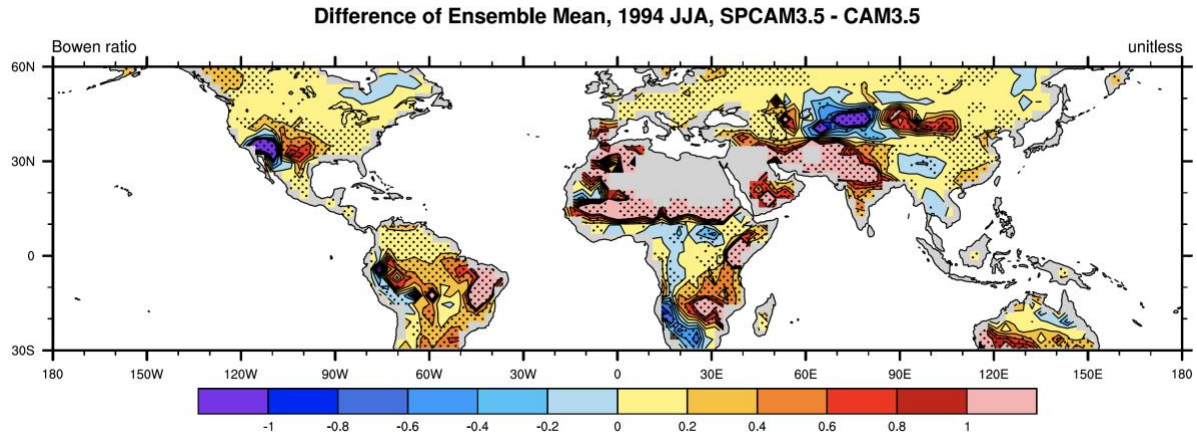

Figure 3.7 Based on ENS(W), Bowen ratio differences of the 16-member ensemble mean between SPCAM3.5 and CAM3.5. Bowen ratios are calculated only when absolute value of surface latent heat flux is larger than 10 watts/m2. Stippling is based on controlling False Discovery Rate (FDR) (Wilks 2016) by choosing $\alpha_{FDR} = 0.1$. Assuming synoptic temporal scale (weekly) Bowen ratio is nearly independent, original sample size is reduced by a factor of 7 to account for autocorrelation in the Student's t test.

Figure 3.7 globally examines the Bowen ratio differences between two models in the control simulation of the GLACE ensemble. This suggests that the effects of SP on Bowen ratio noted over the SW US are actually a global phenomenon. The higher Bowen ratio regime in SPCAM3.5 is present over the majority of the land and the difference of Bowen ratio between

two models is robustly and detectably positive over the vast majority of continental grid points, despite its geographic and inter-ensemble variability (Table 3.1).

Table 3.1 Statistics of the difference of ensemble mean Bowen ratio between SPCAM3.5 and CAM3.5 over land in ENS(W). (Latitude 30°S-60°N, only consider where |latent heat flux| > 10 watts/m2)

Mean	Standard deviation	Lower quartile	Median	Upper quartile	Mininum	Maximum	Range
0.31	0.53	0.04	0.13	0.35	-3.80	6.61	10.41

Do these changes in the surface flux climatology represent an improvement, or deterioration in model realism? Comparing 16-year time periods from our AMIP simulations against observationally derived FLUXNET-MTE datasets [*Jung et al.*, 2009, 2011] (Figure 3.8), within 50°-60°N, both surface sensible and latent heat fluxes are biased low in CAM3.5 (Figure 3.8a,c), while the magnitude of this negative bias is reduced in SPCAM3.5 (Figure 3.8b,d). More broadly from 30°S to 60°N over land, SPCAM3.5 outperforms CAM3.5 in the representation of surface sensible heat flux, latent heat flux and Bowen ratio based on mean biases and Root-Mean-Square Error (RMSE) (Numbers above each sub-panel in Figure 3.8). SP reduces global biases of Bowen ratio from -0.43 to -0.14, and produces smaller RMSE (1.05 < 1.40). From this perspective, the augmentation of Bowen ratio over land by SP is a clear improvement. Nonetheless, regional biases exist. Both models slightly underestimate the Bowen ratio during boreal summer in mid-latitudes in the Northern Hemisphere (Figure 3.8e,f). Over India, CAM3.5 presents moderately negative anomalies of Bowen ratio. In contrast, SPCAM3.5 exhibits large positive anomalies associated with very large (small) sensible (latent) heat flux. Over South America, positive Bowen ratio biases are noticeably larger in CAM3.5 than in SPCAM3.5,

resulting from exceedingly large positive (negative) biases of sensible (latent) heat flux. In SPCAM3.5, representations of Bowen ratio are better over South America but worse over India. Over the SW US, Bowen ratio is biased low throughout in CAM3.5 while mixed with moderate negative and positive anomalies in SPCAM3.5.

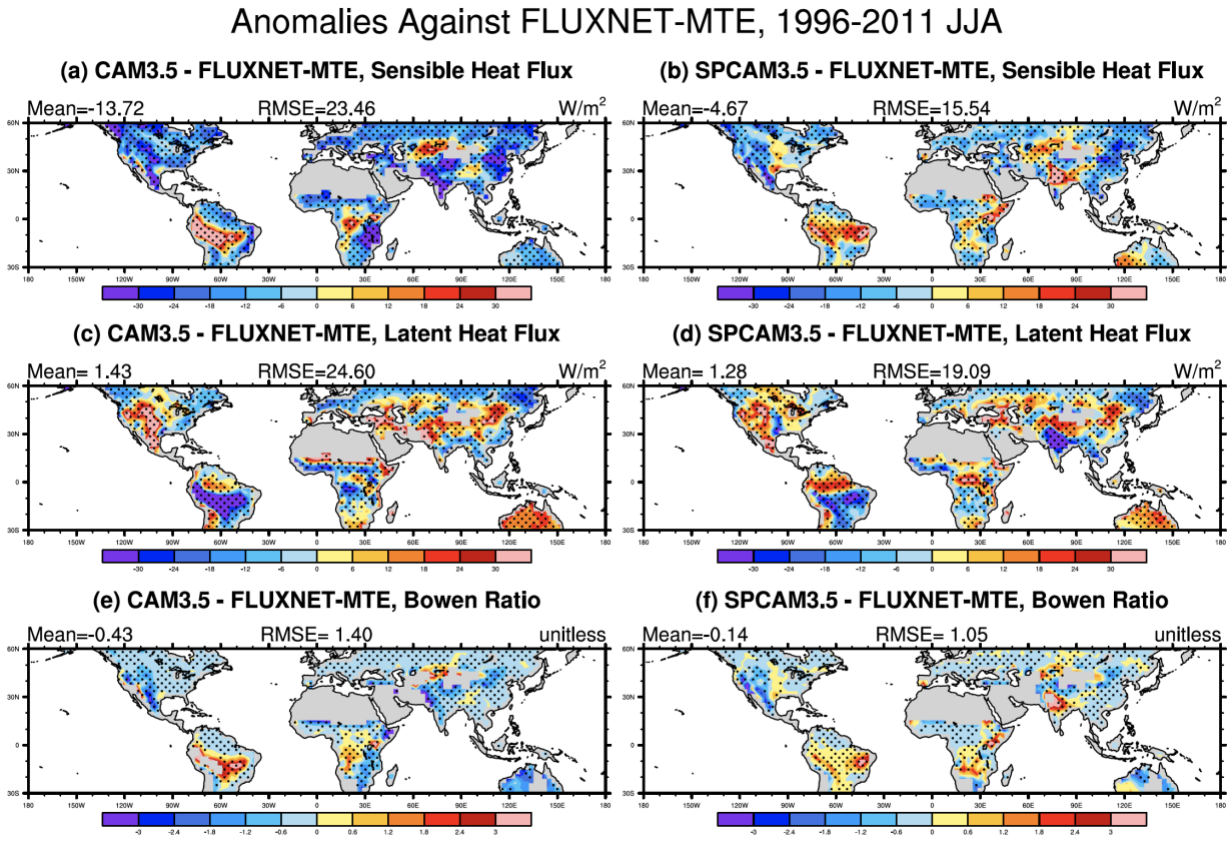

Figure 3.8 The difference maps of multiple variables between AMIP-type simulations and FLUXNET-MTE datasets, boreal summer mean during 1996-2011. (a) Differences of sensible heat flux between CAM3.5 and FLUXNET-MTE; (b) differences of sensible heat flux between SPCAM3.5 and FLUXNET-MTE; (c,d) same as (a,b) but for latent heat flux; (e,f) same as (a,b) but for Bowen ratio, Bowen ratio is calculated when absolute value of latent heat flux is greater than 10 W/m2. Stippling is based on controlling False Discovery Rate (FDR) (Wilks 2016) by choosing $\alpha_{FDR} = 0.1$. Numbers in the upper left corner are latitude-weighted near global (30°S - 60°N) mean biases, numbers in the upper center are latitude-weighted RMSE.

To further test the robustness of the seemingly systematic effects of SP on the Bowen ratio over land, several independent simulations with modern versions of SPCAM were investigated. In the

analysis below, the first (2006 to 2015) and last (2091 to 2100) ten-years of the CCSM4 RCP8.5 simulations were examined, and five-year samples of pre-industrial and 4xCO_2 conditions from the CESM1 simulations were evaluated. The analysis focuses on annual mean conditions over land excluding glacier regions, but including seasons and regions with temporary snow and ice cover.

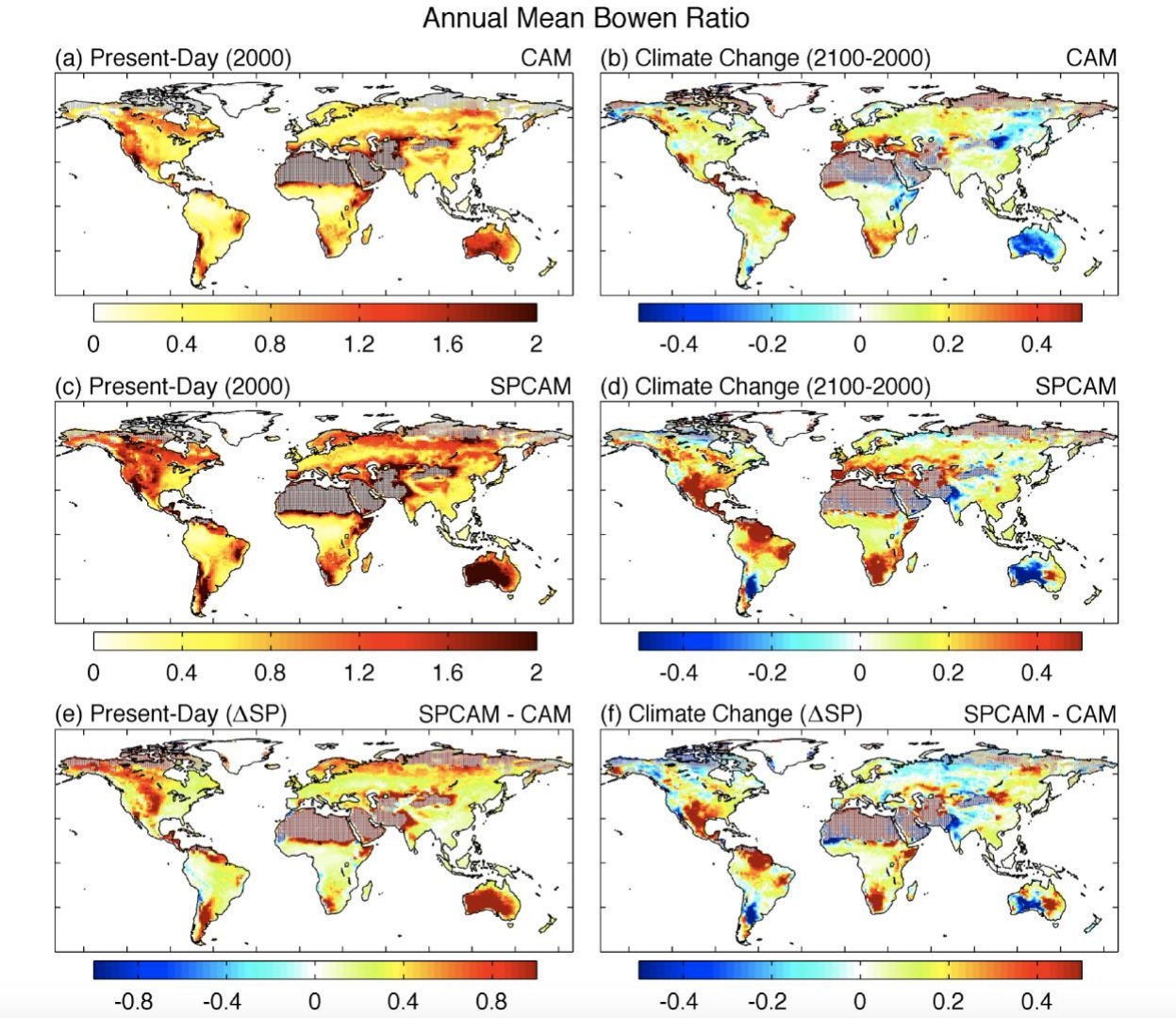

Figure 3.9 Annual mean Bowen ratio (fraction) over land simulated in CCSM4 from (a,b) CAM, (c,d) SPCAM, and (e,f) the difference (SPCAM minus CAM) for (a,c,e) present-day and (b,d,f) climate change conditions; the grey stippling regions have latent heat flux less than 10 Wm^{-2}.

Table 3.2 Annual-mean global-land-mean net radiation (W/m^2), sensible heat flux (W/m^2), latent heat flux (W/m^2), and Bowen ratio (fraction) from CAM and SPCAM simulations with (a)

CCSM4-CAM4, (b) CESM1-CAM4, and (c) CESM1-CAM5. ΔSP is the difference between SPCAM and CAM, and climate change is the differences between future (RCP8.5/4xCO_2) and present/pre-industrial climates as defined in the text. The Bowen ratio is calculated from global-land mean sensible and latent heat fluxes, rather than spatially averaging grid-point level Bowen ratio, so regions with low latent heat (stippling in Figure 3.9) do not contribute disproportionally.

	Present/Pre-Industrial Climate			**RCP8.5/4xCO_2 Climate**			**Climate Change**	
	CAM	**SPCAM**	**ΔSP**	**CAM**	**SPCAM**	**ΔSP**	**CAM**	**SPCAM**
a) Community Climate System Model v4 with Community Atmosphere Model v4								
Net Radiation	86.3	83.6	-2.8	92.2	89.0	-3.2	5.9	5.5
Sensible Heat	33.4	39.6	6.2	38.1	45.8	7.7	4.7	6.2
Latent Heat	52.7	43.2	-9.6	53.9	42.4	-11.5	1.2	-0.8
Bowen Ratio	0.63	0.92	0.28	0.71	1.08	0.37	0.07	0.16
b) Community Earth System Model v1 with Community Atmosphere Model v4								
Net Radiation	83.9	85.4	1.5	90.5	92.0	1.5	6.6	6.5
Sensible Heat	31.7	38.8	7.1	37.4	45.7	8.2	5.8	6.9
Latent Heat	52.3	46.1	-6.2	53.2	45.8	-7.4	0.9	-0.3
Bowen Ratio	0.61	0.84	0.24	0.70	1.00	0.29	0.10	0.16
c) Community Earth System Model v1 with Community Atmosphere Model v5								
Net Radiation	82.0	83.6	1.6	87.1	87.3	0.3	5.1	3.7
Sensible Heat	31.5	35.4	3.9	36.2	40.5	4.3	4.7	5.1
Latent Heat	50.1	47.8	-2.3	50.4	46.3	-4.1	0.3	-1.5
Bowen Ratio	0.63	0.74	0.11	0.72	0.88	0.16	0.09	0.13

The amplified Bowen ratio seen over land due to SP is robust across all three model configurations and versions, and it results from higher sensible and lower latent heat fluxes in all models and scenarios relative to their conventional CAM counterparts (Table 3.2). Differences between SPCAM and CAM are positive everywhere in the present-day and highlight regions in the Central US and Northern Canada, Northern Europe, Equatorial Central and South America, Southern South America, and Australia (Figure 3.9a,c,e). In the future climate change scenarios, all model versions project an increase in the global mean Bowen ratio, but the increase is larger with SPCAM (Table 3.2). CAM consistently predicts a large increase in sensible heat flux and a small increase of latent heat flux, while SPCAM predicts even larger increase in sensible heat flux and a small decrease in latent heat flux (i.e. opposite response to CAM). Differences in the Bowen ratio climate change response between SPCAM and CAM are mostly positive, with the

exception of Southern South America, Western Australia, India, and high latitudes in Northern Hemisphere. The largest increases in SPCAM are seen in the sensitive SW US/Mexico region, as well as Central America, and Northern South America, Southern Africa, and Eastern Australia (Figure 3.9b,d,f).

Overall and consistently in multiple versions of SPCAM, the Bowen ratio is higher in the present/pre-industrial climate, and has a larger amplification in climate change scenarios than in CAM. Given the connection between the Bowen ratio, thermal L-A coupling and near-surface temperature discussed above, the amplified mean Bowen ratio under SP may have important consequences for temperature variability and extremes on subseasonal timescales.

3.4 Conclusion

I have analyzed the effects of explicit convection on global thermal L–A coupling by using SP, which revealed a systematic effect of SP on the Bowen ratio with implications for climate change projection.

Effects of explicit convection on soil moisture–surface temperature coupling are regionally limited but interesting. Reduced thermal coupling occurs over the Arabian Peninsula, but enhancements happen over the Southwestern US and Northern Mexico when SP is used. These regional features are robust in the sense that they are immune to the diagnostics chosen and types of simulations performed. Over the Arabian Peninsula, the process chain is straightforward – SP favorably reduces the time mean rainfall, pushing the soil moisture away from transitional regimes required for a strong coupling, resulting in a reduced regional thermal coupling strength

that is more realistic for the region. Interestingly, over the Southwestern US and Northern Mexico, regional enhancements of thermal coupling in SP cannot be explained by differences in characteristics of rainfall such as the mean or frequency, nor due to differences in soil moisture. I have speculated that a tendency for SP to nonetheless produce an elevated Bowen ratio at moderate soil moisture regimes in this region leads to stronger thermal coupling. This led me to uncover that Bowen ratio amplification is a surprisingly systematic effect of SP, detectable over most continental regions and in four version pairs of CAM and SPCAM. Compared to FLUXNET-MTE constraints, the Bowen ratio amplification in the SPCAM3.5 simulations can be viewed as an improvement.

There is an associated systematic effect of SP on future climate change scenarios. Like many GCMs, CAM projects an enhanced Bowen Ratio by the end of this century, i.e. a significantly increased sensible heat flux and moderately increased latent heat flux. But SPCAM projects an even more pronounced increase of sensible heat flux, and slightly reduced latent heat flux. Thus in future climate, the augmentation of the Bowen ratio in SPCAM is considerably more extreme than in CAM. Such amplified climate sensitivity of Bowen ratio under SP might imply a more sensitive near-surface climate, especially regarding temperature variability and extremes. However, the recent findings by *Zhou and Khairoutdinov* [2017] of a muted temperature subdaily extreme response to climate change under SP suggest this effect may at least in some cases become dominated by other consequences of SP impacting the land surface, such as on regional time-mean soil moisture and cloud cover.

The climate sensitivity of the Bowen Ratio is amplified under SP. These sensitivities appear robust across model versions and experiment designs, and thus appear to be general effects of SP constituting useful context when interpreting surface climate predictions from Multiscale Modeling Frameworks. It would be worth further exploring the effects of SP within modern experiment designs that isolate the impact of L–A coupling in long climate change simulations, for instance as outlined in [*Seneviratne et al.*, 2013].

I acknowledge that an important limitation of this chapter is that a satisfying reason for why SP exhibits such a robust Bowen ratio amplification over land has not been identified. While beyond the scope of the current work, I view it as a priority for future work. One hypothesis is that it arises from enhanced surface air thermal ventilation due to amplification in the contrast between lowest atmospheric temperature and surface temperature in SPCAM. However, pilot tests disproved this hypothesis. Other hypotheses and associated sensitivity testing are needed to better understand this mysterious emergent behavior of explicit embedded convection. Additionally, I rely on the GLACE-type simulation to quantify the L–A coupling strength. Recently, Hauser et al. (2017) pointed out that besides decoupled L–A interactions, the water-balance perturbation in the land model introduced by soil moisture prescription may also contribute to non-negligible changes in temperature. Such effects imply that the derived coupling strength by GLACE may be unpurified due to the induced water-balance perturbation accompanied with the soil moisture prescription.

Chapter 4. Understanding the Remote Influence of Andean Convection on Amazonian Rainfall

This chapter is based on a manuscript in preparation as:

Qin, H., Pritchard, M. S., Terai, C., Bacmeister, J., & Bogenschutz, P., Understanding the Remote Influence of Andean Convection on Amazonian Rainfall. (*In preparation*)

Abstract

Historical simulations of General Circulation Models (GCMs) from the Coupled Model Intercomparison Project Phase 5 (CMIP5) produce too much precipitation over the Andes but too little over the Amazon, hindering the credibility of future projections on the South America Monsoon System (SAMS) and terrestrial biosphere. I investigate the remote role of latent heating by Andean convection in the rainforest dry bias. Using the Community Earth System Model version 1 (CESM v1) and focusing on the wet season, an ensemble of mechanism denial experiments show that Andean convective heating reduces rainfall over the Amazon with a maximum of -1 mm/day. Details of the fast adjustment to this forcing help unveil the main causality. The timescale of initial Amazonian precipitation response is 5-10 hours consistent with fast gravity wave transmission of vertical velocity signals that force changes in the column moisture budget. Associated drying of the Amazon boundary layer is then linked to secondary feedbacks by reducing the Convective Available Potential Energy (CAPE) over the Amazon. Column moisture budget analysis shows that the total advection of moisture over the Amazon due to Andean convective forcing is controlled by the vertical advective term that can be traced back to a mountain-forced component of the vertical velocity field. This study is illustrative for other modelers to quantify the Amazonian rainfall biases of Andean origin in their own GCM of interest, which is helpful in forming their model development strategies.

4.1 Introduction

As the largest terrestrial carbon reservoir, the Amazon rainforest is critical to the climate system. To understand its future, especially as the community approaches an era of explicitly simulated vegetation, it is crucial for modern Earth System Models (ESMs) to accurately capture the physical processes that sculpt the regional water cycle. A realistic representation of Amazonian hydroclimate is also instrumental to climate non-locally, as Amazonian rainfall significantly modulates the hydrologic cycle and energy balance globally (Avissar and Werth 2005; Lawrence and Vandecar 2015; Medvigy et al. 2013; Snyder 2010; Werth and Avissar 2002). However, the current understanding of the processes that control Amazonian rainfall in present and future climate remains incomplete.

One symptom of this incomplete understanding is a chronic ESM bias; modern climate models do not simulate time mean rainfall realistically over tropical South America. Specifically, the multi-model annual mean rainfall from the Coupled Model Intercomparison Project Phase 5 (CMIP5) suffers from what I will refer to as a "Wet Andes, Dry Amazon (WADA)" bias (IPCC 2014; Mehran et al. 2014), which is associated with too much surface net radiation, overly high Bowen ratio, and associated dry lower troposphere (Lintner et al. 2017) over the rainforest, as well as excessive rainfall along the Intertropical Convergence Zone (ITCZ) in adjacent oceans. Although Sea Surface Temperatures (SSTs) are known to play an important role in modulating Amazonian hydroclimate (Chen et al. 2018; Fernandes et al. 2015; Yin et al. 2012), the existence of the WADA bias (Fig 4.1c) even in CMIP5 simulations (Table 4.1) following the Atmospheric Model Intercomparison Project (AMIP) protocol that prescribe observed SSTs (Fig 4.1a) suggests its non-oceanic sources of bias.

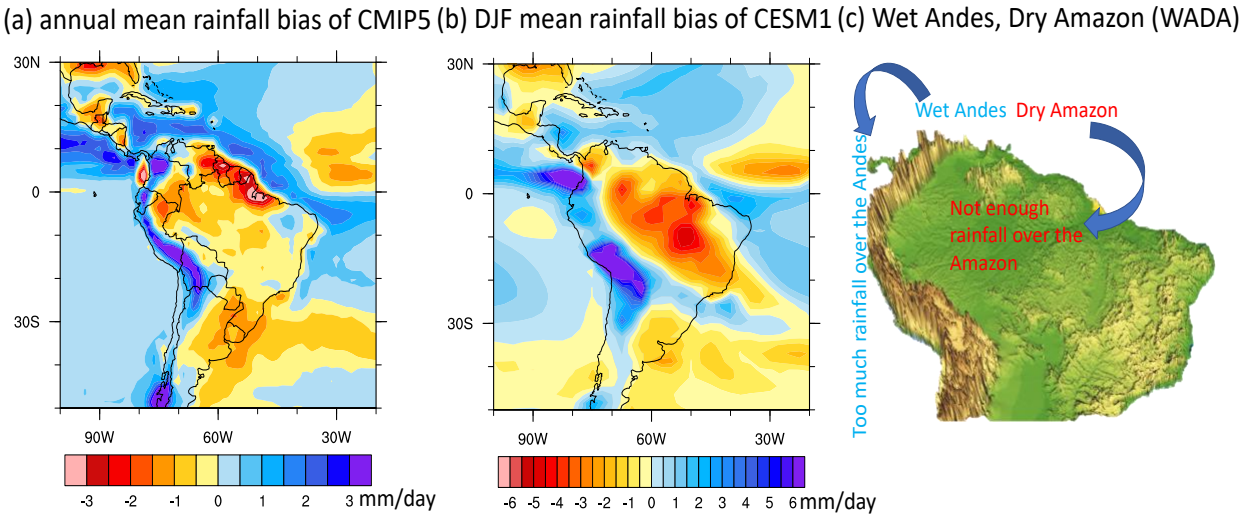

Figure 4.1 (a) Annual mean rainfall biases of the multi-model-mean of 22 AMIP r1i1p1 simulations in the CMIP5 archive (see Table 4.1) re-gridded to 0.9°x1.25° grid relative to the Global Precipitation Climatology Project (GPCP) v2.3 (Adler et al. 2003; Huffman et al. 2009), 1982-2008 a. Units: mm/day; (b) In a companion 1989-2008 AMIP-type simulation, the Dec-Jan-Feb mean rainfall bias in the CESM v1.1 in CESM's 1.9°x2.5° grid. Units: mm/day. (c) Illustration of the Wet Andes, Dry Amazon (WADA) concept which describes a model simulating too much rainfall over the Andes but not enough rainfall over the Amazon.

Table 4.1 AMIP-type simulations from the 22 CMIP5 models used in Figure 4.1a and Figure C1 in our study.

Model	Institute	Country	Reference
CCSM4	National Center for Atmospheric Research	USA	Gent et al. (2011)
CanAM4	Canadian Centre for Climate Modelling and Analysis	Canada	von Salzen et al. (2013)
ACCESS1-3	Commonwealth Scientific and Industrial Research Organization	Australia	Bi et al. (2013); Dix et al. (2013)
ACCESS1-0			
CSIRO-Mk3-6-0	Australian Commonwealth Scientific and Industrial Research Organization Marine and Atmospheric Research, Queensland Climate Change Centre of Excellence	Australia	Rotstayn et al. (2010)
NorESM1-M	Norwegian Climate Centre	Norway	Bentsen et al. (2013)

CMCC-CM	The Centro Euro-Mediterraneo sui Cambiamenti Climatici	Italy	Scoccimarro et al. (2011)
MPI-ESM-MR	Max Planck Institute for Meteorology	Germany	Raddatz et al. (2007)
MPI-ESM-LR			
IPSL-CM5A-MR	Institut Pierre Simon Laplace	France	Marti et al. (2010); Dufresne et al. (2013)
IPSL-CM5B-LR			
IPSL-CM5A-LR			
CNRM-CM5	Centre National de Recherches Meteorologiques, Meteo-France and Centre Europeen de Recherches et de Formation Avancee en Calcul Scientifique	France	Voldoire et al. (2013)
MRI-AGCM3-2H	Meteorological Research Institute	Japan	Mizuta et al. (2012); Yukimoto et al. (2012)
MRI-CGCM3			
MIROC5	Atmosphere and Ocean Research Institute, The University of Tokyo, National Institute for Environmental Studies, Japan Agency for Marine-Earth Science and Technology	Japan	Watanabe et al. (2010); Watanabe et al. (2011)
MIROC-ESM			
HadGEM2-A	Met Office Hadley Centre	UK	Martin et al. (2006); Ringer et al. (2006)
GFDL-CM3	National Oceanic and Atmospheric Administration, Geophysical Fluid Dynamics Laboratory	USA	Donner et al. (2011)
GFDL-HIRAM-C360			Lin (2004); Putman and Lin (2007); Zhao et al. (2009)
GFDL-HIRAM-C180			
inmcm4	Institute for Numerical Mathematics	Russia	Volodin et al. (2010)

Terrestrial feedbacks have been implicated in sustaining and amplifying the WADA bias but limitations of modern land surface models are not obviously its sole, or root cause. Yin et al. (2012) speculated that overly strong evapotranspiration (ET) during the wet season due to excess

surface net radiation might cause excess soil moisture loss, which could subsequently cause scarcity of ET and rainfall in the following dry season. In the Community Earth System Model (CESM) lineage, Zhang et al. (2017) argued that unlike during the wet season, dry season rainfall dry biases over southern Amazon is largely driven from the land component. Regarding the wet season rainfall deficit over southwestern Amazon in CESM v1, Sakaguchi et al. (2018) shows that despite improvements in surface turbulent fluxes, the rainfall biases are not relieved by replacing Community Land Model version 4 (CLM4) with CLM4.5, suggesting that the biases might be common, or external, to both versions of the land model.

From the atmospheric perspective, it is known that aspects of the rainforest dry biases are sensitive to cloud treatments in the model. Sakaguchi et al. (2018) showed that wet season rainfall dry biases over southwestern Amazon are very sensitive to the Convective Available Potential Energy (CAPE) calculation in the deep convection scheme. Using the Weather Research and Forecasting (WRF) model with parameterized large-scale circulation, the morning fog layer in the wet season and associated cloud albedo feedbacks are captured, which contribute to better representations of the diurnal and seasonal cycles of surface fluxes and precipitation over the Amazon (Anber et al. 2015). Using 2D Cloud-Resolving-Models embedded in traditional General Circulation Models (GCMs), cloud super-parameterization (SP) is shown to generally improve the soil moisture – ET relationship and surface turbulent fluxes (Qin et al. 2018; Sun and Pritchard 2016); in certain configurations SP has also been coerced to somewhat reduce the wet season rainfall dry bias over southern Amazon with a higher-order turbulence closure scheme (Zhang et al. 2017). However, details of the causality, which can be complex and non-local, are difficult to clarify.

There is a rich tradition in viewing the causality that associates Amazonian with Andean rainfall from east to west, i.e., with the mean flow and moisture transport. This is logical given that the South American Low-Level Jet (SALLJ) is a main moisture source contributing to Amazon precipitation. For instance, it is likely not a coincidence that a regional rainfall maximum occurs at the Peruvian Andes–Amazon transition coincident with the height of the strongest SALLJ (Chavez and Takahashi 2017). Interesting positive feedbacks accompany this east-to-west moisture transport. Meanwhile, latent heat release from precipitation over the Amazon helps strengthen the atmospheric heating gradient between the Amazon and the tropical Atlantic Ocean, which can further enhance the moisture inflow (Boers et al. 2017; Kooperman et al. 2018). The argument of using SALLJ moisture transport to understand Andean and Amazonian rainfall is also evident in studies focusing on climate of the past and future. During the Last Glacial Maximum, a strengthening of the Amazon-to-Andes moisture transport was linked to rainfall enhancement over the Peruvian and Bolivian Andes and large-scale drying over the Amazon (Vizy and Cook 2007). With elevated CO_2 levels in future climate, the physiological response of Amazon rainforests drives a similar WADA response of rainfall (Kooperman et al. 2018) related to transport of moisture and Moist Static Energy (MSE) by the SALLJ (Langenbrunner et al. 2019).

Our working hypothesis is that an unknown portion of the causality connecting the Andes and Amazon water cycle may flow in the *reverse* direction, i.e., from west-to-east against the mean flow. This is consistent with close links between Andean orography, SALLJ formation, and Amazon rainfall that are well established (Insel et al. 2010; Rasmussen and Houze 2016) in regional modeling experiments, including those of Langenbrunner et al. (2019) which revealed a

significant fraction of a forest-induced drying lags its interaction with downstream topography through non-local controls. The purpose of this article is to answer the question: can the WADA bias phenomenon (Fig 4.1c) be excited solely from the Andean side (rather than the Amazonian side), and if so, what are the most efficient remote-control mechanisms, and what fraction of CESM's dry-Amazon bias can be explained from its wet-Andes component?

By testing this hypothesis, I aim to better understand the role of orographic Andean convection on rainfall over tropical South America, and help better set priorities for where to focus model development efforts towards reducing Amazon dry biases. Unlike CMIP5 studies (Li et al. 2018; Lintner et al. 2017; Mueller and Seneviratne 2014; Yin et al. 2012), which rely heavily on diagnostic measures, I will use a global model to conduct causatively unambiguous sensitivity experiments in an ensemble simulation approach that allows satisfying statistical detection and attribution of the effects of Andean convection on Amazonian rainfall.

The analysis is structured as follows. Section 4.2 will briefly describe our methods and data, including mechanism denial experiment design, and analysis methods. In Section 4.3, I first show the characteristics of Andean convection, then elaborate on the spatial-temporal features of Amazonian precipitation responses due to Andean convective forcing, as well as multiple perspectives to understand the underlying mechanisms. In Section 4.4, I depict the Andean forced eastward expansion features over the Amazon. Discussions and conclusions are summarized in Section 4.5.

4.2 Data and methods

4.2.1 Experiment design

To investigate the role of Andean convection on Amazonian rainfall, I conduct two groups of simulations using CESM v1.1, described below. All simulations use the finite volume dynamical core at 1.9°x2.5° (f19_g16) horizontal resolution and 30 vertical levels, driven with prescribed SSTs (i.e., AMIP-style simulations) and using the "CAM5" physics parameterization suite. That is, the deep convection parameterization follows Zhang and Mcfarlane (1995) with modifications from Richter and Rasch (2008) and Raymond and Blyth (1986, 1992); the shallow convection scheme uses the University of Washington shallow convection scheme following Park and Bretherton (2009); cloud microphysics based on Morrison and Gettelman (2008) with updates from Gettelman et al. (2010) and cloud macrophysics are from Park et al. (2014); radiative transfer calculations are given by the Rapid Radiative Transfer Method for GCMs i.e. RRTMG (Iacono et al. 2008; Mlawer et al. 1997). Aerosol concentration data is prescribed with cyclic values of the year 2000.

(1) CTR group: A prescribed-SST simulation of Austral summer (Dec-Jan-Feb; DJF) of the year 1989, starting on Nov 21st with the first ten days discarded as spin-up.

(2) TOPO group: A sensitivity test ensemble, in which I artificially shut down the temperature tendency from parameterized deep, shallow convection, cloud microphysics, and cloud macrophysics over major mountain and plateau areas (methods described below). Each TOPO simulation lasts four days with hourly output frequency and is branched off from the CTR simulation at 10-day increments starting from Dec 1st midnight UTC.

The result is a 9-member ensemble of paired 4-day hindcasts – the unsteady drift between the ensemble means of CTR and TOPO will isolate the effects of Andean convection with statistical clarity and clues into causation, including lead-lag relationships.

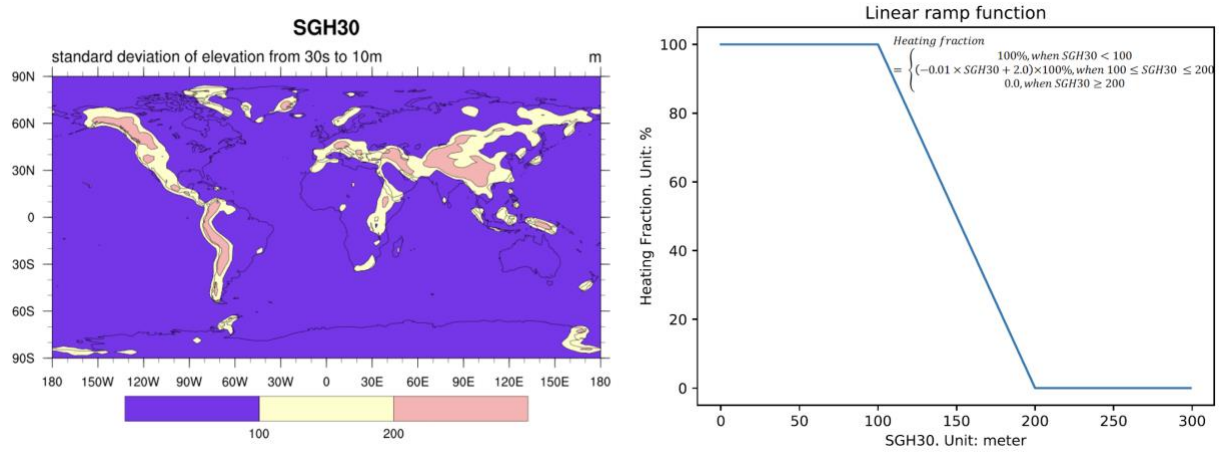

Figure 4.2 Illustration of the interference in the TOPO group simulations. (a) Values of a proxy of topography–SGH30, which represents the standard deviation of elevation from 30arcses to 10arcmin. At the time-step level, temperature tendencies from deep convection, shallow convection, cloud microphysics, and cloud macrophysics are untouched if $SGH30 < 100m$ (purple color), linearly damped if $100m \leq SGH30 < 200m$ (beige color), and fully muted if $SGH30 \geq 200m$ (pink color). Units: meter. (b) The linear ramp function.

The mechanism denial in the TOPO group is restricted geographically to regions of high elevation based on a proxy of topography using a linear ramp function (Figure 4.2). For convenience, this is built around an existing model diagnostic of subgrid orographic variability, the standard deviation of elevation from 30arcsec to 10arcmin, which associates with major mountain chains (Figure 4.2). At each model time step, I apply the ramp function to artificially modulate the magnitude of the diabatic temperature tendency calculated by the net effects of the deep, shallow convection schemes, the cloud macrophysics, and microphysics packages. Full heating (no denial) is allowed at low elevations ($SGH30 < 100m$). I linearly decrease the magnitude of the actual diabatic temperature tendency in proportion to local topography when approaching higher elevations ($100m \leq SGH30 < 200m$), until reaching complete denial of parameterized temperature tendency where $SGH30 \geq 200m$.

The reasons for conducting only wet season (DJF) simulations are twofold. First of all, Andean annual rainfall mostly comes from its wet-season contribution based on satellite observations (Chavez and Takahashi 2017). Therefore, the effects of Andean convection on Amazonian rainfall during the wet season should be easier to detect than during other seasons. Secondly, it is during the wet season that CAM5, the atmospheric component of CESM, is known to produce the strongest rainfall deficit over southern Amazon (Zhang et al. 2017). Similar to other CMIP5 models, the CESM v1.1 used in our experiments has a similar WADA bias pattern during the wet season (Fig 4.1b).

4.2.2 Analysis methods for investigating controls on Amazonian precipitation

There are multiple ways to think about what controls time-mean regional rainfall anomalies in the tropics, and their sensitivities, such that it is important to consider multiple viewpoints to gain a holistic sense of potential causality in our experiments.

4.2.2.1 Moist static energ

Moist Static Energy (MSE) is defined as follows:

$$MSE = C_p T + L_v q + gz \tag{4.1}$$

where C_p is the specific heat of air at constant pressure, T is absolute temperature, L_v is the latent heat of vaporization, q is specific humidity, g is gravitational acceleration, and z is height above some reference level. MSE incorporates the Latent Static Energy (LSE) $L_v q$ and Dry Static Energy (DSE) $C_p T + gz$.

In the tropics, the MSE profile is usually a "V" shape with a minimum in the mid-troposphere and deep convection imports MSE at low-level with associative convergence and exports MSE aloft associative with divergence. As a result, near-surface MSE increase is an indicator of strong convection and precipitation.

4.2.2.2 Mechanics of the gross moist stability

One helpful viewpoint to understand tropical precipitation is the gross moisture stability, briefly reviewed here. Raymond et al. (2009) pointed out that for an air column, at steady state, the joint conservation of specific moist entropy *s* and total cloud water mixing ratio *r* yields

$$P - E = \frac{T_R(F_s - R)}{L\Gamma_R} \qquad (\propto \frac{F_s - R}{\Gamma_R}) \tag{4.2}$$

where T_R=300K, L is the latent heat of condensation, P represents precipitation rate, E stands for surface evaporation rate, F_s is the diabatic MSE input from surface heat and moisture fluxes, R is the column radiative cooling, and Γ_R is a dimensionless quantity called Normalized Gross Moist Stability (NGMS),

$$\Gamma_R = -\frac{T_R\langle\nabla\cdot(sv)\rangle}{L\langle\nabla\cdot(rv)\rangle} \tag{4.3}$$

where the $\langle * \rangle$ denotes mass-weighted vertical integration, and v stands for the horizontal wind. NGMS can be further decomposed into horizontal,

$$\Gamma_H = -\frac{T_R\langle v\cdot\nabla s\rangle}{L\langle\nabla\cdot(rv)\rangle} \tag{4.4}$$

and vertical components,

$$\Gamma_V = -\frac{T_R\langle\omega(\partial s/\partial p)\rangle}{L\langle\nabla\cdot(rv)\rangle} \tag{4.5}$$

where ω is the vertical velocity on pressure coordinate.

Based on equation (4.2), it is clear that since T_R and L are constants, the net water input ($P - E$) in an air column is determined by the ratio of the diabatic term $(F_s - R)$ over the NGMS term.

The quantity of NGMS can be expressed alternately as in Inoue and Back (2015),

$$NGMS = \frac{\langle v \cdot \nabla h \rangle + \langle \omega \frac{\partial h}{\partial p} \rangle}{\langle v \cdot \nabla s \rangle + \langle \omega \frac{\partial s}{\partial p} \rangle} \tag{4.6}$$

where h and s represent MSE and DSE, respectively. The NGMS can be interpreted as the efficiency of MSE export by convection and its associated large-scale circulations per unit intensity of convection. An obvious limitation of equation (4.2) is that it is obtained under the assumption of steady state, which may not be a fair test of what I will show are rapidly evolving and diurnally fluctuating model sensitivities. Nonetheless, it is important to look at a gross moist stability framework as part of a holistic analysis of possible controls on Amazon precipitation.

4.2.2.3 Convective Available Potential Energy

Convective Available Potential Energy (CAPE) is defined as follows:

$$CAPE = \int_{p_f}^{p_n} R_d (T_{UP} - T_{UE})\, dlnp \tag{4.7}$$

where p_n and p_f is the pressure at the level of neutral buoyancy and level of free convection respectively. R_d is the specific gas constant for dry air. T_{UP} is the virtual temperature of an air parcel moving from the level of free convection to the level of neutral buoyancy. T_{UE} is the virtual temperature of the environment.

On a skew-T log-p diagram, CAPE is the positive area of a region between the observed sounding curve and the parcel lifting curve. Larger CAPE values are beneficial to stronger updrafts and deep convection.

4.2.2.4 Moisture budget

A complementary and traditional way to view precipitation causation is through the moisture budget alone, by considering the controls on sources of vapor to the region, and their lead-lag relationship relative to our forcing, as seen in many other studies (Seager and Henderson 2013; Veiga et al. 2005; Yang et al. 2014).

Measuring total moisture advection accurately

To avoid issues when estimating advection offline through imperfect reconstruction of horizontal and vertical gradients and complex corrections needed to account for a terrain-following hybrid vertical coordinate (Benedict et al. 2014), I instead infer the effects of advection using the residual method. That is, first the local total rate of change in specific humidity is calculated as

$$Q_t = \frac{QAP(t) - QAP(t-1)}{\delta t} \tag{4.8}$$

where *QAP* is the specific humidity after calculations of physics packages, δt is the time interval between two timestamps *t* and *t-1*.

The total advection of specific humidity can then be obtained by

$$Q_{adv} = Q_t - PTEQ \tag{4.9}$$

where *PTEQ* is the total diabatic tendency of specific humidity accumulated over the model physics package during the corresponding time interval.

Estimating the subcomponents of total advection

Since moisture advection will turn out to be an especially important aspect of our attribution argument it is important to attempt to decompose it into its components, which can be

imperfectly estimated using finite difference gradient estimation. That is, the total advection of specific humidity can be written as

$$-u\frac{\partial q}{\partial x} - v\frac{\partial q}{\partial y} - \omega\frac{\partial q}{\partial p} \tag{4.10}$$

such that, combined with the continuity equation,

$$\frac{\partial u}{\partial x} + \frac{\partial v}{\partial y} + \frac{\partial \omega}{\partial p} = 0 \tag{4.11}$$

the total advection of specific humidity can be written as

$$-u\frac{\partial q}{\partial x} - v\frac{\partial q}{\partial y} - \omega\frac{\partial q}{\partial p} - q(\frac{\partial u}{\partial x} + \frac{\partial v}{\partial y} + \frac{\partial \omega}{\partial p})$$

or

$$-\left(u\frac{\partial q}{\partial x} + v\frac{\partial q}{\partial y}\right) - \omega\frac{\partial q}{\partial p} - q\left(\frac{\partial u}{\partial x} + \frac{\partial v}{\partial y}\right) - q\frac{\partial \omega}{\partial p} \tag{4.12}$$

Our analysis will focus on vertical integrals, wherein the horizontal gradients are estimated following vertical interpolation from the model's native hybrid terrain-following coordinate to a fixed high-resolution vertical pressure grid.

Decomposing vertical moisture advection

Finally, since the vertical component of vertical moisture advection will prove of main interest, disentangling the roles of circulation from moisture redistribution effects will become important. To this end, the difference of the vertical advection of specific humidity between the CTR and TOPO groups can be written as

$$\langle -\omega\frac{\partial q}{\partial p}\rangle_{CTR} - \langle -\omega\frac{\partial q}{\partial p}\rangle_{TOPO}$$

or

$$\langle -\omega\frac{\partial q}{\partial p}\rangle_{CTR-TOPO} \tag{4.13}$$

where the brackets again represent mass-weighted vertical integration. To understand whether the velocity vs. moisture fields provide the dominant effect, this term can be further decomposed into three terms as follows

$$\langle -\omega \frac{\partial q}{\partial p} \rangle_{CTR-TOPO} = -\langle \omega_{TOPO} \left[\frac{\partial q}{\partial p}\right]_{CTR-TOPO} \rangle - \langle \omega_{CTR-TOPO} \left[\frac{\partial q}{\partial p}\right]_{TOPO} \rangle - \langle \omega_{CTR-TOPO} \left[\frac{\partial q}{\partial p}\right]_{CTR-TOPO} \rangle \quad (4.14)$$

4.2.3 Other datasets

In addition to the model output from our sensitivity experiments, I also use estimates of observed rainfall from the Global Precipitation Climatology Project (GPCP) version 2.3 (Adler et al. 2003; Huffman et al. 2009), the remotely retrieved tropospheric humidity from the Atmospheric Infrared Sounder (AIRS) version 2 (Tian et al. 2013) datasets, the tropospheric vertical velocity and humidity fields from the ERA5 Reanalysis (Hans et al. 2019), and outputs from 22 models (Table 4.1) in the CMIP5 AMIP historical simulations (Taylor et al. 2012b) for auxiliary analysis.

4.3 Responses of Amazonian rainfall to Andean convection

In this section, I first present baseline characteristics of Andean convection in CESM v1.1, then demonstrate the effects of Andean convective forcing on non-local Amazon rainfall and finally test multiple hypotheses in an attempt to understand the relevant processes and mechanisms.

4.3.1 Characteristics of Andean forcing

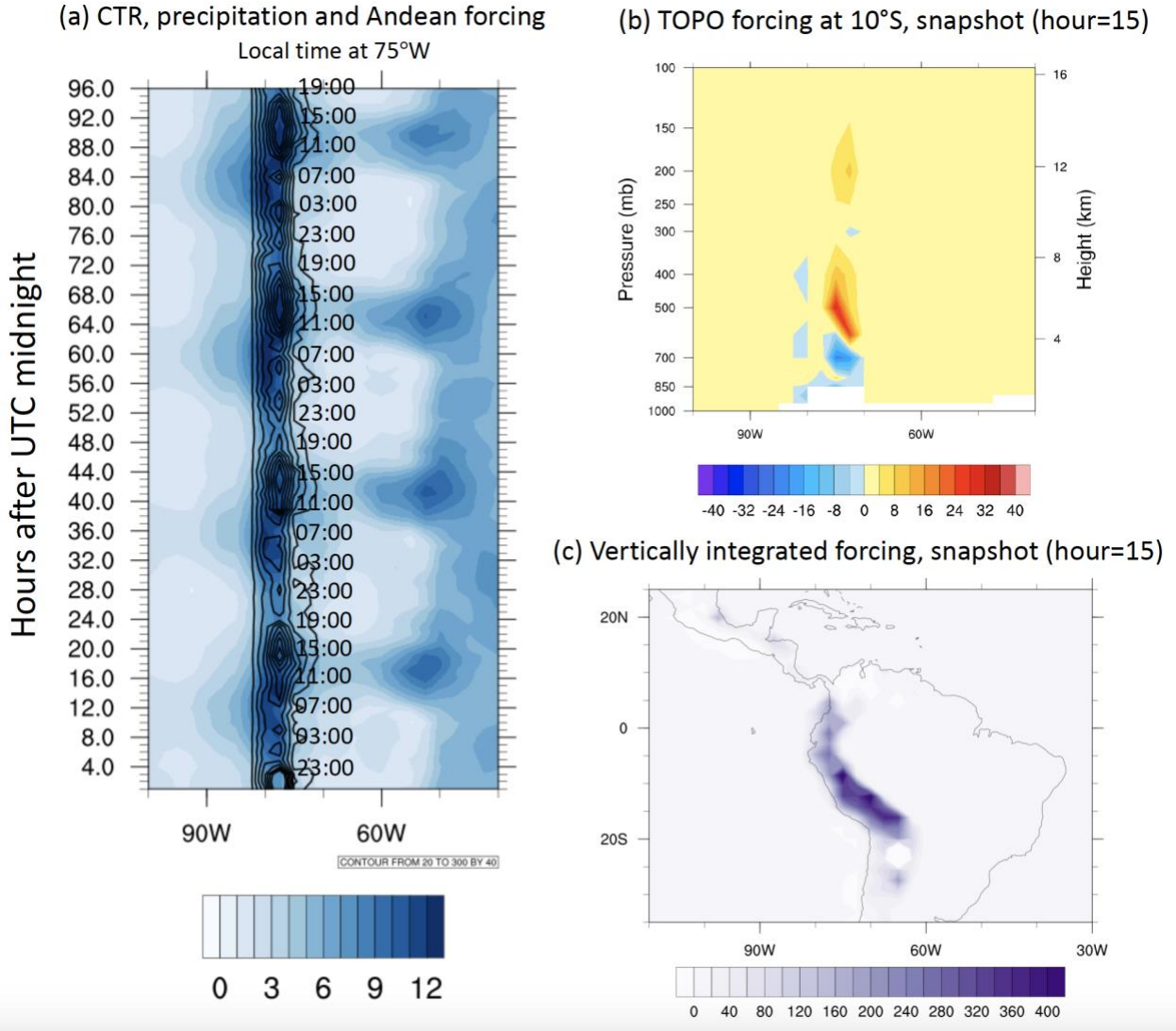

Figure 4.3 (a) Hovmöller diagram showing the composite diurnal cycle of equatorial rainfall (shading) in the CTR ensemble (nine members), averaged between 5°S-5°N, with contours showing the vertically integrated (1000-100hPa) Andean forcing in the CTR group which is denied in the TOPO group. Units: precipitation in mm/day, forcing in W/m2. (b) Composite height-longitude snapshot at 10°S latitude, showing Andean forcing in the CTR group at the 15th hour after branching off (10:00 am local time at 75°W). Units: K/day. (c) As in (b) but showing the horizontal structure of the vertically integrated (1000-100hPa) Andean forcing in the CTR group. Units: W/m2.

Figure 4.3 reviews the spatial and temporal structure of Andean convective forcing in the CTR group, which is necessary context for interpreting its denial in the TOPO group. An equatorial

(5°S-5°N) Hovmöller diagram (Fig 4.3a) of the composite (i.e. CTR ensemble mean) diurnal rainfall cycle illustrates the afternoon maxima over the continental interior (east of 75°W) and nocturnal oceanic maxima (west of 80°W); this phenomenon is discussed in Mapes et al. (2003) from the viewpoint of satellite observations. The Andean forcing maximizes around local afternoon at 75°W (Fig 4.3a). Andean forcing in the CTR group exhibits a robust diurnal cycle approximately in phase with the diurnal cycle of rainfall. Its vertical structure reveals heating in the middle troposphere and cooling in the lower levels (Fig 4.3b) consistent with deep, organized convection that includes lower-tropospheric cooling from evaporation of subcloud precipitate. The horizontal structure of the vertically integrated Andean forcing shows the intended alignment with Andean orography with peak net heating equatorward of 20°S (Fig 4.3c).

4.3.2 Responses of Amazonian precipitation driven by Andean convective heating

In the following analysis, for physical interpretability, I will focus attention on the CTR-minus-TOPO ensemble mean anomalies since this can be regarded as a proxy for mechanisms associated with *including* the effects of Andean convection.

The remote control of Amazonian rainfall by the Andes can be seen in Fig 4.4. In these 96 hours, the CTR group has four complete diurnal cycles with rainfall peaks reaching around 8 mm/day at local afternoon (Fig 4.4b). Amazonian precipitation reduces as a response to Andean convective heating, and such reduction exhibits a robust diurnal cycle (Fig 4.4c). The first rainfall reduction cycle sustains for about 37 hours while the second and the third ones sustain for about 24 hours. Although the rainfall reduction maximum averaged over the Amazon box reaches around -1

mm/day, it can be as much as -3 to -5 mm/day regionally (Fig 4.4a). The experiment setup and the short temporal scale of Amazonian precipitation responses suggest that it is through fast atmospheric processes that the Andes–Amazon connection operates. As an aside, I note that local to the Andes, latent heat release enhances precipitation (Fig 4.4a, blue shading), which is expected since the convergent circulations that feed vapor to a convective cell are partially driven by its heating (Holton 2004). This answers our question raised in the introduction that a portion of the WADA pattern can be attributed solely from the Andes.

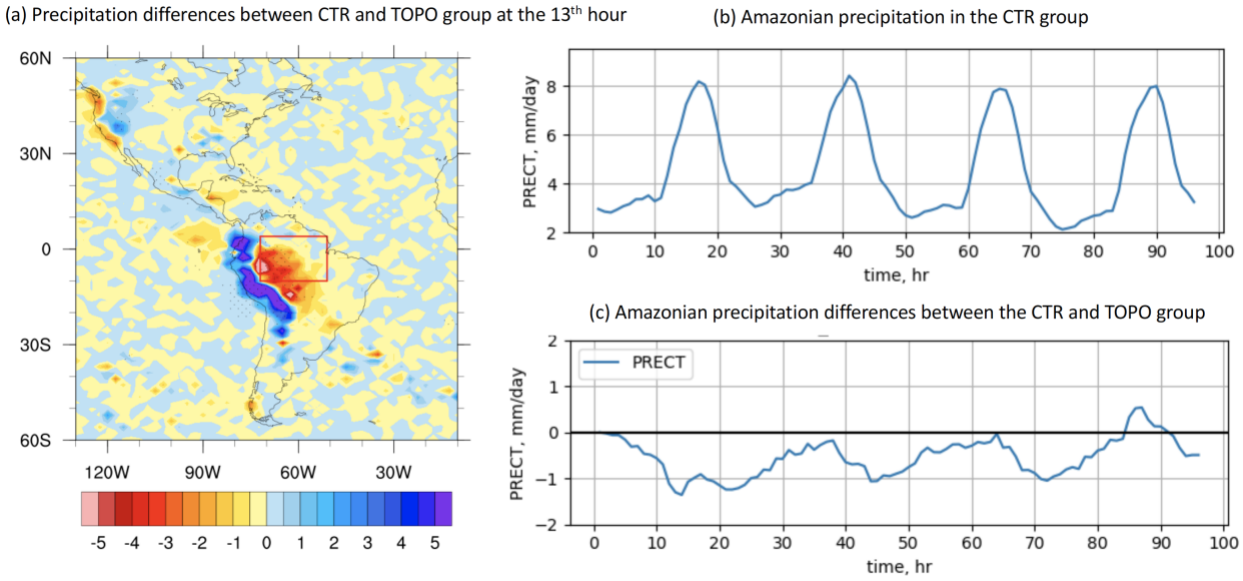

Figure 4.4 (a) Precipitation responses to Andean forcing (CTR minus TOPO) at the 13th hour after branching off. Areas with stippling indicate significant of 0.1 level in the student-t test. The Amazon area is defined with a red box (51°W-72°W, 10°S-4°N). Units: mm/day. (b) Precipitation averaged over the Amazon box in the CTR group. Units: mm/day. (c) Differences in precipitation averaged over the Amazon box between CTR and TOPO group. It depicts the Amazonian precipitation responses to Andean forcing. The initial dynamic adjustment takes about 10 hours, averaged mean during the 11th-96th hour is -0.573 mm/day. Units: mm/day.

4.3.3 Why does precipitation reduce over the Amazon?

In this section, I try to understand precipitation responses over the Amazon from the lenses of near-surface MSE, mechanics of GMS, CAPE, and the moisture budget.

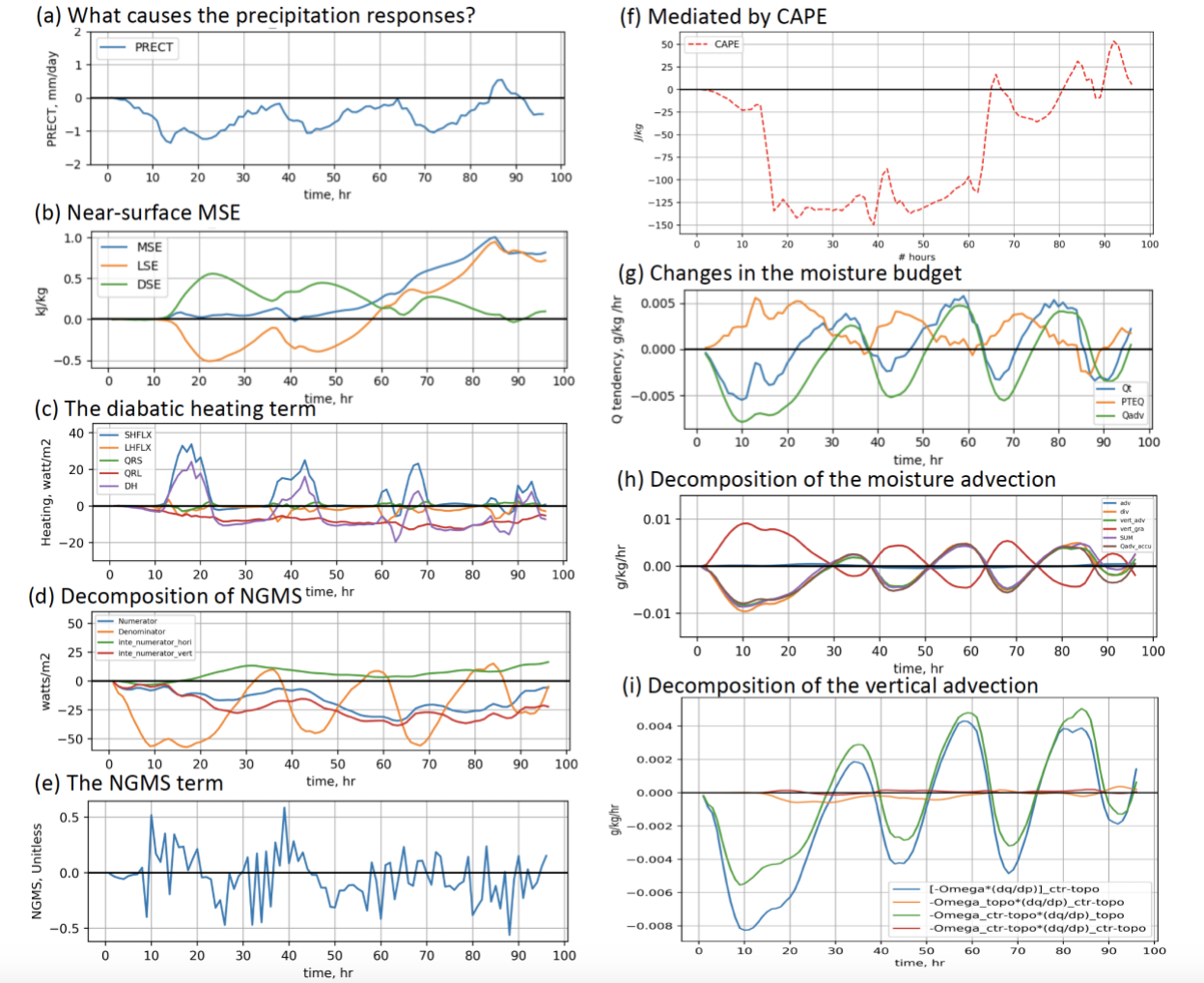

Figure 4.5 Summary schematic investigating causality of Andes-Amazon teleconnection dynamics (a) the signal of interest; i.e. same as Fig 4.4c, it is included here for easy visual comparison of following (b-i) subpanels where a variety of diagnostics are averaged over the Amazon. (b) CTR minus TOPO group in MSE (blue), LSE (yellow), and DSE (green) averaged in the lowest five model layers. Units: kJ/kg. (c) CTR minus TOPO group in surface sensible heat flux (blue), latent heat flux (yellow), vertically integrated solar heating rate (green) and longwave heating rate (red), as well as the sum of the four terms (purple). Units: watts/m2. (d) CTR minus TOPO group in the numerator (blue) and its horizontal, vertical component, and the denominator (yellow) of the NGMS. Units: watts/m2. (e) CTR minus TOPO group in the NGMS. Units: dimensionless. (f) CTR minus TOPO group in CAPE. Units: J/kg. (g) CTR minus TOPO group in the local rate of change in vertically integrated specific humidity (blue), total physics tendency of specific humidity PTEQ (yellow), total advection of specific humidity (green) inferred based on equation (4.9). Units: g/kg/hr. (h) Decomposition of the total advection of specific humidity based on equation (2.12). CTR minus TOPO group in $-\langle u\frac{\partial q}{\partial x}+v\frac{\partial q}{\partial y}\rangle$ (blue), $-\langle q(\frac{\partial u}{\partial x}+\frac{\partial v}{\partial y})\rangle$ (yellow), $-\langle \omega\frac{\partial q}{\partial p}\rangle$ (green), $-\langle q\frac{\partial \omega}{\partial p}\rangle$ (red), the sum of the previous four terms (purple), and vertical integral of the total advection of specific humidity inferred based on

equation (4.9) (brown). Units: g/kg/hr. (i) CTR and TOPO group differences $\langle -\omega \frac{\partial q}{\partial p} \rangle_{CTR-TOPO}$ (blue), and its decomposition into three terms, $-\langle \omega_{TOPO} \left[\frac{\partial q}{\partial p}\right]_{CTR-TOPO} \rangle$ in yellow, $-\langle \omega_{CTR-TOPO} \left[\frac{\partial q}{\partial p}\right]_{TOPO} \rangle$ in green, $-\langle \omega_{CTR-TOPO} \left[\frac{\partial q}{\partial p}\right]_{CTR-TOPO} \rangle$ in red. Units: g/kg/hr. The fact that the sum of three individual components does not seem to equal to the original term $\langle -\omega \frac{\partial q}{\partial p} \rangle_{CTR-TOPO}$ (blue) is likely due to errors induced in gradient calculations which might be accumulated in the summation.

The changes of near-surface MSE induced by Andean convective heating do not seem to explain changes in precipitation over the Amazon (Fig 4.5b). Larger MSE in the lower troposphere is conducive to deep convection and rainfall, as seen in Hill et al. (2017). From this view, I should expect a reduction of lower-level MSE in the CTR group relative to the TOPO group if Amazonian rainfall is tele-connected via a near-surface MSE bridge. In contrast, in our experiment, relative to the TOPO group, the CTR group actually has a slightly *higher* near-surface MSE until the 60th hour, after which it increases even more (Fig 4.5b). The LSE component (i.e. vapor in energy units, $L_v q$) of MSE is mostly compensated by changes in the DSE ($C_p T + gz$) component before the 60th hour, after which elevated LSE dominates the MSE changes (Fig 4.5b). Despite the fact that it is more than compensated by sensible heating, I do view the initial low-level drying (reduced LSE) as causatively important, and will return to this shortly.

Meanwhile: Can the Amazonian precipitation changes be reconciled with a gross moist stability view instead? Based on equation (4.2), I can understand drivers of P-E from the diabatic heating term in the numerator and the NGMS term in the denominator. Differences of P-E averaged over the Amazon between CTR and TOPO group are very similar to changes of P (not shown). As a result, I can use (4.2) to understand changes of precipitation. The diabatic column heating term

consists of surface sensible heat flux and latent heat flux, vertically integrated shortwave and longwave heating rate. Sensible heat flux increases significantly during the local afternoon with a strong diurnal cycle but with peaks tapering down, while the longwave heating rate remains stably negative after the first few hours (Fig 4.5c). Changes in latent heat flux and shortwave heating rate are relatively negligible, and the sum of the four terms is mainly driven by the sum of sensible heat flux and longwave heating rate (Fig 4.5c). The numerator of the NGMS in equation (4.6) is mostly driven by the vertical advective term of MSE (Fig 4.5d). The NGMS term seems to have two cycles before the 45th hour with peak values around 0.5 but tends to be slightly negative afterward (Fig 4.5e). I found that the ratio between the diabatic heating term and the NGMS term shows irregular changes (not shown), which is not adequate to explain precipitation changes. Intriguingly, precipitation increases in the 85th-90th hour, during which both the diabatic term and the NGMS term are negative (Fig 4.5c, e), implying the combined effects of longwave cooling and NGMS might contribute to the rainfall enhancement during that period.

I next turn to the possibility of control-by-CAPE, which will turn out to be important but in ways that may be secondary to a progenitor signal transmitted through the low-level humidity field. Comparing to the TOPO group, the CTR group has a much lower CAPE over the Amazon during the 10th-80th hour, especially during the 20th-60th hour, associated with suppressed deep convection and rainfall (Fig 4.5f). This reduction of CAPE is linked to the boundary layer drying, which reduces dew point temperature and therefore CAPE (not shown), for the same reasons elaborated in Langenbrunner et al. (2019). Although this CAPE reduction is consistent with precipitation decrease due to Andean forcing, it cannot explain the very beginning of a

precipitation reduction, and I speculate that it is instead an internal feedback triggered by upstream causes linked to the humidity budget. It is worth pointing out that the Amazonian rainfall is susceptible to both Andean forcing and complex secondary feedbacks which could be developed later-on. The most effective way to disentangle the effects of Andean convection on Amazonian rainfall from other secondary feedbacks is to focus on the initial period right after branching off.

In the end, to find a causatively satisfying framework to interpret the origins of the Andes-to-Amazonian precipitation response dynamics, I delve into the moisture budget. In Fig 4.5g, the local rate of change in moisture is balanced by moisture changes due to physics package calculations and the total advection of moisture. During the initial period until the 30th hour, the total advection of moisture decreases (Fig 4.5g); during the same period, precipitation decreases and reaches diurnal minima (Fig 4.5a). The total advection of moisture provides the clean unidirectional causality during the initial period which provides a reasonable explanation of precipitation reduction over the Amazon. It is worth noting that the initial tropospheric drying due to advection is strong in the boundary layer (Fig 4.6e-h), which may lead to secondary feedbacks (e.g. subsequent CAPE reductions) acting to suppress rainfall over the Amazon despite re-moistening due to moisture advection at a later stage.

Based on (4.12), the total advection of specific humidity, which the above analysis has indicated is an important part of the causation, can be further decomposed into four terms, the horizontal advective term $-\left(u\frac{\partial q}{\partial x}+v\frac{\partial q}{\partial y}\right)$, the divergence term $-q\left(\frac{\partial u}{\partial x}+\frac{\partial v}{\partial y}\right)$, the vertical advective term $-\omega\frac{\partial q}{\partial p}$, and the vertical Omega gradient term $-q\frac{\partial \omega}{\partial p}$. Such decomposition is shown in Fig 4.5h. I

readily acknowledge that this “bottom-up” way of calculating total advection from model state variable snapshots is error prone and needs some careful consideration (e.g., avoiding unnecessary vertical interpolation from hybrid to pressure coordinates for vertical advection terms; using spherical harmonics to estimate gradients for horizontal terms). For validation and comparison, the accurate, residually-inferred, moisture total advection calculation based on (4.8) and (4.9) is also overlaid in Fig 4.5h (brown). The closeness of the total advection lines based on these two methods (purple vs. brown lines) justifies the decomposition results calculated using gradient terms, and demonstrates that the model output frequency is high enough to warrant such a reconstruction.

The results in Figure 4h suggest that the vertical circulations induced by Andean latent heating, through their influence on vertical moisture advection, are a key causative bridge. On the one hand, the divergence term (yellow) always balance with the vertical Omega gradient term (red) due to the continuity equation (4.11). On the other hand, the horizontal advective term (blue) is negligible compared to other terms. Therefore, the total advection as the sum of the four components (purple) is mostly determined by the vertical advective term (green).

Finally, to further understand whether the velocity or the moisture fields provide the dominant effect on the differences of the vertical advective term between CTR and TOPO group $\langle -\omega \frac{\partial q}{\partial p} \rangle_{CTR-TOPO}$(blue line in Fig 4.5i) , I use (4.14) to decompose it into $-\langle \omega_{TOPO} \left[\frac{\partial q}{\partial p}\right]_{CTR-TOPO} \rangle$ (yellow line in Fig 4.5i), $-\langle \omega_{CTR-TOPO} \left[\frac{\partial q}{\partial p}\right]_{TOPO} \rangle$ (green line in Fig 4.5i), and $-\langle \omega_{CTR-TOPO} \left[\frac{\partial q}{\partial p}\right]_{CTR-TOPO} \rangle$ (red line in Fig 4.5i). It is obvious that the differences of

the vertical advective term $\langle -\omega \frac{\partial q}{\partial p} \rangle_{CTR-TOPO}$ is driven by $-\langle \omega_{CTR-TOPO} \left[\frac{\partial q}{\partial p}\right]_{TOPO} \rangle$, i.e. differences of vertical velocity field between CTR and TOPO group, revealing the importance of the vertical velocity dynamic response to Andean forcing as critical to mediating the advective impacts on the Amazonian region.

4.4 Eastward expansion of the Andean vertical advection bridge

In section 4.3.3, I have shown that the vertical advective term $\langle -\omega \frac{\partial q}{\partial p} \rangle_{CTR-TOPO}$ is a first-order control on reductions of the total advection of moisture, which in turn provide the best explanation for initial reduction in Amazonian rainfall. This view is corroborated when I examine the 10°S latitude transect (Fig 4.6) during the initial period when the response signals are more of a direct response to Andean forcing and less of a mixed effect of Andean forcing plus gradually developing local feedbacks. Initially, only on the east flank of the Andes can the strong subsidence anomalies be found. Then, the horizontal scale of the sinking anomalies expands eastward progressively (Fig 4.6a-d) as expected through fast gravity wave radiation (Bretherton and Smolarkiewicz 1989; Cohen and Boos 2017; Halliday et al. 2018; Kalisch et al. 2016; Kiladis et al. 2009) with a co-located expansion of drying in the troposphere (Fig 4.6e-h). Consistently, in the middle troposphere, the vertical velocity anomalies gradually progress eastward during the 4th-11th hour with the subsequent eastward stride of specific humidity with a few hours lag (Fig 4.7). In order to put the Andean forced Amazonian rainfall response into a broader context, I define an Andean east flank region (red box on the left in Fig 4.7a) and an Amazon region (red box on the right in Fig 4.7a), based on which I analyzed the CMIP5 data archive (Table 4.1), satellite observations and reanalysis datasets. The 500hPa vertical velocity

(specific humidity) on the Andean east flank has a significant negative (positive) correlation with the precipitation over the Amazon (Fig C1). This suggests that realistic representations of the Andean east flank midlevel vertical velocity and humidity fields are associated with a model's skill in simulating Amazonian rainfall.

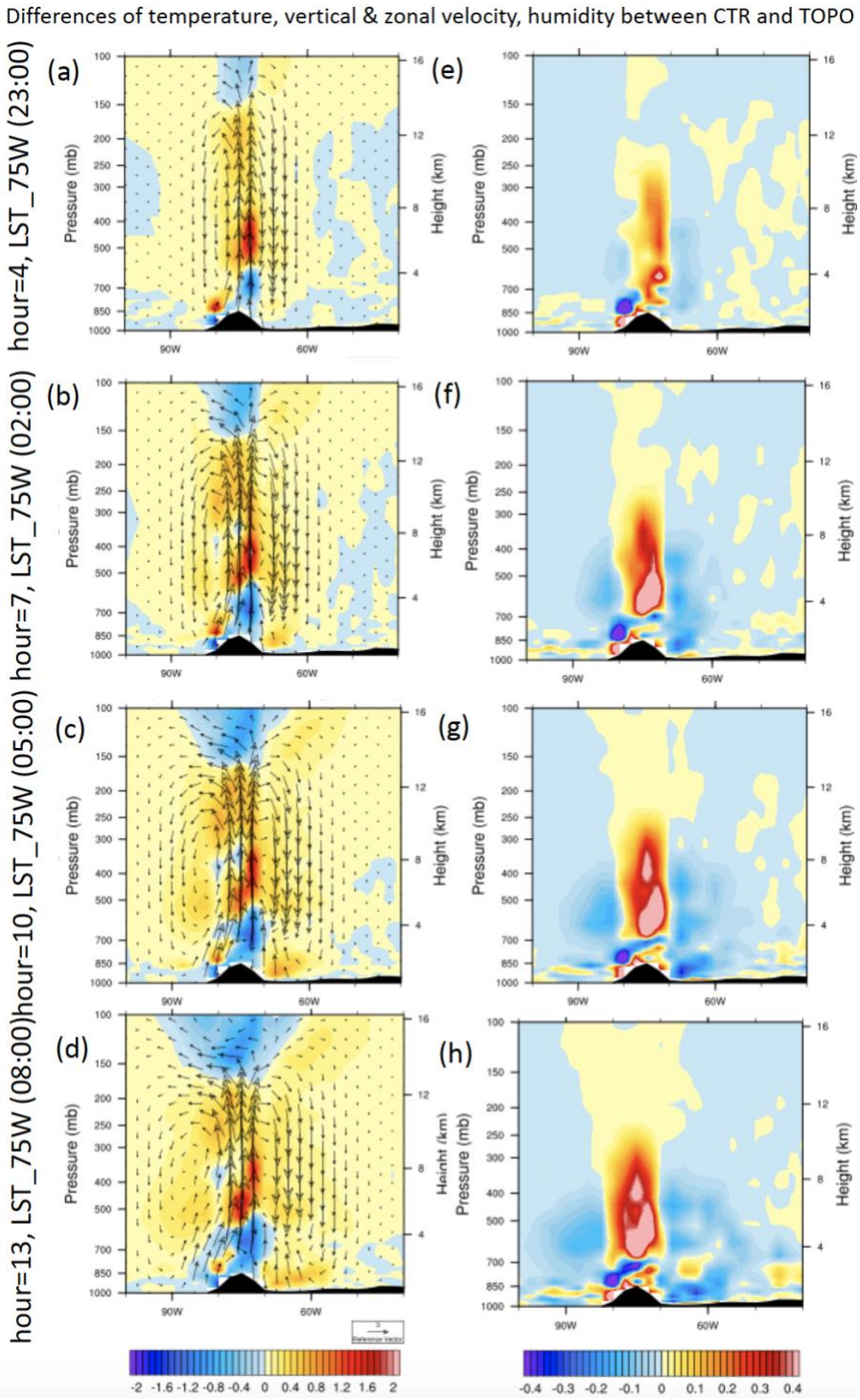

Figure 4.6 Transect at 10°S latitude. (a-d) Differences between CTR and TOPO group of temperature (shading), zonal, and vertical velocity (arrows), where vertical velocity is magnified 100 times for visibility. Units: temperature in Kelvin, wind in m/sec. (e-h) Differences between CTR and TOPO group of specific humidity. Units: g/kg. (a)(e) show the 4th hour after branching off (23:00 local time at 75°W). (b)(f) show the 7th hour after branching off (02:00 local time at 75°W). (c)(g) show the 10th hour after branching off (05:00 local time at 75°W). (d)(h) show the 13th hour after branching off (08:00 local time at 75°W).

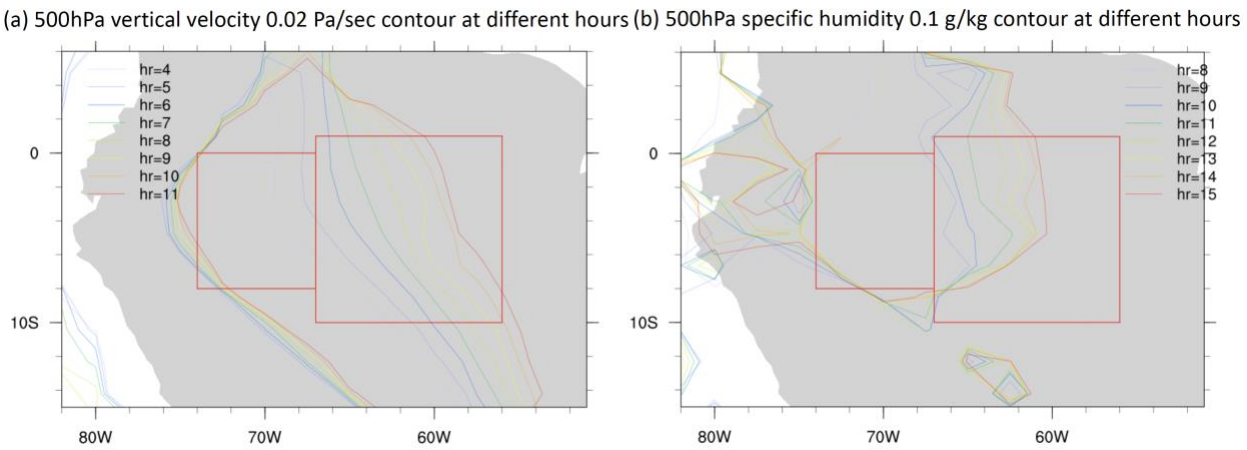

Figure 4.7 (a) Differences between CTR and TOPO group in the 500hPa vertical velocity at 0.02 Pa/sec contour during the 4th-11th hour after branching off. (b) Differences between CTR and TOPO group in the 500hPa specific humidity at 0.1 g/kg contour during the 8th-15th hour after branching off. The red box 1 on the right (67-56°W, 10°S-1°N) shows where the eastward progression notably occurs, and the red box 2 on the left (67-74°W, 8°S-equator) delineates the Andean east flank region. In Figure A1, precipitation is averaged over the Amazon box (box1). 500hPa vertical velocity and specific humidity are averaged over the Andean east flank region defined by box 2.

4.5 Conclusion and discussion

Motivated by the systematic "Wet Andes, Dry Amazon" (WADA) bias pattern seen in the CMIP5 archive over tropical South America, I designed a sensitivity experiment to surgically isolate the effects of Andean convective forcing on Amazonian precipitation processes. Based on an ensemble hindcast approach, I illustrate that complete denial of all Andean convective heating leads to a peak Amazonian precipitation decrease of approximately -1mm/day within 15 hours after initial Andean convective forcing and thereafter exhibits a strong diurnal cycle oscillating around ~ -0.5 mm/day reduction. The precipitation decrease over the Amazon is primarily controlled by the total advection of moisture driven by the vertical advective term $-\omega \frac{\partial q}{\partial p}$ and is also reinforced by local CAPE reductions related to the circulation-induced low-level drying. Differences in the vertical advective term between CTR and TOPO group $\langle -\omega \frac{\partial q}{\partial p} \rangle_{CTR-TOPO}$ are

traced to differences of vertical velocity between the two groups. Andean convective heating initially induces strong subsidence anomalies on its east flank, which then rapidly expand eastward into the Amazon basin through gravity wave radiation. As a consequence of the vertical advective term, a similar eastward expansion of tropospheric drying is easily visible and detectable on a similar horizontal length scale.

One advantage of our study is its capability to quantify what portion of the Amazonian rainfall dry biases may originally stem from Andean rainfall wet biases. In our 1989 DJF CTR group simulation, the Andean region has a mean rainfall of 6.37 mm/day and the number is 4.69 mm/day for the Amazon region. Using GPCP v2.3 as the benchmark, the implied rainfall biases are +2.69 mm/day over the Andes and -3.57 mm/day over the Amazon. That is, the Andean wet bias is $\frac{2.68}{6.37} \times 100\% = 42\%$ of the Andean mean rainfall. Recalling that the results of removing all of the condensational heating over the Andes had a rainfall reduction effect of -0.573 mm/day over the Amazon basin as depicted in Fig 4.4a (averaging over the 11th-96th hour in Fig 4c), and assuming a simple linear scaling, the implied amount of Amazonian rainfall biases due to Andean wet biases can be calculated as $-0.573 \times 0.42 = -0.24$ mm/day. This implies that approximately $\frac{-0.24}{-3.57} \times 100\% = 7\%$ of the Amazonian rainfall dry biases in our CTR group using CESM v1.1 could be directly attributed to the fast advective bridge from wet biases over the Andes. This 7% seems trivial. However, I suspect his number to be much larger over western part of the Amazon where it is more susceptible to Andean forced vertical advective drying (Fig 4.6), and the mean rainfall dry bias (-1 to -3 mm/day) is smaller than the eastern Amazon (Fig 4.2). Another caveat of such calculation is that the TOPO group only runs for 4 days, such experiment is incapable of detecting the effects of Andean convection on Amazonian rainfall on

longer synoptic timescales which the initial daily response could be strengthened (Langenbrunner et al. 2019).

The immediate implication is that, since the portion of the Amazonian rainfall dry bias that directly originates from excess Andean convection is quite small, CESM model developers focusing on improving Amazonian hydroclimate might be better served by prioritizing their efforts and resources into fixing other sources of Amazonian rainfall biases such as land parameterizations, or cloud treatments that impact the forest directly. However, this assumes that secondary amplification on longer timescales, such as that already observed intermittently via CAPE feedbacks, is not prone on longer timescales to further amplifying the initial effects of Andes forcing. Such nonlinear amplification has been observed on > 4-day timescales in this regional system before by Langenbrunner et al. (2019) through forest-mountain reinforcement and could also occur through land-atmosphere coupling connected wet- to dry-seasons (Levine et al. 2019). Obviously, extended versions of these simulations would be needed to know if the system dynamics to Andean forcing are likewise amplifying or, perhaps more likely, buffering. Meanwhile, other modeling systems beyond CESM could use a similar mechanism denial strategy to assess what fraction of Amazonian rainfall dry biases are caused by Andean wet biases in their own GCM of interest, which could be beneficial to their model development strategies.

Some readers may question our experiment setup about the “energy leakage” issue. In our experiment design, our main purpose is to causatively determine the effects of Andean convective forcing on Amazonian rainfall. To achieve this, I first have a full-fledged CTR group

simulation, and then have a second TOPO group in which I surgically mute the convective heating over mountainous regions. By comparing these two groups of simulations, I can separate the effects of Andean convective heating on Amazonian rainfall. The tradeoff of such experiment design is the violation of energy conservation. Simulations in the second TOPO group allow precipitation to occur but deny latent heat release from condensation over areas where $SGH30 \geq 200m$ and linearly damp condensational latent heat release over areas where $100m \leq SGH30 < 200m$. This means the annihilation of the latent heat energy encapsulated in precipitation, or the "energy leakage" issue. In the TOPO group, the interference only deals with temperature tendencies (rather than moisture tendencies), such that the energy leakage in the TOPO group would be concerning if the increase of the column MSE over the Andes is dominated by DSE. But this is not true (Fig C2), implying that the impact of energy leakage is minimal in our setup. It is also reassuring to see that similar experiment design strategies are adopted in other studies (Sun and Barros 2015a; Sun and Barros 2015b) where surface evaporation is artificially removed to investigate the local and remote impacts of evapotranspiration on convection and precipitation over South America.

In addition, the differences between CTR and TOPO groups are due to muting condensational heating over mountains and plateaus all over the globe (rather than over the Andean orography only). In our simulations, I scrutinized the precipitation responses over South America in the first few days, during which the remote influences of shutting down condensational heating from other mountainous ranges and plateaus are quite limited. Since I only analyzed the South American region, I encourage other researchers to use our datasets to investigate the relationship

of rainfall biases between mountainous regions and adjacent lowlands in other parts of the world where the dipole patterns of rainfall biases are also quite common as can be seen in Figure 1.1.

Our study adds to the evidence of an interesting positive regional feedback within the SAMS system over the Andes-Amazon region. During the wet season, SALLJ transports moisture and MSE from the Amazon towards the Andes, increasing the Andean convection and precipitation. Based on our experiment, this rainfall increase over the Andes can decrease Amazonian rainfall through the vertical advective drying. Amazonian rainfall reduction decreases local ET, which is a known effect to further strengthen the Andean rainfall from different perspectives. One view is through the lens of CAPE reduction and increased divergence anomalies over the Amazon (Sun and Barros 2015a); the other notion is that Amazonian ET reduction help elevate local surface Bowen ratio and deepen the boundary layer depth, which leads to a stronger MSE transport towards the Andes (Langenbrunner et al. 2019). As a result of the positive feedback, our study underscores the importance of looking at the Andes-Amazon system holistically, and the Andes-Amazon ought to be assessed together in climate change studies. In a warmer climate, Amazonia is projected to experience decreases of rainfall (Pascale et al. 2019), a strengthening and lengthened dry season (Joetzjer et al. 2013), more frequent and exacerbated meteorological droughts (Duffy et al. 2015). Our sensitivity study suggests that future changes of Andean convection and precipitation may affect Amazonian hydroclimate through intimate feedbacks. For instance, a decrease or increase of Andean rainfall in the future (Neukom et al. 2015; Seiler et al. 2013; Urrutia and Vuille 2009) might alleviate or exacerbate the rainfall deficit problem over the Amazon.

Chapter 5. Conclusion

5.1 Summary of results

This thesis aims to broaden our knowledge of the role of convection in mediating inter-component (land-atmosphere) coupling dynamics, as well as inter-regional (Andes-Amazon) teleconnections, using two novel numerical modeling approaches – cloud superparameterization and a new form of orographic latent heating denial. First, from a global perspective, based on the Global Land-Atmosphere Coupling Experiment (GLACE) protocol, I investigated the effects of explicit convection on land-atmosphere coupling through the hydrologic pathway. Then, I illustrated that explicit convection changes the thermal land-atmosphere coupling for distinct reasons over the Arabian Peninsula and the southwestern United States. Finally, in a detailed analysis of the Amazon wet season hydroclimate, based on an ensemble hindcast sensitivity experiment augmented with mechanism denial, I examined how Andean convection remotely controls a portion of Amazonian rainfall.

In Chapter 2, I used a standard technique to quantify the hydrologic land-atmosphere coupling strength by synchronizing soil moisture state variables across ensemble simulations known as the GLACE protocol. Although this technique is well established and has been applied to standard climate models, I am the first to deploy such a strategy to next-generation prototype climate simulations, in which convection is "super-parameterized" i.e. explicitly simulated by embedded 2D Cloud-Resolving-Models (CRMs) in every grid column of the traditional climate model. Over weekly-to-subseasonal timescales, comparing to parameterized convection, explicit convection reduces the hydrologic land-atmosphere coupling on a global scale during boreal

summer. Such reduction is exceptionally substantial over central Eurasia, northern Africa, central United States, and tropical South America. The coupling strength reduction primarily comes from the atmospheric segment (evapotranspiration–precipitation) rather than the terrestrial segment (soil moisture–evapotranspiration). Over seasonal timescales, the hydrologic land-atmosphere coupling mainly reflects on the response limb (impacts of precipitation on terrestrial water storage), rather than the forcing limb (impacts of terrestrial water storage on precipitation), and the effects of explicit convection on seasonal coupling are minimal.

In Chapter 3, I showed that unlike its global damping impacts on the hydrologic coupling, explicit convection only changes the thermal coupling regionally. Such regional effects are evident in both the GLACE-type and the AMIP-type simulations (using metrics of terrestrial coupling indexes). Analysis of the underlying mechanism argues that decreased soil moisture–temperature coupling strength over the Arabian Peninsula occurs because explicit convection produces less but more realistic local time-mean rainfall, pushing the soil moisture regime further away from the optimal transitional regime that is necessary for strong coupling. In contrast, explicit convection enhances the thermal coupling strength over the southwestern United States and northern Mexico for different reasons that are as yet unclear. Such regional enhancement of thermal coupling is not attributable to local precipitation or soil moisture since a broad range of statistical measures suggest a high degree of similarity between two groups. Instead, the enlarged thermal coupling over the southwestern United States is related to a mysterious surface Bowen ratio enhancement. This led me to a surprising discovery, that explicit convection enlarges the land surface Bowen ratio over the majority of global land. On a global-average sense, this enhancement of the Bowen ratio leads to somewhat better agreements with

observationally derived FLUXNET-MTE datasets. Across multiple model version pairs of using parameterized vs. explicit convection, climate simulations suggest that the explicit convection has a systematic and robust effect on the land surface Bowen ratio enhancement. Furthermore, comparing to parameterized convection, explicit convection exhibits a remarkably stronger amplification effect on land surface Bowen ratio in a climate with elevated CO_2 levels.

Chapter 4 is motivated by a systematic zonal dipole pattern of rainfall biases in CMIP5 simulations over tropical South America, which I have labeled the "Wet Andes, Dry Amazon" (WADA) bias to suggest the potential of coupling between Andean and Amazonian hydroclimate. This chapter conceives an experimental design in which the convective forcing over the Andes is artificially muted in an experiment group. Based on the control and experiment group of simulations, this allows a causatively unambiguous way to separate the effects of Andean convective heating on Amazonian rainfall processes. I find that Andean convective forcing causes an Amazonian rainfall reduction of -0.57 mm/day averaging over the first 4 days. I then attempt to infer the causality from multiple complementary approaches that are widely used in modern tropical climate dynamics. Neither low-level moist static energy nor the mechanics of moist gross stability can explain the response of Amazonian rainfall. However, changes in the moisture budget, especially in the vertical advective term, appear to provide a consistent explanation for the reduction of Amazonian rainfall, which can be ultimately traced to differences in the vertical velocity field linked to the balanced motions that associated with convective heating over the mountains, and their advective consequences. Signals of Amazonian responses are less corrupted by growing non-linear feedbacks in the initial period of the experiment, and it is a focus on this initial drift structure between experiment and control group

that provides easily visible vertical velocity anomalies due to Andean forcing gradually expanding eastward, accompanied by tropospheric drying anomalies seen on similar horizontal length scales. Assuming linear scaling, our mechanism denial experiment implies that in CESM v1 during wet season, 7% of the Amazonian rainfall dry bias is attributable to rainfall wet biases over the Andes, though nonlinear feedbacks could either amplify or damp this on longer timescales.

5.2 Future research directions

Implications and suggestions for future work stemming from Chapter 2

As the climate community moves towards the Global Cloud-Resolving Models (GCRMs) (Fukutomi et al. 2016; Randall 2013; Sasaki et al. 2016; Satoh et al. 2019; Stevens et al. 2019), the effects of explicit convection found by using the SP framework may be viewed as setting expectations for potentially similar behaviors emerging from GCRMs, and attention given to results in Chapter 2-3 may help prevent from being caught off guard by unexpected GCRM behaviors in the near future. Chapter 2 concludes that during boreal summer, explicit convection attenuates the GLACE-type soil moisture–precipitation coupling strength, or the impacts of soil moisture on rainfall over subseasonal timescales. For the subseasonal-to-seasonal (S2S) prediction community (Brunet et al. 2010; White et al. 2017), this implies that in the era of GCRMs in the coming decade, over the mid-latitude regions of transitional soil moisture regime, including the agriculturally important central U.S., predictability of rainfall may be more dominated by remote oceanic SSTs and atmospheric intra-seasonal oscillations in the tropics like the Madden-Julian Oscillation (MJO), and less should be expected from local soil moisture assimilations.

Some limitations of Chapter 2 are important to mention. The preliminary work does not satisfactorily explain why explicit convection can mute the soil moisture–precipitation coupling on a global scale; neither does it provide direct evidence to prove whether or not it is an improvement since the GLACE-type diagnostic is not observable. To adequately address these limitations, one could take advantage of recent field campaigns (Fast et al. 2019a; Fast et al. 2019b) and conduct single-column simulations with parameterized vs. explicit convection at the U.S. Southern Great Plains site where ample observations are available. The advice is to use other methodologies that are more physically interpretable and friendly to observations. For instance, to examine the sensitivity of soil moisture–precipitation coupling to the parameterization in the mass-flux closure of convection, transpiration of vegetation (Williams 2019), and representation of agricultural practices (McDermid et al. 2019); to dissect the soil moisture–evaporation feedback by considering soil evaporation, transpiration and canopy interception separately (Berg and Sheffield 2019); and to utilize the mixing diagram approach on quantifications of local coupling (Santanello et al. 2009b). Furthermore, this chapter uncovers the systematic effects of explicit convection on soil moisture–precipitation coupling on sub-seasonal timescales, but the consequences on extreme hydrologic events are not explored. Given the role of soil moisture on the intensity and persistence of droughts (Roundy and Wood 2015; Wu and Zhang 2013; Zaitchik et al. 2013), it is meaningful to know whether or not explicit convection can alter the impacts of soil moisture on extreme hydrologic events like droughts. Lastly, in a climate with elevated CO_2 levels, GCMs with explicit convection are known to behave differently comparing to those with parameterized convection (Arnold et al. 2014; Kooperman et al. 2016), it would be interesting to see if explicit convection would simulate soil

moisture–precipitation feedbacks and their impacts on future droughts differently in a warmer climate by following the CMIP5-GLACE protocol (Lorenz et al. 2016; Seneviratne et al. 2013; Zhou et al. 2019) deployed on superparameterized simulations.

Implications and suggestions for future work stemming from Chapter 3

Chapter 3 suggests that explicit convection enhances soil moisture–temperature coupling over the southwestern U.S. and northern Mexico. This is useful context for Numerical Weather Prediction (NWP) and S2S communities as the soil moisture assimilation may increase the subseasonal predictability of regional near-surface temperature in the GCRMs. Another mystery of Chapter 3 is that explicit convection systematically enhances the land Bowen ratio which proves to be an improvement on a global-average sense. It is of great intellectual and practical benefits to probe the why question since the Bowen ratio has direct implications on surface temperature extremes, and future GCRMs may exhibit similar behaviors. Bowen ratio is a reflection of the surface energy partitioning, which is extremely complex in modern GCMs. Over central U.S. and northeastern Amazonia, the systematic Bowen ratio enhancement effects are particularly strong. This may imply that the underlying vegetation transpiration–surface climate feedbacks are represented quite differently due to explicit convection [*DeMott et al.,* 2007]. Since the transpiration pull is needed for a sustained supply of water for photosynthesis, which fixes carbon in the terrestrial biosphere, it would be an intriguing investigation into the regional impacts of explicit convection on carbon fixation.

Suggestions for future work stemming from Chapter 3 are summarized as follows. First of all, it is worthwhile using a recently launched satellite (e.g., Soil Moisture Active/Passive, or the

SMAP) mission for model evaluation purposes (Dong and Crow 2018). Furthermore, given the regionally strong effects of explicit convection on the thermal coupling, a valuable research pathway is to scrutinize its consequences on extreme temperature events since soil moisture–atmosphere feedbacks are known to increase the intensity and duration of heatwave events (Fischer et al. 2007a; Lorenz et al. 2010; Seo et al. 2019). Lastly, to investigate the effects of explicit convection on soil moisture–temperature feedbacks under climate change scenarios, the suggestion is to adopt a recently proposed theoretical approach based on the soil moisture–evaporative fraction relationship, using which the thermal coupling signal obtained from regular climate change simulations can be equivalent to that obtained from the costly CMIP5-GLACE simulations (Schwingshackl et al. 2018), which can be challenging to simulate in computationally intensive superparameterized models.

Implications and suggestions for future work stemming from Chapter 4

An orographic dipole structure of rainfall biases in CMIP5 is ubiquitous over the Himalayan Mountains – Indian lowland area, the Rocky Mountains – central U.S. area, as well as the WADA pattern investigated in Chapter 4, as can be seen in Figure 1.1. This might be related to the hybrid sigma coordinate employed in most GCMs. It is a known fact that precipitation in GCMs tends to be overestimated over orographic regions and underestimated over adjacent low lands due to computational errors of pressure gradient force calculation near steep topographies in hybrid sigma coordinate (Li et al. 2014; Maloney and Zhang 2016; Yu et al. 2015; Zou et al. 2016). Efforts of designing the cut-cell method in representing the topography might be fruitful in this regard (Lock et al. 2012; Shaw and Weller 2016). Secondly, our sensitivity results emphasize that Andean convection exert influence on Amazonian rainfall through mediations

from the dynamic and moisture fields over the Andean east flank in the middle troposphere. Model evaluators interested in the Amazonian hydroclimate are encouraged to incorporate relevant processes in their evaluation metrics. On the observational side, the ground based weather stations are scare over the Andean east flank region (Xavier et al. 2016). A lack of high-quality observation datasets poses a challenge for model evaluation on the Andean driven mechanism. The Amazon Dense Global Navigation Satellite System (GNSS) Meteorological Network and the recent GoAmazon2014/2015 campaign (Machado et al. 2018; Martin et al. 2016; Schiro et al. 2018; Wang et al. 2018) are all located around central Amazonian basin at Manaus (60°W). Similar observational efforts are strongly encouraged over the Andean east flank region. Thirdly, to better pinpoint the moisture sources and sinks over the Andes-Amazon region, this chapter encourages usage of the isotopic analysis (Risi et al. 2013; Wright et al. 2017) to separate moisture sources from adjacent oceans to rainforest ET since the latter is relatively enriched in deuterium; and the trajectory-based methods (Drumond et al. 2008; Jiang et al. 2017).

This chapter demonstrates that based on an ensemble sensitivity experiment, for the CESM v1 in the CTR simulation, 7% of the Amazon basin-wide rainfall dry bias is attributable to the fast (< 4 day) response to Andean wet biases during the wet season. It is important to identify if this sensitivity grows or decays on longer timescales, as either outcome is possible, and this would alter the view of the importance of this teleconnection. Meanwhile, this result has so far only been investigated in a single GCM, the CESM. Other researchers can deploy similar mechanism denial experiments to be informed of what fraction of the Amazonian rainfall biases, in their GCMs, is due to biases from the Andes, as opposed to other sources of biases like SSTs, land

parameterizations, convection treatments. This is beneficial for a better allocation of efforts and resources for model developments. Our study also adds to evidence pointing to positive regional feedbacks within the SAMS system over the Andes-Amazon region, which argue for analyzing the Andes-Amazon system holistically. In the future, Amazonia is projected to experience rainfall reduction (Pascale et al. 2019), a strengthening and lengthened dry season (Joetzjer et al. 2013), more frequent and exacerbated meteorological droughts (Duffy et al. 2015). This chapter suggests that future changes of Andean precipitation may affect Amazonian hydroclimate through complex feedbacks that involve vertical advection of vapor by the circulations induced by mountain convective heating, and consequent impacts on the potential buoyancy of Amazonian boundary layer air parcels.

Bibliography

Adler, R. F., and Coauthors, 2003: The version-2 global precipitation climatology project (GPCP) monthly precipitation analysis (1979-present). *J Hydrometeorol*, **4,** 1147-1167.

Anber, U., P. Gentine, S. Wang, and A. H. Sobel, 2015: Fog and rain in the Amazon. *Proc Natl Acad Sci U S A*, **112,** 11473-11477.

Arnold, N. P., M. Branson, M. A. Burt, D. S. Abbot, Z. M. Kuang, D. A. Randall, and E. Tziperman, 2014: Effects of explicit atmospheric convection at high CO2. *Proceedings of the National Academy of Sciences of the United States of America*, **111,** 10943-10948.

Avissar, R., and D. Werth, 2005: Global hydroclimatological teleconnections resulting from tropical deforestation. *J Hydrometeorol*, **6,** 134-145.

Barros, V. R., and M. E. Doyle, 2018: Low-level circulation and precipitation simulated by CMIP5 GCMS over southeastern South America. *International Journal of Climatology*, **38,** 5476-5490.

Benedict, J. J., and D. A. Randall, 2009: Structure of the Madden-Julian Oscillation in the Superparameterized CAM. *J. Atmos. Sci.*, **66,** 3277-3296.

Benedict, J. J., E. D. Maloney, A. H. Sobel, and D. M. W. Frierson, 2014: Gross Moist Stability and MJO Simulation Skill in Three Full-Physics GCMs. *J. Atmos. Sci.*, **71,** 3327-3349.

Bentsen, M., and Coauthors, 2013: The Norwegian Earth System Model, NorESM1-M – Part 1: Description and basic evaluation of the physical climate. *Geosci. Model Dev.*, **6,** 687-720.

Berg, A., and J. Sheffield, 2019: Historic and Projected Changes in Coupling Between Soil Moisture and Evapotranspiration (ET) in CMIP5 Models Confounded by the Role of Different ET Components. *Journal of Geophysical Research-Atmospheres*, **124,** 5791-5806.

Berg, A., B. R. Lintner, K. L. Findell, S. Malyshev, P. C. Loikith, and P. Gentine, 2014: Impact of Soil Moisture-Atmosphere Interactions on Surface Temperature Distribution. *Journal of Climate*, **27,** 7976-7993.

Berg, A., and Coauthors, 2015: Interannual Coupling between Summertime Surface Temperature and Precipitation over Land: Processes and Implications for Climate Change*. *Journal of Climate*, **28,** 1308-1328.

Bi, D. H., and Coauthors, 2013: The ACCESS coupled model: description, control climate and evaluation. *Australian Meteorological and Oceanographic Journal*, **63,** 41-64.

Boers, N., N. Marwan, H. M. Barbosa, and J. Kurths, 2017: A deforestation-induced tipping point for the South American monsoon system. *Sci Rep*, **7,** 41489.

Bretherton, C. S., and P. K. Smolarkiewicz, 1989: Gravity-Waves, Compensating Subsidence and Detrainment around Cumulus Clouds. *J. Atmos. Sci.*, **46,** 740-759.

Brunet, G., and Coauthors, 2010: Collaboration of the Weather and Climate Communities to Advance Subseasonal-to-Seasonal Prediction. *Bulletin of the American Meteorological Society*, **91,** 1397-1406.

Chavez, S. P., and K. Takahashi, 2017: Orographic rainfall hot spots in the Andes-Amazon transition according to the TRMM precipitation radar and in situ data. *Journal of Geophysical Research: Atmospheres*, **122,** 5870-5882.

Chen, Y., B. Langenbrunner, and J. T. Randerson, 2018: Future Drying in Central America and Northern South America Linked With Atlantic Meridional Overturning Circulation. *Geophysical Research Letters*, **45,** 9226-9235.

Cohen, N. Y., and W. R. Boos, 2017: The influence of orographic Rossby and gravity waves on rainfall. *Quarterly Journal of the Royal Meteorological Society*, **143,** 845-851.

Cook, B. I., G. B. Bonan, and S. Levis, 2006: Soil Moisture Feedbacks to Precipitation in Southern Africa. *Journal of Climate*, **19,** 4198-4206.

Demott, C. A., D. A. Randall, and M. Khairoutdinov, 2007: Convective precipitation variability as a tool for general circulation model analysis. *Journal of Climate*, **20,** 91-112.

Dirmeyer, P. A., 2011: The terrestrial segment of soil moisture–climate coupling. *Geophys. Res. Lett.*, **38,** L16702-L16702.

Dix, M., and Coauthors, 2013: The ACCESS coupled model: documentation of core CMIP5 simulations and initial results. *Australian Meteorological and Oceanographic Journal*, **63,** 83-99.

Dong, J. Z., and W. T. Crow, 2018: Use of Satellite Soil Moisture to Diagnose Climate Model Representations of European Soil Moisture-Air Temperature Coupling Strength. *Geophysical Research Letters*, **45,** 12884-12891.

Donner, L. J., and Coauthors, 2011: The Dynamical Core, Physical Parameterizations, and Basic Simulation Characteristics of the Atmospheric Component AM3 of the GFDL Global Coupled Model CM3. *Journal of Climate*, **24,** 3484-3519.

Drumond, A., R. Nieto, L. Gimeno, and T. Ambrizzi, 2008: A Lagrangian identification of major sources of moisture over Central Brazil and La Plata Basin. *Journal of Geophysical Research-Atmospheres*, **113**.

Duffy, P. B., P. Brando, G. P. Asner, and C. B. Field, 2015: Projections of future meteorological drought and wet periods in the Amazon. *Proceedings of the National Academy of Sciences of the United States of America*, **112,** 13172-13177.
Dufresne, J.-L., and Coauthors, 2013: Climate change projections using the IPSL-CM5 Earth System Model: from CMIP3 to CMIP5. *Climate Dynamics*, **40,** 2123-2165.
Entekhabi, D., I. Rodriguez-Iturbe, and R. L. Bras, 1992: VARIABILITY IN LARGE-SCALE WATER-BALANCE WITH LAND SURFACE ATMOSPHERE INTERACTION. *JOURNAL OF CLIMATE*, **5,** 798-813.
Fast, J. D., L. K. Berg, Z. Feng, F. Mei, R. Newsom, K. Sakaguchi, and H. Xiao, 2019a: The Impact of Variable Land-Atmosphere Coupling on Convective Cloud Populations Observed During the 2616 HI-SCALE Field Campaign. *Journal of Advances in Modeling Earth Systems*, **11,** 2629-2654.
Fast, J. D., and Coauthors, 2019b: Overview of the HI-SCALE Field Campaign: A New Perspective on Shallow Convective Clouds. *Bulletin of the American Meteorological Society*, **100,** 821-840.
Ferguson, C. R., E. F. Wood, and R. K. Vinukollu, 2012: A Global Intercomparison of Modeled and Observed Land-Atmosphere Coupling. *Journal of Hydrometeorology*, **13,** 749-784.
Fernandes, K., A. Giannini, L. Verchot, W. Baethgen, and M. Pinedo-Vasquez, 2015: Decadal covariability of Atlantic SSTs and western Amazon dry-season hydroclimate in observations and CMIP5 simulations. *Geophysical Research Letters*, **42,** 6793-6801.
Findell, K. L., P. Gentine, B. R. Lintner, and C. Kerr, 2011: Probability of afternoon precipitation in eastern United States and Mexico enhanced by high evaporation. *Nature Geoscience*, **4,** 434-439.
Fischer, E. M., S. I. Seneviratne, D. Luthi, and C. Schar, 2007a: Contribution of land-atmosphere coupling to recent European summer heat waves. *Geophysical Research Letters*, **34,** L06707-L06707.
Fischer, E. M., S. I. Seneviratne, P. L. Vidale, D. Luthi, and C. Schar, 2007b: Soil moisture - Atmosphere interactions during the 2003 European summer heat wave. *Journal of Climate*, **20,** 5081-5099.
Froidevaux, P., L. Schlemmer, J. Schmidli, W. Langhans, and C. Schär, 2014: Influence of the Background Wind on the Local Soil Moisture–Precipitation Feedback. *J. Atmos. Sci.*, **71,** 782-799.
Fukutomi, Y., C. Kodama, Y. Yamada, A. T. Noda, and M. Satoh, 2016: Tropical synoptic-scale wave disturbances over the western Pacific simulated by a global cloud-system resolving model. *Theoretical and Applied Climatology*, **124,** 737-755.
Gent, P. R., and Coauthors, 2011: The Community Climate System Model Version 4. *Journal of Climate*, **24,** 4973-4991.
Gettelman, A., and Coauthors, 2010: Multimodel assessment of the upper troposphere and lower stratosphere: Tropics and global trends. *Journal of Geophysical Research-Atmospheres*, **115**.
Guillod, B. P., and Coauthors, 2014: Land-surface controls on afternoon precipitation diagnosed from observational data: uncertainties and confounding factors. *Atmospheric Chemistry and Physics*, **14,** 8343-8367.
Guo, Z. C., and Coauthors, 2006: GLACE: The Global Land-Atmosphere Coupling Experiment. Part II: Analysis. *Journal of Hydrometeorology*, **7,** 611-625.
Halliday, O. J., S. D. Griffiths, D. J. Parker, A. Stirling, and S. Vosper, 2018: Forced gravity waves and the tropospheric response to convection. *Quarterly Journal of the Royal Meteorological Society*, **144,** 917-933.
Hans, H., and Coauthors, 2019: Global reanalysis: goodbye ERA-Interim, hello ERA5. *ECMWF Newsletter*.
Hauser, M., R. Orth, and S. I. Seneviratne, 2017: Investigating soil moisture-climate interactions with prescribed soil moisture experiments: an assessment with the Community Earth System Model (version 1.2). *Geoscientific Model Development*, **10,** 1665-1677.
Hill, S. A., Y. Ming, I. M. Held, and M. Zhao, 2017: A Moist Static Energy Budget-Based Analysis of the Sahel Rainfall Response to Uniform Oceanic Warming. *Journal of Climate*, **30,** 5637-5660.
Hirsch, A. L., A. J. Pitman, S. I. Seneviratne, J. P. Evans, and V. Haverd, 2014: Summertime maximum and minimum temperature coupling asymmetry over Australia determined using WRF. *Geophys. Res. Lett.*, **41,** 1546-1552.
Hohenegger, C., P. Brockhaus, C. S. Bretherton, and C. Schar, 2009: The Soil Moisture-Precipitation Feedback in Simulations with Explicit and Parameterized Convection. *Journal of Climate*, **22,** 5003-5020.
Huffman, G. J., R. F. Adler, D. T. Bolvin, and G. J. Gu, 2009: Improving the global precipitation record: GPCP Version 2.1. *Geophys. Res. Lett.*, **36,** L17808-L17808.
Iacono, M. J., J. S. Delamere, E. J. Mlawer, M. W. Shephard, S. A. Clough, and W. D. Collins, 2008: Radiative forcing by long-lived greenhouse gases: Calculations with the AER radiative transfer models. *Journal of Geophysical Research-Atmospheres*, **113**.
Inoue, K., and L. Back, 2015: Column-Integrated Moist Static Energy Budget Analysis on Various Time Scales during TOGA COARE. *J. Atmos. Sci.*, **72,** 1856-1871.

Insel, N., C. J. Poulsen, and T. A. Ehlers, 2010: Influence of the Andes Mountains on South American moisture transport, convection, and precipitation. *Climate Dynamics*, **35,** 1477-1492.
IPCC, 2014: Evaluation of Climate Models. *Climate Change 2013 - The Physical Science Basis*, T. F. Stocker, and Coauthors, Eds., Cambridge University Press, 741-866.
Jiang, Z. H., S. Jiang, Y. Shi, Z. Y. Liu, W. Li, and L. Li, 2017: Impact of moisture source variation on decadal-scale changes of precipitation in North China from 1951 to 2010. *Journal of Geophysical Research-Atmospheres*, **122,** 600-613.
Joetzjer, E., H. Douville, C. Delire, and P. Ciais, 2013: Present-day and future Amazonian precipitation in global climate models: CMIP5 versus CMIP3. *Climate Dynamics*, **41,** 2921-2936.
Kalisch, S., H. Y. Chun, M. Ern, P. Preusse, Q. T. Trinh, S. D. Eckermann, and M. Riese, 2016: Comparison of simulated and observed convective gravity waves. *Journal of Geophysical Research-Atmospheres*, **121,** 13474-13492.
Kiladis, G. N., M. C. Wheeler, P. T. Haertel, K. H. Straub, and P. E. Roundy, 2009: Convectively coupled equatorial waves. *Reviews of Geophysics*, **47**.
Kooperman, G. J., M. S. Pritchard, M. A. Burt, M. D. Branson, and D. A. Randall, 2016: Robust effects of cloud superparameterization on simulated daily rainfall intensity statistics across multiple versions of the Community Earth System Model. *Journal of Advances in Modeling Earth Systems*, **8,** 140-165.
Kooperman, G. J., and Coauthors, 2018: Forest response to rising CO2 drives zonally asymmetric rainfall change over tropical land. *Nature Climate Change*, **8,** 434-+.
Koster, R. D., and Coauthors, 2004: Regions of Strong Coupling Between Soil Moisture and Precipitation. *Science*, **305,** 1138-1140.
Koster, R. D., and Coauthors, 2006a: GLACE: The Global Land-Atmosphere Coupling Experiment. Part I: Overview. *Journal of Hydrometeorology*, **7,** 590-610.
Koster, R. D., and Coauthors, 2006b: GLACE: The Global Land-Atmosphere Coupling Experiment. Part I: Overview. *J Hydrometeorol*, **7,** 590-610.
Langenbrunner, B., M. S. Pritchard, G. J. Kooperman, and J. T. Randerson, 2019: Why Does Amazon Precipitation Decrease When Tropical Forests Respond to Increasing CO2? *Earths Future*, **7,** 450-468.
Lawrence, D., and K. Vandecar, 2015: Effects of tropical deforestation on climate and agriculture. *Nature Climate Change*, **5,** 174-174.
Levine, N. M., and Coauthors, 2016a: Ecosystem heterogeneity determines the ecological resilience of the Amazon to climate change. *Proc Natl Acad Sci U S A*, **113,** 793-797.
Levine, P. A., J. T. Randerson, S. C. Swenson, and D. M. Lawrence, 2016b: Evaluating the strength of the land-atmosphere moisture feedback in Earth system models using satellite observations. *Hydrology and Earth System Sciences*, **20,** 4837-4856.
Levine, P. A., J. T. Randerson, Y. Chen, M. S. Pritchard, M. Xu, and F. M. Hoffman, 2019: Soil Moisture Variability Intensifies and Prolongs Eastern Amazon Temperature and Carbon Cycle Response to El Niño–Southern Oscillation. *Journal of Climate*, **32,** 1273-1292.
Li, L. H., and Coauthors, 2018: Evaluating Global Land Surface Models in CMIP5: Analysis of Ecosystem Water- and Light-Use Efficiencies and Rainfall Partitioning. *Journal of Climate*, **31,** 2995-3008.
Li, Y., B. Wang, D. Wang, J. Li, and L. Dong, 2014: An orthogonal terrain-following coordinate and its preliminary tests using 2-D idealized advection experiments. *Geoscientific Model Development*, **7,** 1767-1778.
Lin, S.-J., 2004: A "Vertically Lagrangian" Finite-Volume Dynamical Core for Global Models. *Monthly Weather Review*, **132,** 2293-2307.
Lintner, B. R., D. K. Adams, K. A. Schiro, A. M. Stansfield, A. A. A. Rocha, and J. D. Neelin, 2017: Relationships among climatological vertical moisture structure, column water vapor, and precipitation over the central Amazon in observations and CMIP5 models. *Geophys. Res. Lett.*, **44,** 1981-1989.
Lock, S. J., H. W. Bitzer, A. Coals, A. Gadian, and S. Mobbs, 2012: Demonstration of a Cut-Cell Representation of 3D Orography for Studies of Atmospheric Flows over Very Steep Hills. *Monthly Weather Review*, **140,** 411-424.
Lorenz, R., E. B. Jaeger, and S. I. Seneviratne, 2010: Persistence of heat waves and its link to soil moisture memory. *Geophysical Research Letters*, **37,** L09703-L09703.
Lorenz, R., and Coauthors, 2016: Influence of land-atmosphere feedbacks on temperature and precipitation extremes in the GLACE-CMIP5 ensemble. *Journal of Geophysical Research-Atmospheres*, **121,** 607-623.
Machado, L. A. T., and Coauthors, 2018: Overview: Precipitation characteristics and sensitivities to environmental conditions during GoAmazon2014/5 and ACRIDICON-CHUVA. *Atmospheric Chemistry and Physics*, **18,** 6461-6482.

Malhi, Y., J. T. Roberts, R. A. Betts, T. J. Killeen, W. Li, and C. A. Nobre, 2008: Climate change, deforestation, and the fate of the Amazon. *Science*, **319,** 169-172.
Malhi, Y., and Coauthors, 2009: Exploring the likelihood and mechanism of a climate-change-induced dieback of the Amazon rainforest. *Proc Natl Acad Sci U S A*, **106,** 20610-20615.
Maloney, E. D., and C. D. Zhang, 2016: Dr. Yanai's Contributions to the Discovery and Science of the MJO. *Meteor Mon*, **56,** 4.1-4.18.
Mapes, B. E., T. T. Warner, M. Xu, and A. J. Negri, 2003: Diurnal patterns of rainfall in northwestern South America. Part I: Observations and context. *Monthly Weather Review*, **131,** 799-812.
Marti, O., and Coauthors, 2010: Key features of the IPSL ocean atmosphere model and its sensitivity to atmospheric resolution. *Climate Dynamics*, **34,** 1-26.
Martin, G. M., M. A. Ringer, V. D. Pope, A. Jones, C. Dearden, and T. J. Hinton, 2006: The Physical Properties of the Atmosphere in the New Hadley Centre Global Environmental Model (HadGEM1). Part I: Model Description and Global Climatology. *Journal of Climate*, **19,** 1274-1301.
Martin, S. T., and Coauthors, 2016: Introduction: Observations and Modeling of the Green Ocean Amazon (GoAmazon2014/5). *Atmospheric Chemistry and Physics*, **16,** 4785-4797.
McDermid, S. S., C. Montes, B. I. Cook, M. J. Puma, N. Y. Kiang, and I. Aleinov, 2019: The Sensitivity of Land-Atmosphere Coupling to Modern Agriculture in the Northern Midlatitudes. *Journal of Climate*, **32,** 465-484.
Medvigy, D., R. L. Walko, M. J. Otte, and R. Avissar, 2013: Simulated Changes in Northwest US Climate in Response to Amazon Deforestation. *Journal of Climate*, **26,** 9115-9136.
Mehran, A., A. AghaKouchak, and T. J. Phillips, 2014: Evaluation of CMIP5 continental precipitation simulations relative to satellite- based gauge- adjusted observations. *Journal of Geophysical Research-Atmospheres*, **119,** 1695-1707.
Mei, R., and G. Wang, 2012: Summer Land-Atmosphere Coupling Strength in the United States: Comparison among Observations, Reanalysis Data, and Numerical Models. *J Hydrometeorol*, **13,** 1010-1022.
Mizuta, R., and Coauthors, 2012: Climate Simulations Using MRI-AGCM3.2 with 20-km Grid. *Journal of the Meteorological Society of Japan. Ser. II*, **90A,** 233-258.
Mlawer, E. J., S. J. Taubman, P. D. Brown, M. J. Iacono, and S. A. Clough, 1997: Radiative transfer for inhomogeneous atmospheres: RRTM, a validated correlated-k model for the longwave. *Journal of Geophysical Research-Atmospheres*, **102,** 16663-16682.
Morrison, H., and A. Gettelman, 2008: A new two-moment bulk stratiform cloud microphysics scheme in the community atmosphere model, version 3 (CAM3). Part I: Description and numerical tests. *Journal of Climate*, **21,** 3642-3659.
Mueller, B., and S. I. Seneviratne, 2012: Hot days induced by precipitation deficits at the global scale. *Proceedings of the National Academy of Sciences of the United States of America*, **109,** 12398-12403.
——, 2014: Systematic land climate and evapotranspiration biases in CMIP5 simulations. *Geophys Res Lett*, **41,** 128-134.
Neukom, R., and Coauthors, 2015: Facing unprecedented drying of the Central Andes? Precipitation variability over the period AD 1000–2100. *Environmental Research Letters*, **10,** 084017.
Park, S., and C. S. Bretherton, 2009: The University of Washington Shallow Convection and Moist Turbulence Schemes and Their Impact on Climate Simulations with the Community Atmosphere Model. *Journal of Climate*, **22,** 3449-3469.
Park, S., C. S. Bretherton, and P. J. Rasch, 2014: Integrating Cloud Processes in the Community Atmosphere Model, Version 5. *Journal of Climate*, **27,** 6821-6856.
Pascale, S., L. M. V. Carvalho, D. K. Adams, C. L. Castro, and I. F. A. Cavalcanti, 2019: Current and Future Variations of the Monsoons of the Americas in a Warming Climate. *Curr Clim Change Rep*, **5,** 125-144.
Phillips, T. J., and S. A. Klein, 2014: Land-atmosphere coupling manifested in warm-season observations on the U.S. southern great plains. *Journal of Geophysical Research-Atmospheres*, **119,** 509-528.
Pritchard, M. S., and R. C. J. Somerville, 2009: Assessing the Diurnal Cycle of Precipitation in a Multi-Scale Climate Model. *Journal of Advances in Modeling Earth Systems*, **1,** 12-12.
Putman, W. M., and S.-J. Lin, 2007: Finite-volume transport on various cubed-sphere grids. *Journal of Computational Physics*, **227,** 55-78.
Qin, H. C., M. S. Pritchard, G. J. Kooperman, and H. Parishani, 2018: Global Effects of Superparameterization on Hydrothermal Land-Atmosphere Coupling on Multiple Timescales. *J. Adv. Model. Earth Syst.*, **10,** 530-549.
Raddatz, T. J., and Coauthors, 2007: Will the tropical land biosphere dominate the climate–carbon cycle feedback during the twenty-first century? *Climate Dynamics*, **29,** 565-574.

Randall, D., M. Khairoutdinov, A. Arakawa, and W. Grabowski, 2003: Breaking the cloud parameterization deadlock. *Bulletin of the American Meteorological Society*, **84,** 1547-1564.
Randall, D. A., 2013: Beyond deadlock. *Geophysical Research Letters*, **40,** 5970-5976.
Rasmussen, K. L., and R. A. Houze, 2016: Convective Initiation near the Andes in Subtropical South America. *Monthly Weather Review*, **144,** 2351-2374.
Raymond, D. J., and A. M. Blyth, 1986: A Stochastic Mixing Model for Nonprecipitating Cumulus Clouds. *J. Atmos. Sci.*, **43,** 2708-2718.
——, 1992: Extension of the Stochastic Mixing Model to Cumulonimbus Clouds. *J. Atmos. Sci.*, **49,** 1968-1983.
Raymond, D. J., S. L. Sessions, A. H. Sobel, and Z. Fuchs, 2009: The Mechanics of Gross Moist Stability. *Journal of Advances in Modeling Earth Systems*, **1,** n/a-n/a.
Richter, J. H., and P. J. Rasch, 2008: Effects of convective momentum transport on the atmospheric circulation in the community atmosphere model, version 3. *Journal of Climate*, **21,** 1487-1499.
Ringer, M. A., and Coauthors, 2006: The Physical Properties of the Atmosphere in the New Hadley Centre Global Environmental Model (HadGEM1). Part II: Aspects of Variability and Regional Climate. *Journal of Climate*, **19,** 1302-1326.
Risi, C., D. Noone, C. Frankenberg, and J. Worden, 2013: Role of continental recycling in intraseasonal variations of continental moisture as deduced from model simulations and water vapor isotopic measurements. *Water Resources Research*, **49,** 4136-4156.
Rotstayn, L. D., and Coauthors, 2010: Improved simulation of Australian climate and ENSO-related rainfall variability in a global climate model with an interactive aerosol treatment. *International Journal of Climatology*, **30,** 1067-1088.
Roundy, J. K., and E. F. Wood, 2015: The Attribution of Land-Atmosphere Interactions on the Seasonal Predictability of Drought. *JOURNAL OF HYDROMETEOROLOGY*, **16,** 793-810.
Sakaguchi, K., L. R. Leung, C. D. Burleyson, H. Xiao, and H. Wan, 2018: Role of Troposphere-Convection-Land Coupling in the Southwestern Amazon Precipitation Bias of the Community Earth System Model Version 1 (CESM1). *Journal of Geophysical Research-Atmospheres*, **123,** 8374-8399.
Santanello, J. A., C. D. Peters-Lidard, S. V. Kumar, C. Alonge, and W.-K. Tao, 2009a: A Modeling and Observational Framework for Diagnosing Local Land–Atmosphere Coupling on Diurnal Time Scales. *J Hydrometeorol*, **10,** 577-599.
Santanello, J. A., C. D. Peters-Lidard, S. V. Kumar, C. Alonge, and W. K. Tao, 2009b: A Modeling and Observational Framework for Diagnosing Local Land-Atmosphere Coupling on Diurnal Time Scales. *Journal of Hydrometeorology*, **10,** 577-599.
Santanello Jr, J. A., C. D. Peters-Lidard, and S. V. Kumar, 2011: Diagnosing the Sensitivity of Local Land-Atmosphere Coupling via the Soil Moisture-Boundary Layer Interaction. *J Hydrometeorol*, **12,** 766-786.
Santanello Jr, J. A., C. D. Peters-Lidard, A. Kennedy, and S. V. Kumar, 2013: Diagnosing the Nature of Land-Atmosphere Coupling: A Case Study of Dry/Wet Extremes in the US Southern Great Plains. *J Hydrometeorol*, **14,** 3-24.
Sasaki, W., R. Onishi, H. Fuchigami, K. Goto, S. Nishikawa, Y. Ishikawa, and K. Takahashi, 2016: MJO simulation in a cloud-system-resolving global ocean-atmosphere coupled model. *Geophysical Research Letters*, **43,** 9352-9360.
Satoh, M., B. Stevens, F. Judt, M. Khairoutdinov, S.-J. Lin, W. M. Putman, and P. Düben, 2019: Global Cloud-Resolving Models. *Curr Clim Change Rep*, **5,** 172-184.
Schiro, K. A., F. Ahmed, S. E. Giangrande, and J. D. Neelin, 2018: GoAmazon2014/5 campaign points to deep-inflow approach to deep convection across scales. *Proc Natl Acad Sci U S A*, **115,** 4577-4582.
Schlemmer, L., C. Hohenegger, J. Schmidli, and C. Schar, 2012: Diurnal equilibrium convection and land surface-atmosphere interactions in an idealized cloud-resolving model. *Quarterly Journal of the Royal Meteorological Society*, **138,** 1526-1539.
Schwingshackl, C., M. Hirschi, and S. I. Seneviratne, 2018: A theoretical approach to assess soil moisture-climate coupling across CMIP5 and GLACE-CMIP5 experiments. *Earth Syst Dynam*, **9,** 1217-1234.
Scoccimarro, E., and Coauthors, 2011: Effects of Tropical Cyclones on Ocean Heat Transport in a High-Resolution Coupled General Circulation Model. *Journal of Climate*, **24,** 4368-4384.
Seager, R., and N. Henderson, 2013: Diagnostic Computation of Moisture Budgets in the ERA-Interim Reanalysis with Reference to Analysis of CMIP-Archived Atmospheric Model Data. *Journal of Climate*, **26,** 7876-7901.
Seiler, C., R. W. A. Hutjes, and P. Kabat, 2013: Likely Ranges of Climate Change in Bolivia. *Journal of Applied Meteorology and Climatology*, **52,** 1303-1317.
Seneviratne, S. I., D. Luthi, M. Litschi, and C. Schar, 2006: Land-atmosphere coupling and climate change in Europe. *Nature*, **443,** 205-209.

Seneviratne, S. I., and Coauthors, 2010a: Investigating soil moisture-climate interactions in a changing climate: A review. *Earth-Sci Rev*, **99,** 125-161.
Seneviratne, S. I., and Coauthors, 2010b: Investigating soil moisture–climate interactions in a changing climate: A review. *Earth-Science Reviews*, **99,** 125-161.
Seneviratne, S. I., and Coauthors, 2013: Impact of soil moisture-climate feedbacks on CMIP5 projections: First results from the GLACE-CMIP5 experiment. *Geophysical Research Letters*, **40,** 5212-5217.
Seo, E., and Coauthors, 2019: Impact of soil moisture initialization on boreal summer subseasonal forecasts: mid-latitude surface air temperature and heat wave events. *Climate Dynamics*, **52,** 1695-1709.
Shaw, J., and H. Weller, 2016: Comparison of Terrain-Following and Cut-Cell Grids Using a Nonhydrostatic Model. *Monthly Weather Review*, **144,** 2085-2099.
Snyder, P. K., 2010: The Influence of Tropical Deforestation on the Northern Hemisphere Climate by Atmospheric Teleconnections. *Earth Interactions*, **14**.
Stevens, B., and Coauthors, 2019: DYAMOND: the DYnamics of the Atmospheric general circulation Modeled On Non-hydrostatic Domains. *Progress in Earth and Planetary Science*, **6,** 61.
Sun, J., and M. S. Pritchard, 2016: Effects of explicit convection on global land-atmosphere coupling in the superparameterized CAM. *J. Adv. Model. Earth Syst.*, **8,** 1248-1269.
Sun, X., and A. P. Barros, 2015a: Impact of Amazonian evapotranspiration on moisture transport and convection along the eastern flanks of the tropical Andes. *Quarterly Journal of the Royal Meteorological Society*, **141,** 3325-3343.
Sun, X. M., and A. P. Barros, 2015b: Isolating the Role of Surface Evapotranspiration on Moist Convection along the Eastern Flanks of the Tropical Andes Using a Quasi-Idealized Approach. *J. Atmos. Sci.*, **72,** 243-261.
Taylor, C. M., R. A. de Jeu, F. Guichard, P. P. Harris, and W. A. Dorigo, 2012a: Afternoon rain more likely over drier soils. *Nature*, **489,** 423-426.
Taylor, C. M., A. Gounou, F. Guichard, P. P. Harris, R. J. Ellis, F. Couvreux, and M. De Kauwe, 2011: Frequency of Sahelian storm initiation enhanced over mesoscale soil-moisture patterns. *Nature Geoscience*, **4,** 430-433.
Taylor, K. E., R. J. Stouffer, and G. A. Meehl, 2012b: An Overview of Cmip5 and the Experiment Design. *Bulletin of the American Meteorological Society*, **93,** 485-498.
Tian, B. J., E. J. Fetzer, B. H. Kahn, J. Teixeira, E. Manning, and T. Hearty, 2013: Evaluating CMIP5 models using AIRS tropospheric air temperature and specific humidity climatology. *Journal of Geophysical Research-Atmospheres*, **118,** 114-134.
Urrutia, R., and M. Vuille, 2009: Climate change projections for the tropical Andes using a regional climate model: Temperature and precipitation simulations for the end of the 21st century. *Journal of Geophysical Research: Atmospheres*, **114**.
Veiga, J. A. P., V. B. Rao, and S. H. Franchito, 2005: Heat and moisture budgets of the Walker circulation and associated rainfall anomalies during El Nino events. *International Journal of Climatology*, **25,** 193-213.
Vizy, E. K., and K. H. Cook, 2007: Relationship between Amazon and high Andes rainfall. *Journal of Geophysical Research-Atmospheres*, **112**.
Voldoire, A., and Coauthors, 2013: The CNRM-CM5.1 global climate model: description and basic evaluation. *Climate Dynamics*, **40,** 2091-2121.
Volodin, E. M., N. A. Dianskii, and A. V. Gusev, 2010: Simulating present-day climate with the INMCM4.0 coupled model of the atmospheric and oceanic general circulations. *Izvestiya, Atmospheric and Oceanic Physics*, **46,** 414-431.
von Salzen, K., and Coauthors, 2013: The Canadian Fourth Generation Atmospheric Global Climate Model (CanAM4). Part I: Representation of Physical Processes. *Atmosphere-Ocean*, **51,** 104-125.
Wang, D., S. E. Giangrande, M. J. Bartholomew, J. Hardin, Z. Feng, R. Thalman, and L. A. T. Machado, 2018: The Green Ocean: precipitation insights from the GoAmazon2014/5 experiment. *Atmospheric Chemistry and Physics*, **18,** 9121-9145.
Watanabe, M., and Coauthors, 2010: Improved Climate Simulation by MIROC5: Mean States, Variability, and Climate Sensitivity. *Journal of Climate*, **23,** 6312-6335.
Watanabe, S., and Coauthors, 2011: MIROC-ESM 2010: model description and basic results of CMIP5-20c3m experiments. *Geosci. Model Dev.*, **4,** 845-872.
Wei, J., and P. A. Dirmeyer, 2010: Toward understanding the large-scale land-atmosphere coupling in the models: Roles of different processes. *Geophys. Res. Lett.*, **37**.
Wei, J., P. A. Dirmeyer, and Z. Guo, 2010: How Much Do Different Land Models Matter for Climate Simulation? Part II: A Decomposed View of the Land–Atmosphere Coupling Strength. *Journal of Climate*, **23,** 3135-3145.

Werth, D., and R. Avissar, 2002: The local and global effects of Amazon deforestation. *Journal of Geophysical Research-Atmospheres*, **107**.
White, C. J., and Coauthors, 2017: Potential applications of subseasonal-to-seasonal (S2S) predictions. *Meteorological Applications*, **24,** 315-325.
Wilks, D. S., 2016: "THE STIPPLING SHOWS STATISTICALLY SIGNIFICANT GRID POINTS" How Research Results are Routinely Overstated and Overinterpreted, and What to Do about It. *Bulletin of the American Meteorological Society*, **97,** 2263-+.
Williams, I. N., 2019: Evaluating Soil Moisture Feedback on Convective Triggering: Roles of Convective and Land-Model Parameterizations. *Journal of Geophysical Research-Atmospheres*, **124,** 317-332.
Wright, J. S., and Coauthors, 2017: Rainforest-initiated wet season onset over the southern Amazon. *Proc Natl Acad Sci U S A*, **114,** 8481-8486.
Wu, L. Y., and J. Y. Zhang, 2013: Role of land-atmosphere coupling in summer droughts and floods over eastern China for the 1998 and 1999 cases. *Chinese Science Bulletin*, **58,** 3978-3985.
Xavier, A. C., C. W. King, and B. R. Scanlon, 2016: Daily gridded meteorological variables in Brazil (1980-2013). *International Journal of Climatology*, **36,** 2644-2659.
Yang, Q., L. R. Leung, S. A. Rauscher, T. D. Ringler, and M. A. Taylor, 2014: Atmospheric Moisture Budget and Spatial Resolution Dependence of Precipitation Extremes in Aquaplanet Simulations. *Journal of Climate*, **27,** 3565-3581.
Yin, L., R. Fu, E. Shevliakova, and R. E. Dickinson, 2012: How well can CMIP5 simulate precipitation and its controlling processes over tropical South America? *Climate Dynamics*, **41,** 3127-3143.
Yu, R. C., J. Li, Y. Zhang, and H. M. Chen, 2015: Improvement of rainfall simulation on the steep edge of the Tibetan Plateau by using a finite-difference transport scheme in CAM5. *Climate Dynamics*, **45,** 2937-2948.
Yukimoto, S., and Coauthors, 2012: A New Global Climate Model of the Meteorological Research Institute: MRI-CGCM3 —Model Description and Basic Performance&mdash. *Journal of the Meteorological Society of Japan. Ser. II*, **90A,** 23-64.
Zaitchik, B. F., J. A. Santanello, S. V. Kumar, and C. D. Peters-Lidard, 2013: Representation of Soil Moisture Feedbacks during Drought in NASA Unified WRF (NU-WRF). *Journal of Hydrometeorology*, **14,** 360-367.
Zhang, G. J., and N. A. Mcfarlane, 1995: Sensitivity of Climate Simulations to the Parameterization of Cumulus Convection in the Canadian Climate Center General-Circulation Model. *Atmosphere-Ocean*, **33,** 407-446.
Zhang, K., and Coauthors, 2017: Influence of Superparameterization and a Higher-Order Turbulence Closure on Rainfall Bias Over Amazonia in Community Atmosphere Model Version 5. *Journal of Geophysical Research: Atmospheres*, **122,** 9879-9902.
Zhao, M., I. M. Held, S.-J. Lin, and G. A. Vecchi, 2009: Simulations of Global Hurricane Climatology, Interannual Variability, and Response to Global Warming Using a 50-km Resolution GCM. *Journal of Climate*, **22,** 6653-6678.
Zhou, S., and Coauthors, 2019: Land-atmosphere feedbacks exacerbate concurrent soil drought and atmospheric aridity. *Proceedings of the National Academy of Sciences of the United States of America*, **116,** 18848-18853.
Zou, X., Y. Y. Li, J. X. Li, and B. Wang, 2016: Advection errors in an orthogonal terrain-following coordinate: idealized 2-D experiments using steep terrains. *Atmospheric Science Letters*, **17,** 243-250.

A. Supplement to Chapter 2

Figure A1 illustrates the soil moisture trajectories in ENS(W) and ENS(S) at one location. Soil liquid water (h2osoi_liq, kg/m2) was chosen to represent soil moisture.

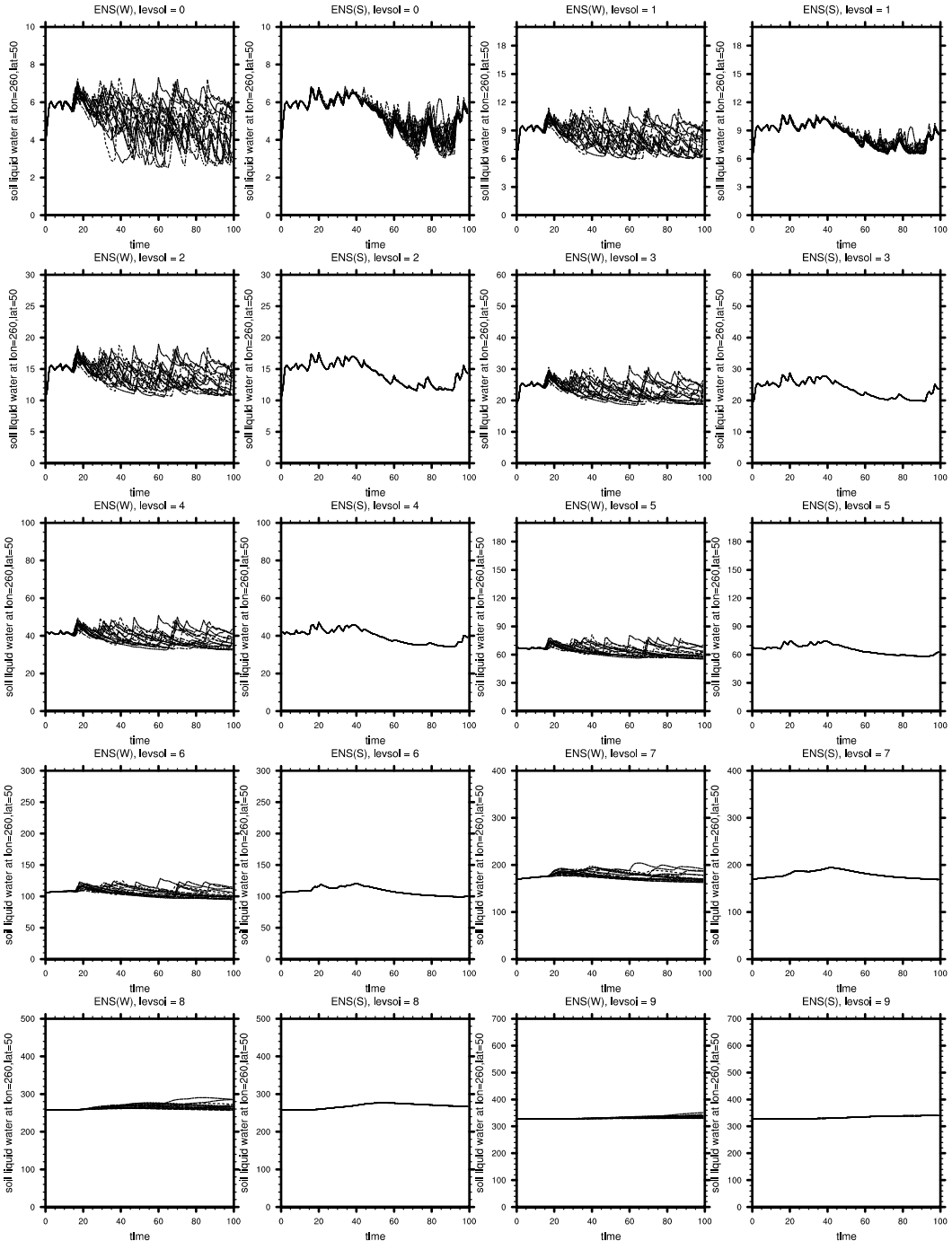

Figure A1. Using liquid water content time series from ensemble members at one grid point to illustrate the implementation of subsurface (deeper than 5cm) soil moisture prescription. Level 0 and level 1 are above 5cm in depth, level 2-9 deeper than 5cm. Soil liquid water time series spread among ensemble members in the writing ensemble (ENS(W)) at all levels and in the subsurface reading ensemble (ENS(S)) at level 0 and level 1. Ensemble spread is absent as a result of soil liquid water prescription among ensemble members in ENS(S) for level 2-9.

In order to add soil moisture writing and reading capabilities to the default land model, modifications were made in the following two files:

1. models/lnd/clm2/src/main/driver.F90

2. models/lnd/clm2/src/biogeophys/BalanceCheckMod.F90

B. Supplement to Chapter 3

Figure B1 presents how both CAM3.5 and SPCAM3.5 perform against GPCP datasets in terms of the mean and standard deviation of boreal summer (JJA) rainfall in 1996-2015 AMIP simulations. This analysis also supports the argument that SPCAM3.5 better represents rainfall over Arabian Peninsula on two basic statistics.

Figure B2 examines soil moisture at multiple depths over Arabia in ENS(W) in CAM3.5 and SPCAM3.5. It suggests that SPCAM has dryer soil moisture at both near-surface and deeper levels.

Figure B3 presents summer mean precipitation in ENS(W) over SW US in CAM3.5 and SPCAM3.5. Figure B4 is similar to Figure B2 but applied to SW US. Figure B3 and Figure B4 together implies that "there must be another factor independent of mean precipitation or its associated soil moisture abundance that can produce enhanced thermal coupling under SP."

Figure B5 supplements Figure 3.8 in the main article. It exhibits the terrestrial coupling index [Dirmeyer, 2011] based on the AMIP simulation, but with removal of drizzle mode with multiple

thresholds to determine drizzling. Regional enhancement of coupling over SW US in SPCAM3.5 is insensitive to the threshold. This further illustrates that the drizzling removal of SP is unlikely to explain the enhancement of thermal coupling over SW US.

Table B1 supplements Figure 3.6 in the main text. It supports the idea that soil moisture variability in the very dry decile bins is very small in both CAM and SPCAM. Such little variability in soil moisture is most likely unable to support a strong coupling between soil moisture within these bins and near-surface temperature [Dirmeyer, 2011; Seneviratne et al., 2010].

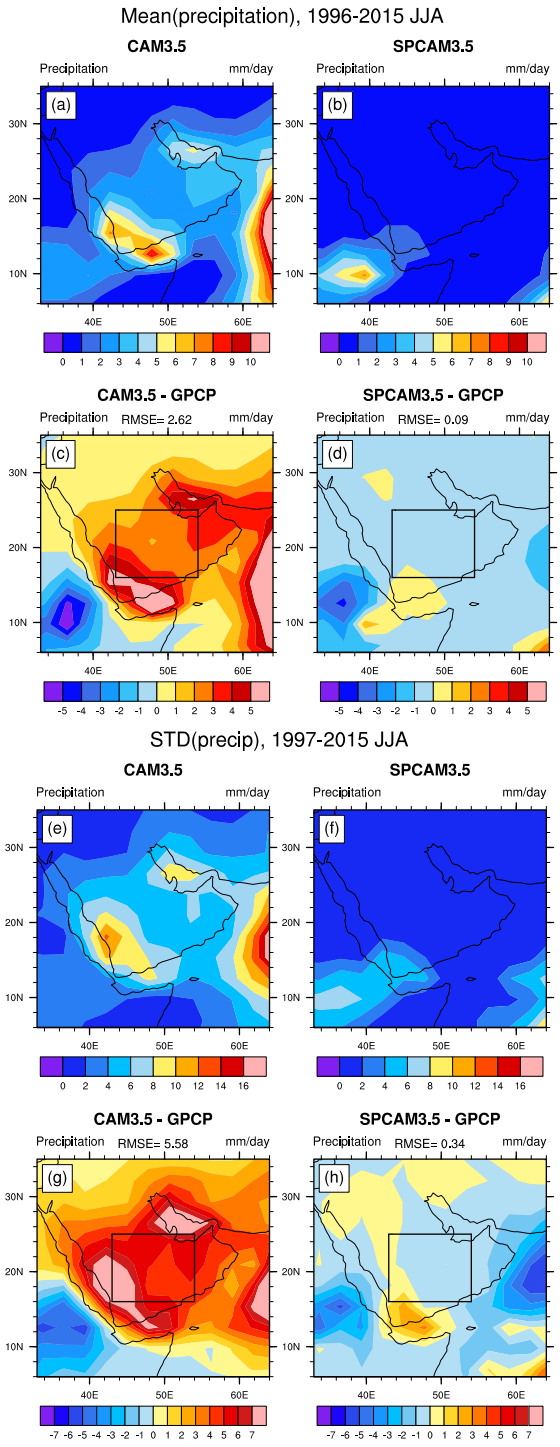

Figure B1. AMIP 1996-2015 JJA mean precipitation over Arabia from (a) CAM3.5 and (b) SPCAM3.5; anomalies relative to GPCP in (c) CAM3.5 and (d) SPCAM3.5; (e-h) Same as (a-d), but for standard deviation of precipitation. Root-mean-square errors are calculated within the black box and are shown on top of (c-d), (g-h). Calculation of mean uses monthly precipitation data from GPCP v2.3 as in the main article. Calculations of standard deviation uses GPCP 1-Degree Daily Combination v1.2.

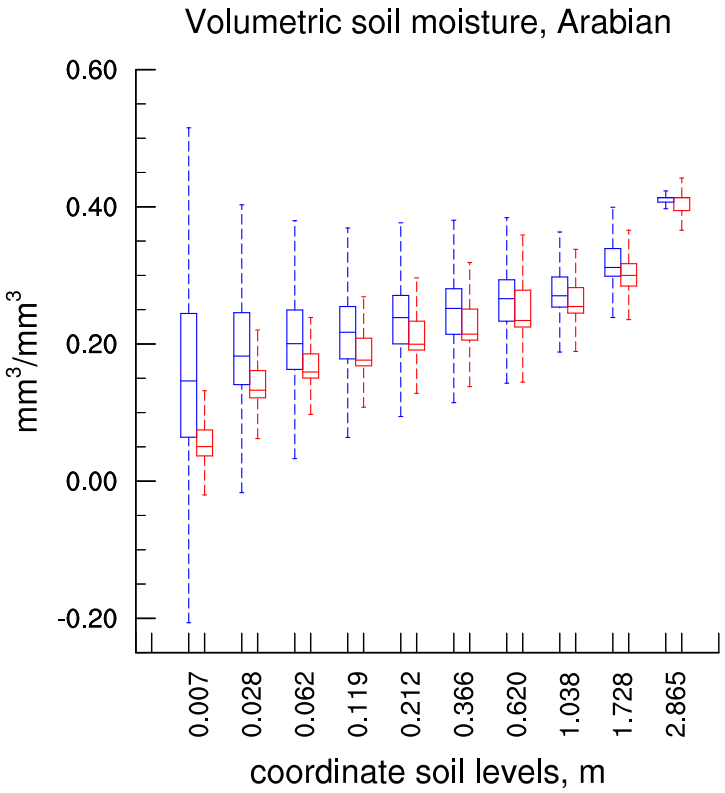

Figure B2. Based on ENS(W), box-and-whisker plot of volumetric soil moisture within the Arabian box (as outlined in black in Figure 3) at different soil levels in CAM3.5 (blue color) and SPCAM3.5 (red color). The lower (upper) end of the whisker is determined by 1.5 interquartile range from lower (upper) quartile.

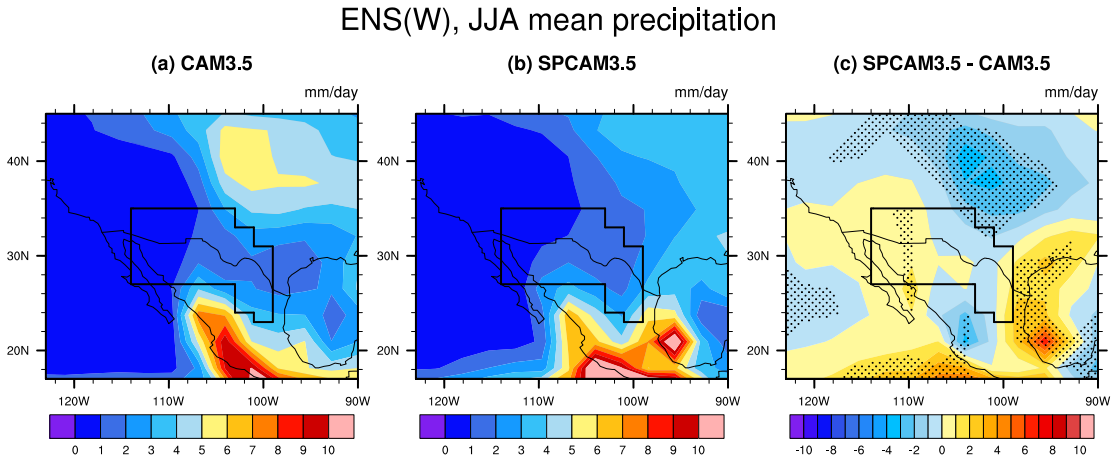

Figure B3. Same as Figure 3.3, but over the Southwestern US and Northern Mexico and here $\alpha_{FDR} = 0.15$.

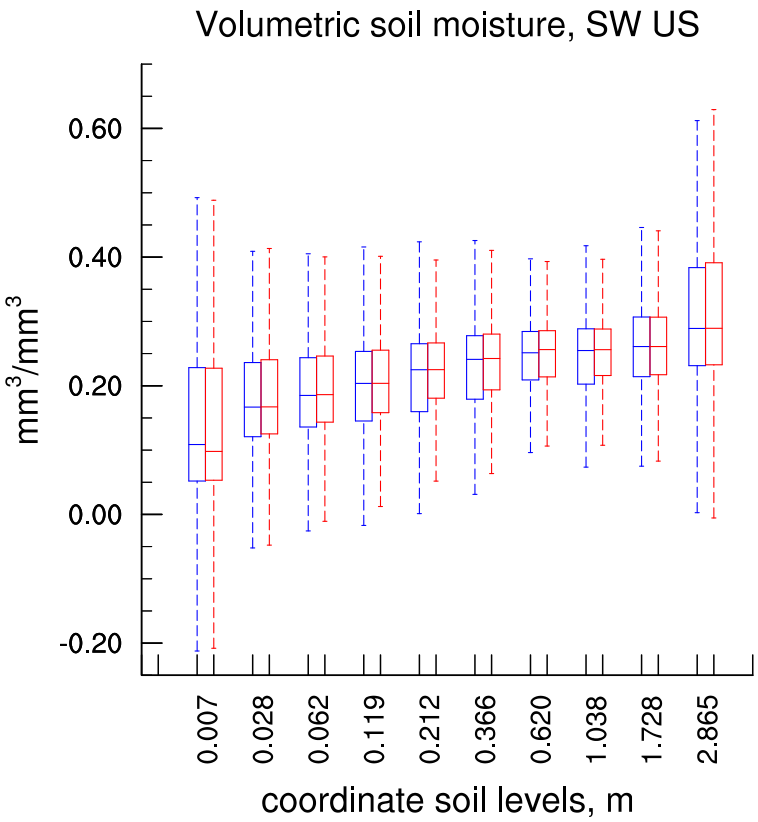

Figure B4. Same as Figure B2, but over the Southwestern US and Northern Mexico.

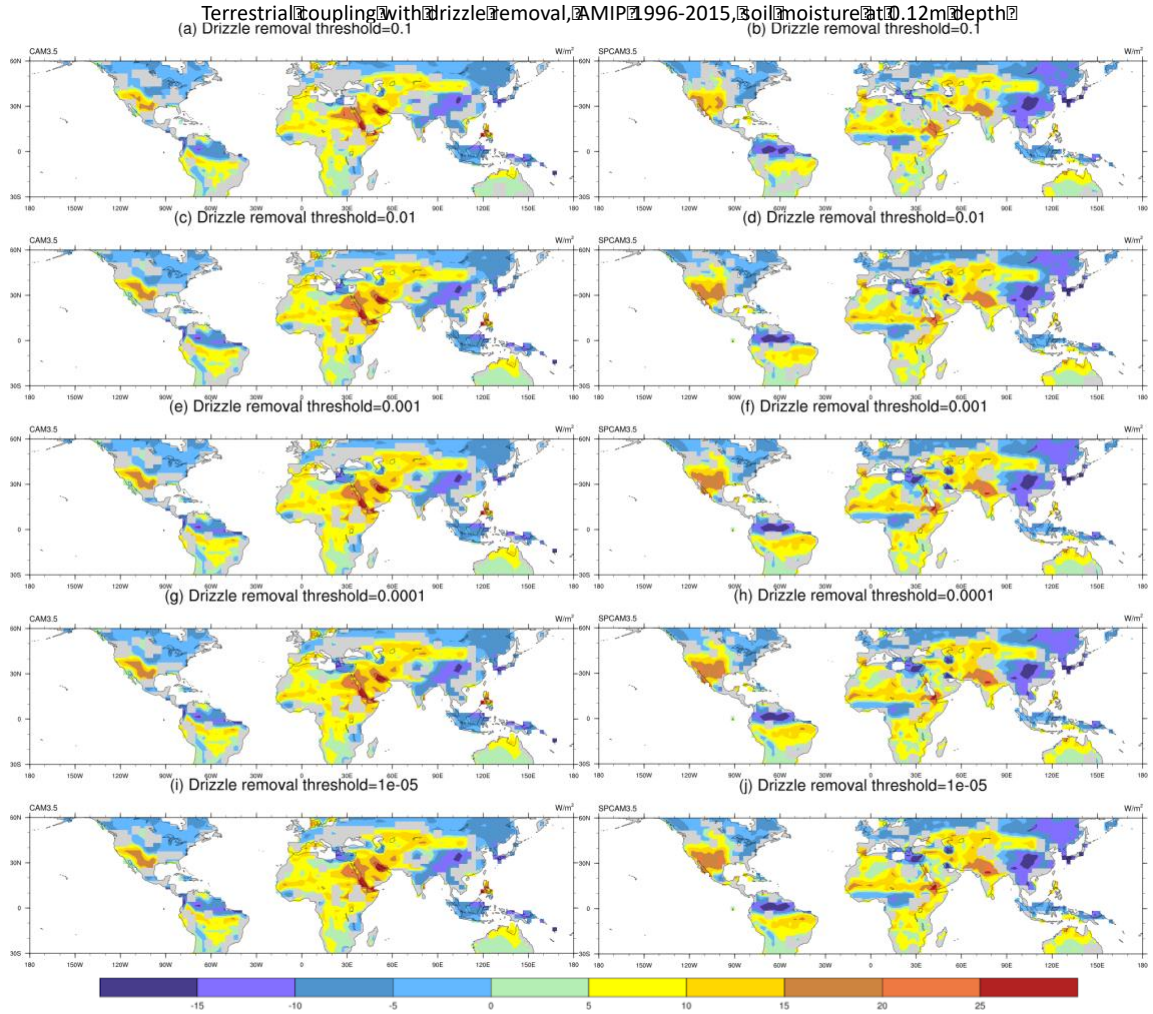

Figure B5. Based on 1996-2015 AMIP simulation, boreal summer, terrestrial coupling index in CAM3.5 (left column) and SPCAM3.5 (right column). Days in which total precipitaion is less than (a,b) 0.1, (c,d) 0.01, (e,f) 0.001, (g,h) 0.0001, (i,j) 1.0×10^{-5} mm/day are removed in both models. Consistent with Figure 4, soil moisture chosen to be soil liquid water in kg/m^2, at 0.12m depth.

Table B1. Based on daily samples in ENS(W), over Southwestern US and Northern Mexico during boreal summer, standard deviation of volumetric soil moisture (0.007m) within each decile bin. Units: mm_3/mm_3

Soil moisture	[0.025, 0.033)	[0.033, 0.046)	[0.046, 0.063)	[0.063, 0.075)	[0.075, 0.098)	[0.098, 0.151)	[0.151, 0.201)	[0.201, 0.253)	[0.253, 0.307)	[0.307, 1.031)
CAM	3.949 E-06	1.780 E-05	3.178 E-05	7.408 E-06	8.543 E-05	2.692 E-04	1.577 E-04	1.483 E-04	2.230 E-04	1.185 E-03
SPCAM	3.404 E-06	1.522 E-05	3.378 E-05	9.822 E-06	8.396 E-05	2.567 E-04	1.545 E-04	1.494 E-04	2.254 E-04	5.388 E-03

C. Supplement to Chapter 4

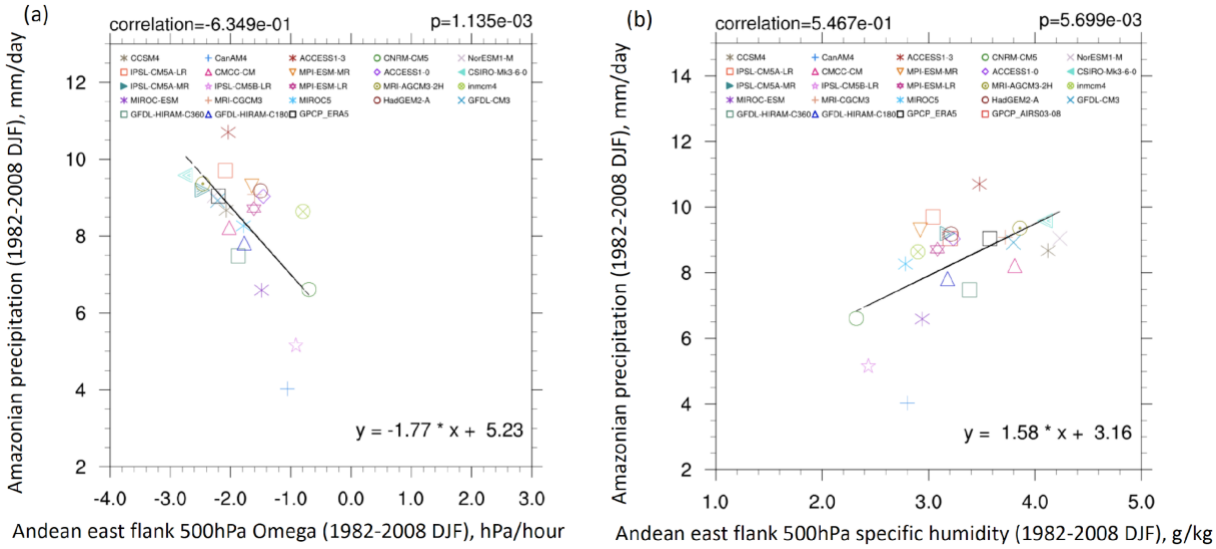

Figure C1. (a) X-axis: 500hPa vertical velocity (averaged over 1982-2008 Dec-Jan-Feb) on the east flank of the Andes (see Fig 4.7 red box 2). Y-axis: precipitation averaged over the Amazon (see Fig 4.7 red box 1). Units: vertical velocity in hPa/hour, precipitation in mm/day. Different symbols represent different CMIP5 models (see Table 4.1). In particular, the black square represents observational constraints where precipitation comes from GPCP v2.3, and 500 Omega comes from ERA5 reanalysis. Based on these 23 members, Pearson's r = -0.6349, p-value=0.001135. A linear regression obtained is y = -1.77x+5.23 (b) X-axis: 500hPa specific humidity (averaged over 1982-2008 Dec-Jan-Feb) on the east flank of the Andes (see Fig 4.7 red box 2). Y-axis: the same as in (a). Units: specific humidity in g/kg, precipitation in mm/day. The black square represents observational constrains where precipitation comes from GPCP v2.3, and 500hPa specific humidity comes from ERA5 reanalysis. For the pink square, 500hPa specific humidity comes from the satellite-derived AIRS dataset. Based on these 24 members, Pearson's R = -0.5467, p-value = 0.005699. A linear regression obtained is y = 0.58x + 3.16. Note that the AIRS dataset is only available after 2002 Sep, and here specific humidity from AIRS is the 2003-2008 Dec-Jan-Feb average (rather than 1982-2008 DJF). For AIRS datasets, the number of retrievals is low in cloudy regions (such as ITCZ), which reduces confidence.

Here we show that the vertical velocity and moisture fields in the middle troposphere on the Andean east flank have a significant correlation with Amazonian rainfall among CMIP5 AMIP simulations, satellite observations, and reanalysis datasets. Admittedly, part of the relationship between the Andean east flank 500hPa field and Amazonian rainfall is due to the covariance in adjacent boxes. That is, stronger ascending motion over the Amazon likely means stronger

upward motion on the Andean east flank, and stronger ascending generally correlates with more precipitation. Similar arguments can be made on wetter humidity. Nonetheless, based on our sensitivity experiments, the Andean east flank region is where we know that the dynamical responses of Andean convective forcing are strong. Therefore, we think the linear relationship obtained in Fig C1 may provide a partial diagnostic proxy for the Andean forced component of the WADA bias signal. Assuming it is not a coincidence the significant correlation may already suggest that realistic representations of the Andean east flank midlevel vertical velocity and humidity fields are associated with a model's skill in simulating Amazonian rainfall.

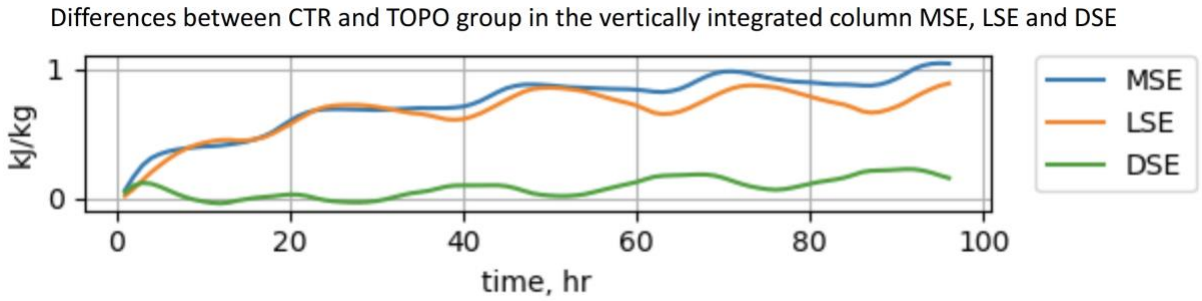

Figure C2. Differences between CTR and TOPO group in the vertically integrated column MSE, LSE, and DSE. This is evidence that the impacts of energy leakage in the experiment setup is minimal.